Search for Leptoquarks at HERA

Dissertation
zur Erlangung des Doktorgrades
des Department Physik
der Universität Hamburg

vorgelegt von
Antje Hüttmann
aus Hamburg

Hamburg 2009

Gutachter der Dissertation:	Prof. Dr. Peter Schleper JProf. Dr. Johannes Haller
Gutachter der Disputation:	Prof. Dr. Robert Klanner Prof. Dr. Dieter Horns
Datum der Disputation:	30.09.2009
Vorsitzender des Prüfungsausschusses:	Dr. Georg Steinbrück
Vorsitzender des Promotionsausschusses:	Prof. Dr. Robert Klanner
Dekan der MIN Fakultät:	Prof. Dr. Heinrich Graener

Abstract

A search for first generation leptoquarks was performed in polarized electron-proton collider data recorded with the ZEUS detector at HERA in the years 2003–2007. They were analyzed for final states with an electron and jets or with missing transverse momentum and jets and a search for resonance structures or other deviations from the Standard Model predictions in the spectra of the invariant mass of lepton and jets was performed. No evidence for leptoquark signals was found. The data were combined with the previously taken data at HERA corresponding to an integrated luminosity of 488 pb^{-1} and limits were set on the Yukawa coupling λ as a function of the leptoquark mass for different leptoquark types within the Buchmüller-Rückl-Wyler model.

Kurzfassung

Es wurde in polarisierten Elektron-Proton-Collider-Daten, die in den Jahren 2003–2007 mit dem ZEUS-Detektor bei HERA aufgenommen wurden, nach Leptoquarks der ersten Generation gesucht. Die Daten wurden auf Endzustände mit einem Elektron und Jets oder mit fehlendem Transversalimpuls und Jets hin untersucht und es wurde nach Resonanzstrukturen oder anderen Abweichungen von den Vorhersagen des Standardmodells in den Spektren der invarianten Masse von Lepton und Jets gesucht. Es wurden keine Hinweise auf Leptoquark-Signale gefunden. Die Daten wurden mit den früheren HERA-Daten kombiniert, was einer Gesamtluminosität von 488 pb^{-1} entspricht, und Grenzen auf die Yukawa-Kopplung λ als Funktion der Leptoquark-Masse für verschiedene Leptoquark-Typen im Buchmüller-Rückl-Wyler-Modell wurden bestimmt.

Contents

Chapter 1

Introduction

The Standard Model of particle physics [1] is a theoretical framework describing the elementary particles and their interactions. Even though it is very successful in describing experimentally measured processes, there are many open questions and fundamental problems arising from both theory and experiment, as:

- *Unification of the fundamental forces:* gravity is not included in the SM, and the strength of the gravitational force is many orders of magnitude lower than the strength of the electroweak and the strong force. Furthermore it is unclear why the electromagnetic and the weak force are unified to the electroweak force, but the strong and the electroweak force are not unified.

- *Symmetry between lepton and quark sector:* the SM does not explain why leptons and quarks both have three generations and why the charge of the proton equals the charge of the positron. Furthermore, it gives no explanation for the conservation of lepton and baryon number.

- *Higgs boson:* in the SM, the Higgs boson is needed to explain the generation of particle masses, but it has not been observed so far.

- *Neutrino mass:* in the Standard model neutrinos were originally assumed to be massless, but experimental evidence from neutrino oscillation experiments shows that they have a mass [2].

- *Composition of the universe:* it is unknown why our world is built almost solely from matter rather than antimatter. Furthermore, the origin of the so-called dark matter in the universe is unknown.

This gives reason to believe that physics beyond the Standard Model exists and that the Standard Model is only an effective low-energy approximation of a more fundamental theory. The symmetry between the lepton and the quark sector suggests a more fundamental relation between these sectors, as it is given by many extensions of the Standard Model. The most common approach is to introduce a higher symmetry embedding quarks and leptons in a single gauge group. In many of these models new bosons that can couple to a lepton and a quark exist, like for example leptoquarks. Leptoquarks are hypothetical scalar or vector bosons carrying both lepton and baryon number, as well as color charge and fractional electric charge.

The electron-proton collider HERA was particularly suited for searches of lepton-quark interactions not predicted by the SM. If new bosons such as leptoquarks coupling to leptons and quarks have masses of order M_Z, they could be observed as high-mass resonant states in ep scattering. New phenomena at mass scales in the TeV range, such as heavy leptoquarks exchange, could lead to measurable low energy effects and thus to deviations of the experimental measurements from the SM predictions.

In this thesis, a search for first generation leptoquarks with the ZEUS detector at HERA is presented. Deviations from the Standard Model in the invariant mass spectrum of lepton and jets were searched for in an analysis of polarized Neutral Current (NC) and Charged Current (CC) Deep Inelastic Scattering (DIS) at high momentum transfer Q^2. Since no evidence for any leptoquark signal was found, limits were derived on the Yukawa coupling λ as a function of the mass for different leptoquark states as described by the Buchmüller-Rückl-Wyler model [3].

This thesis is organized as follows. In Chapter 2, a theoretical overview of Deep Inelastic Scattering as well as an introduction to the Buchmüller-Rückl-Wyler model and the possibilities of observing leptoquarks at HERA and other colliders is given. In Chapter 3, the HERA accelerator and the ZEUS detector are briefly described, focusing on the components that are most relevant for this analysis. Chapter 4 describes the event reconstruction and the selection of NC and CC DIS events. The results of the leptoquark resonance search are presented in Chapter 5. Chapter 6 describes the leptoquark limit setting procedure and shows the limits set in the mass-coupling plane. In Chapter 7, the analysis is summarized and conclusions are drawn.

Chapter 2

Theory

2.1 Deep Inelastic Scattering (DIS)

In the Standard Model [1], high energy electron-proton collisions are described by the exchange of a virtual boson between the electron and the proton. If the momentum transfer is large enough and the interaction is highly inelastic, the electron collides directly with a single proton constituent (parton). The struck parton is knocked out of the proton and the proton is broken up [1]. Processes of Deep Inelastic Scattering (DIS) can be divided into two categories: Neutral Current (NC) processes with γ or Z^0 exchange and an electron in the final state, and Charged Current (CC) processes with $W^{\pm}$ exchange and a neutrino in the final state. In leading order, these processes are described by the Feynman graphs shown in figure 2.1. Besides the scattered electron (NC) or neutrino (CC), the final state consists of the struck quark and the proton remnant, which hadronize in the detector.

For the decription of DIS events, the following four-momenta are used:

- incoming proton: P
- incoming electron: k
- scattered electron: k'
- exchanged gauge boson: $q = k - k'$

From these four-momenta, four Lorentz invariants can be calculated:

[1] There are also so-called diffractive events in which the proton stays intact, but they are negligible in this analysis.

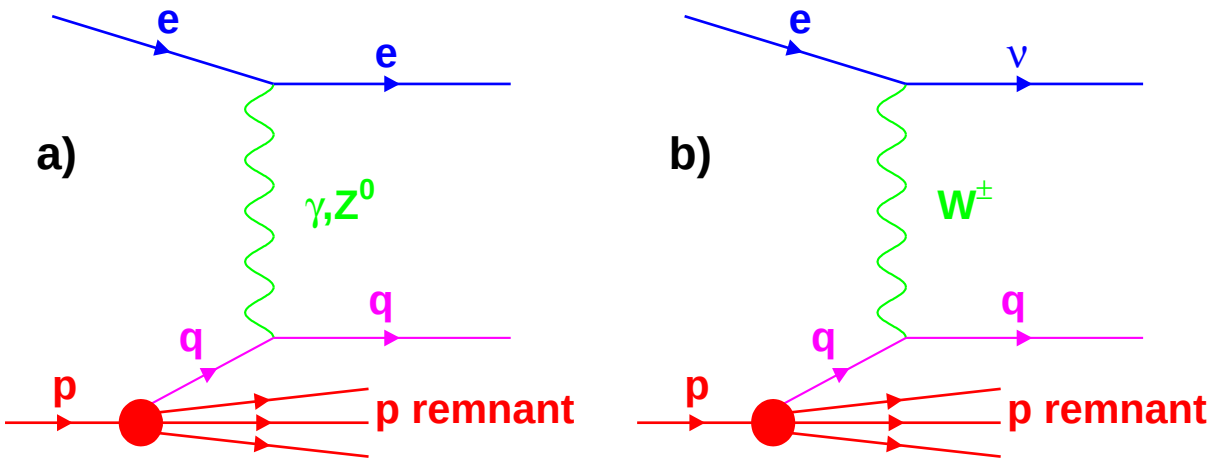

Figure 2.1: *Leading order Feynman graphs for deep inelastic ep scattering: (a) for NC and (b) for CC interactions.*

- The center of mass energy of the electron-proton-system:
  $s = (k + P)^2$
- The Bjorken scaling variable:
  $x = \frac{-q^2}{2q \cdot P}$
- The inelasticity (fractional energy loss of the electron in the rest frame of the proton):
  $y = \frac{q \cdot P}{k \cdot P}$
- The boson virtuality:
  $Q^2 = -q^2$

These variables are not independent, but are in leading order related by

$$Q^2 = xys, \tag{2.1}$$

where the electron and proton mass are neglected, as it is done in the quark parton model.

2.2 The Quark Parton Model

In the quark parton model (QPM) [4], the proton is moving with momentum approaching infinity along the z-direction, so that the transverse momentum of the proton and its

mass can be neglected. The proton is regarded as a collection of free, point-like partons each carrying a fraction of the proton momentum. The exchanged boson scatters elastically off a parton. The cross section for electron-proton scattering is obtained by folding the electron-parton cross section with the parton distribution function (PDF) and then summing over all active quark and antiquark flavors in the proton. The PDF gives the probability that a parton of a specific flavor carries a fraction of the hadron momentum.

In the QPM, the momentum fraction of the struck parton equals the Bjorken scaling variable x. The inelasticity y is related to the lepton scattering angle $\theta^\star$ in the lepton-quark center-of-mass system by

$$y = \frac{1}{2}(1 - \cos\theta^\star) \tag{2.2}$$

($\theta^\star = 0$ corresponding to no deflection).

The naive QPM cannot take into account for the presence of gluons. In the QCD improved QPM, gluon radiation and the splitting of gluons into $q\bar{q}$-pairs are included.

2.3 The DIS Cross Section

In this section, the NC and CC DIS cross sections at high Q^2 in the leading-order QCD improved QPM are presented [5]. The (longitudinal) polarization of the lepton beam is taken into account, whereas the nucleon is considered as unpolarized. The polarization of the lepton beam is defined as:

$$P = \frac{N_R - N_L}{N_R + N_L}, \tag{2.3}$$

where N_R and N_L are the number of right-handed and left-handed leptons in the beam, respectively.

Neutral Current

The NC differential cross section for the scattering of polarized electrons (polarization P) off unpolarized protons ($e^\pm p \to e^\pm X$) is given by:

$$\frac{d^2\sigma^\pm_{NC}}{dxdQ^2} = \frac{2\pi\alpha}{xQ^4}\left[H^\pm_0 + PH^\pm_P\right], \tag{2.4}$$

with

$$H^\pm_{0,P} = Y_+ F_2^{0,P} \mp Y_- x F_3^{0,P}, \tag{2.5}$$

where $Y_\pm = 1 \pm (1-y)^2$ and α is the electromagnetic coupling constant. The term $H_0^\pm$ is polarization-independent. F_2 and xF_3 are the structure functions describing the structure of the proton. They are given by:

$$F_2^{0,P} = \sum_i x\left(q_i(x,Q^2) + \bar{q}_i(x,Q^2)\right) A_i^{0,P}, \tag{2.6}$$

$$xF_3^{0,P} = \sum_i x\left(q_i(x,Q^2) - \bar{q}_i(x,Q^2)\right) B_i^{0,P}. \tag{2.7}$$

The sum runs over all quark flavors present in the proton, and $q_i(x,Q^2)$ and $\bar{q}_i(x,Q^2)$ are the PDFs. The function xF_3 provides direct information on the valence quark densities (assuming $q_{sea} = \bar{q}_{sea}$), and the function F_2 provides information on the valence and sea quark densities and indirectly on the gluon density. The coefficients A_i^0 and B_i^0 for the polarization-independent terms, and A_i^P and B_i^P for the polarization-dependent terms, are given by:

$$\begin{aligned} A_i^0 &= e_i^2 - 2e_i v_i v_e P_Z + (v_e^2 + a_e^2)(v_i^2 + a_i^2) P_Z^2 \\ B_i^0 &= -2e_i a_i a_e P_Z + 4 a_i v_i v_e a_e P_Z^2 \\ A_i^P &= 2e_i a_e v_i P_Z - 2a_e v_e (v_i^2 + a_i^2) P_Z^2 \\ B_i^P &= 2e_i a_i v_e P_Z - 2a_i v_i (v_e^2 + a_e^2) P_Z^2 \end{aligned} \tag{2.8}$$

Here, e_i is the quark charge (in units of the proton charge), and v_i and a_i are its NC vector and axial vector couplings. By convention, v_e and a_e are the vector and axial vector couplings of negatively charged electrons. P_Z describes the effect of the Z^0 propagator relative to that of the virtual photon and is given by:

$$P_Z = \frac{Q^2}{(Q^2 + M_Z^2)\sin^2 2\theta_W}, \tag{2.9}$$

where θ_W is the electroweak mixing angle, and M_Z is the mass of the Z-boson.

Charged Current

The CC differential cross section for the scattering of polarized electrons with polarization P off unpolarized protons ($e^\pm p \to \nu/\bar{\nu}X$) is given by:

$$\frac{d^2\sigma_{CC}^\pm}{dxdQ^2} = (1 \pm P)\frac{G_F^2}{2\pi x}\left(\frac{M_W^2}{Q^2 + M_W^2}\right)^2 \tilde{\sigma}_{CC}^\pm, \tag{2.10}$$

with

$$\tilde{\sigma}_{CC}^+ = x\left[\bar{u}(x,Q^2) + \bar{c}(x,Q^2) + (1-y^2)\left(d(x,Q^2) + s(x,Q^2)\right)\right], \tag{2.11}$$

$$\tilde{\sigma}_{CC}^- = x\left[u(x,Q^2) + c(x,Q^2) + (1-y^2)\left(\bar{d}(x,Q^2) + \bar{s}(x,Q^2)\right)\right]. \tag{2.12}$$

Here, G_F is the Fermi coupling constant, M_W is the mass of the W-boson, and $q(x, Q^2)$, $\bar{q}(x, Q^2)$ are the PDFs. Eq. 2.11 and Eq. 2.12 reflect the fact that in CC DIS electrons (positrons) can only interact with positively (negatively) charged quarks.

From the vector-axial vector structure of weak interactions, it follows that right-handed neutrinos and left-handed antineutrinos are absent in the Standard Model (if neutrinos are assumed to be massless). Due to helicity conservation, only left-handed electrons and right-handed positrons participate in CC interactions, and thus the cross section has a linear polarization-dependence.

Figure 2.2 shows the unpolarized NC and CC differential cross sections ($d\sigma/dQ^2$) for e^-p and e^+p collisions as measured by H1 and ZEUS. At low Q^2 ($Q^2 \ll M_W^2$), the CC cross section is suppressed due to the W mass. The cross sections become comparable at $Q^2 \approx M_W^2$.

Also visible are the differences between electron and positron data. The NC e^- cross section is larger than the NC e^+ cross section because the structure function xF_3 contributes with different sign (Eq. 2.5). This is due to the vector-axial vector structure of the Z-boson coupling.

The difference between the e^- and the e^+ CC cross sections has two reasons. First, at larger values of x, where the sea quark density is very small, the CC e^- cross section (Eq. 2.12) is dominated by the u quark density while the CC e^+ cross section (Eq. 2.11) is dominated by the d quark density. Second, the antiquark contribution in the CC e^- cross section and the quark contribution in the CC e^+ cross section are suppressed by a factor of $(1-y^2)$, due to the vector-axial vector structure of the W-boson coupling. Thus, neglecting the sea quark densities, the CC e^- cross section is proportional to $u(x, Q^2)$, whereas the CC e^+ cross section is proportional to $(1-y^2)\, d(x, Q^2)$ and therefore smaller than the CC e^- cross section.

The vector-axial vector structure of the Z and W boson couplings is also responsible for the polarization dependence of the cross sections. For NC, only the contributions from Z boson exchange are polarization-dependent. Since, for low values of Q^2, this contributions are suppressed by the Z mass, the effect is increasing with Q^2. The $e_L^- p$ cross section is larger than the unpolarized e^-p cross section and the $e_R^- p$ cross section is smaller. Figure 2.3 shows the ratio of the differential cross section as a function of Q^2 for an electron beam with positive polarization $P_e = 0.29$ and an electron beam with negative polarization $P_e = -0.27$ [9]. In a similar way, the cross section for $e_R^+ p$ scattering is larger

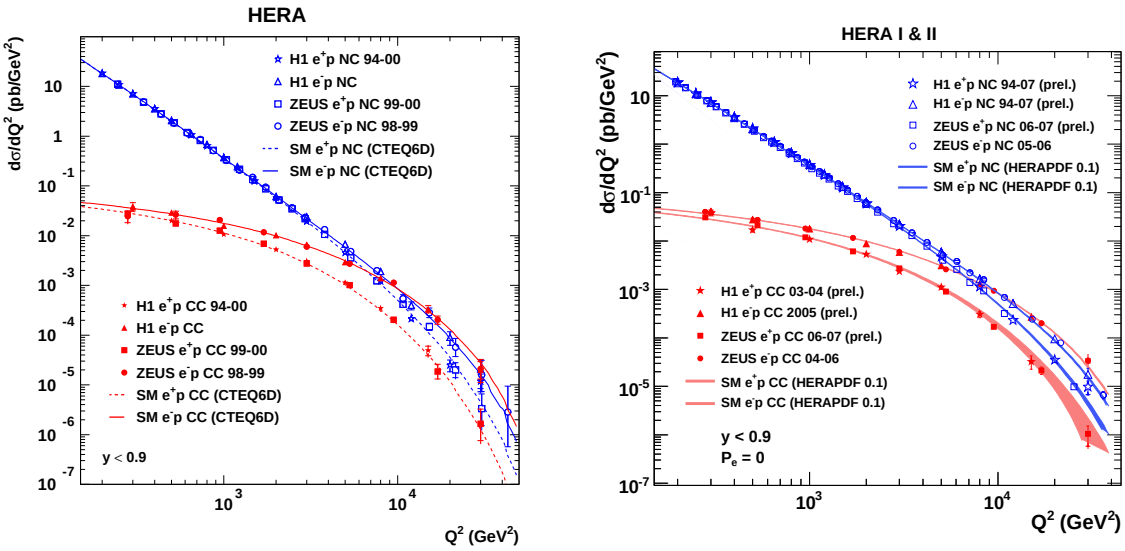

Figure 2.2: *Differential cross section $d\sigma/dQ^2$ for neutral current and charged current DIS at HERA, seperately for e^+p and e^-p interactions [6, 7, 8]. The curves show the SM predictions for these cross sections evaluated using the PDF sets indicated in the plots.*

than the unpolarized e^+p cross section and the $e^+_L\,p$ cross section is smaller.

As already mentioned, only left-handed electrons and right-handed positrons participate in CC DIS, and thus the cross section (Eq. 2.10) has a linear dependence on the polarization. The e^-p cross section is expected to be zero for $P = 1$ and maximal for $P = -1$, and v.v. for the e^+p cross section. Figure 2.4 shows the total CC cross sections for both e^-p and e^+p data as a function of the polarization [10].

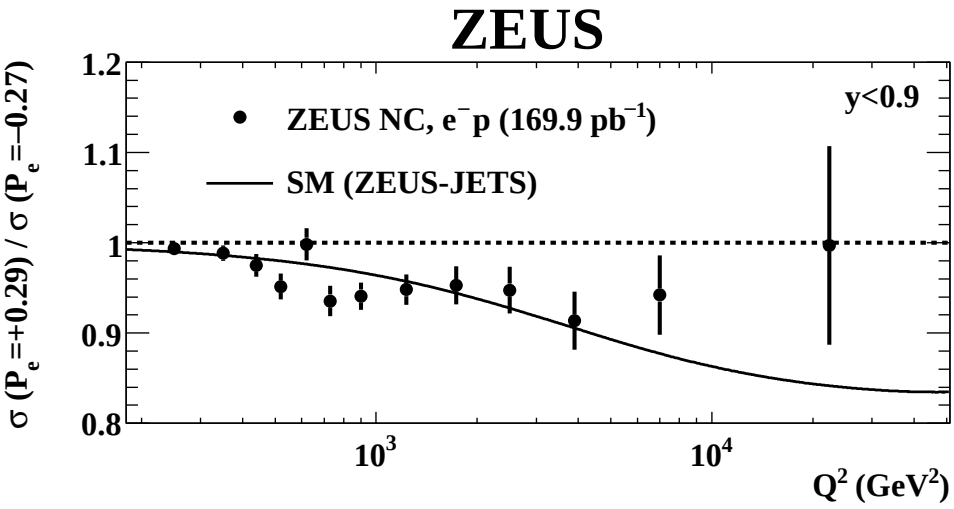

Figure 2.3: *The ratio of the differential cross sections $d\sigma/dQ^2$ for lepton beams with positive and negative polarization [9].*

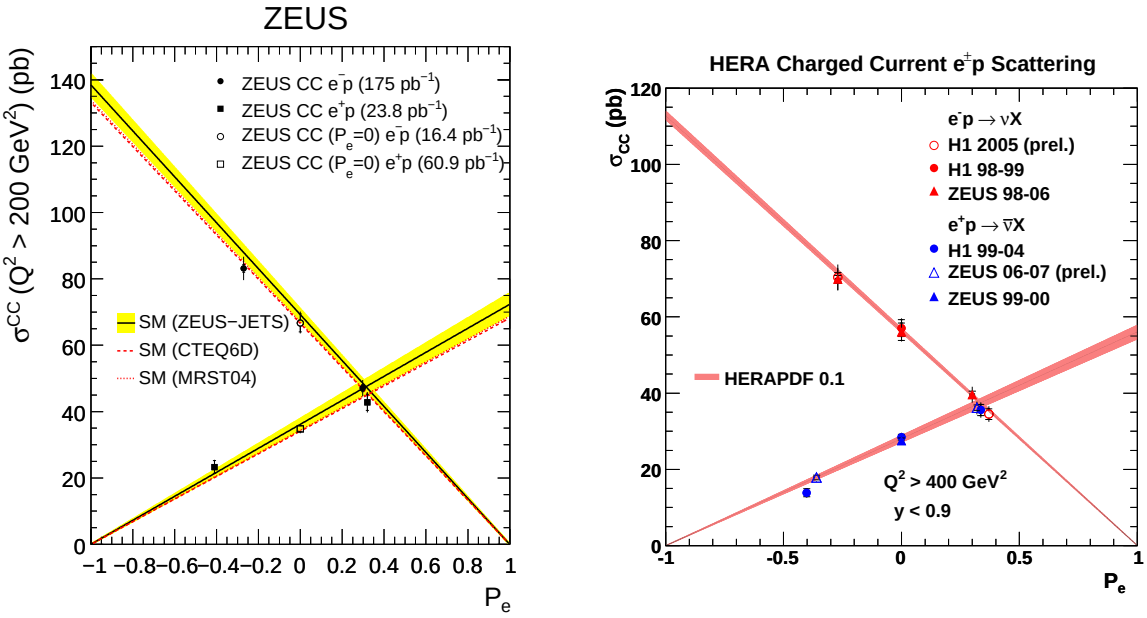

Figure 2.4: *Total e^-p and e^+p CC DIS cross section as a function of the polarization of the lepton beam [10, 8]. The lines show the SM predictions for these cross sections evaluated using different PDF sets.*

2.4 Physics Beyond the Standard Model

2.4.1 Grand Unified Theories

Many different extensions of the Standard Model aim for a connection between the lepton and the quark sector. In Grand Unified theories (GUTs) [11, 12, 2] the electroweak and the strong force are unified. The Standard model symmetry group $SU(3) \times SU(2) \times U(1)$ is embedded in the gauge group of the GUT. There are different GUT models, many of which imply the existence of gauge bosons carrying both lepton and baryon number (leptoquarks). In GUTs an energy scale exists at which the gauge couplings are unified. This scale is of the order of $10^{15}-10^{16}$ GeV. In so-called SUSY GUTs [13, 2], the low energy particle spectrum contains the SM particles as well as their supersymmetric partners (Section 2.4.6).

The simplest model that unifies electroweak and strong interactions is the $SU(5)$ model proposed by Georgi and Glashow [11]. However, it leads to disagreement with experimental evidence as for example the gauge coupling unification and the predicted proton lifetime are ruled out by experimental constraints. The problems can be overcome by introducing an extra Higgs representation to the particle content of the Georgi-Glashow scenario. This extended model [14] predicts light scalar leptoquarks which can have masses of the order of $10^2 - 10^3$ GeV, and thus could be observed at HERA. Furthermore, it takes into account massive neutrinos, and gives an explanation of the matter-antimatter asymmetry in the universe.

2.4.2 The Buchmüller-Rückl-Wyler Model

The Buchmüller-Rückl-Wyler (BRW) model [3] is a general leptoquark model that assumes the existence of a higher symmetry connecting leptons and quarks, like for example it is the case in Grand Unified Theories (Section 2.4.1). In the BRW model, the $SU(3) \times SU(2) \times U(1)$ symmetry of the Standard Model, as well as lepton and baryon number, are conserved. Leptoquarks with lepton or baryon number violating couplings would lead to rapid proton decays. From experimental constraints on flavor violating couplings, it follows that the leptoquark couplings are flavor diagonal (unless the couplings are very small or the leptoquarks are very heavy) [15, 16]. From limits on pion decays, it follows that leptoquarks with masses of order 100 GeV can have sizeable couplings only to left- or to right-handed leptons [16].

Taking into account these constraints, the BRW model predicts 7 scalar and 7 vector

isomultiplets (plus the corresponding anti-leptoquarks) for each fermion generation. Leptoquarks that couple to first generation fermions are called first generation leptoquarks, and this naming scheme extends to all generations. The LQs are classified according to their fermion number $|F| = |L + 3B|$, where L is the lepton number and B is the baryon number of the leptoquark. The fermion number can take the values 0 or 2.

In the BRW model, leptoquarks have only two free parameters: their mass M_{LQ} and their Yukawa coupling λ. For first generation leptoquarks, λ is the coupling of the leptoquark to an electron or electron neutrino and an up or down type quark. Only 4 out of the 14 leptoquark types can be found in an isospin state with couplings to both eq and νq. Assuming that there are no additional interactions, the branching fractions into eq and νq are assumed to be 0.5 for these isospin states. The different leptoquark states within an isospin multiplet are assumed to have the same mass.

2.4.3 Leptoquarks at HERA

The leptoquark states predicted by the BRW model are listed in Table 2.1, where the notation follows the Aachen convention [17]. Isospin states that can only couple to νq and thus cannot be produced in electron-proton collisions are not shown in the Table. By definition, the LQ quantum numbers as well as the production and decay channels corresponds to LQs produced in $e^- q$ collsions. Different LQ species are named according to their spin (S for scalar and V for vector), the chirality of the incoming lepton (L or R), and the weak isospin I^W of the leptoquarks $(0, 1/2, 1)$. The leptoquarks $\tilde{S}$ and $\tilde{V}$ differ by two units of weak hypercharge $Y^W = 2(Q - I_3^W)$ from S and V, respectively, where Q is the electric charge of the leptoquark. In addition, the electric charge Q, the production channel, as well as the allowed decay channels with their branching fractions are shown. The corresponding anti-leptoquarks, which can be produced in $e^+ q$ collisions, have opposite electric charge, and the helicity of the incoming lepton is reversed. Quarks (antiquarks) are replaced by the corresponding antiquark (quark).

As mentioned in Section 2.4.2, only 4 out of the 14 leptoquark types can be found in an isospin state with couplings to both eq and νq. Thus only four LQ types can be produced in ep collisions and decay to neutrino and quark.

At HERA, leptoquarks can be exchanged in the s-channel and the u-channel. Since these processes have the same initial and final state as NC (or CC) DIS, they can interfere with the SM process. Figure 2.5 shows the Feynman diagrams for the s-channel and u-channel leptoquark exchange, as well as for the SM DIS process. The total cross section

LQ species	Charge	F	Production	Decay	Branching ratio
$S^L_{1/2}$	-5/3	0	$e_L\bar{u}$	$e\bar{u}$	1
$S^R_{1/2}$	-5/3	0	$e_R\bar{u}$	$e\bar{u}$	1
	-2/3	0	$e_R\bar{d}$	$e\bar{d}$	1
$\tilde{S}^L_{1/2}$	-2/3	0	$e_L\bar{d}$	$e\bar{d}$	1
V^L_0	-2/3	0	$e_L\bar{d}$	$e\bar{d}$	1/2
				$\nu_e\bar{u}$	1/2
V^R_0	-2/3	0	$e_R\bar{d}$	$e\bar{d}$	1
$\tilde{V}^R_0$	-5/3	0	$e_R\bar{u}$	$e\bar{u}$	1
V^L_1	-5/3	0	$e_L\bar{u}$	$e\bar{u}$	1
	-2/3	0	$e_L\bar{d}$	$e\bar{d}$	1/2
				$\nu_e\bar{u}$	1/2
S^L_0	-1/3	2	e_Lu	eu	1/2
				ν_ed	1/2
S^R_0	-1/3	2	e_Ru	eu	1
$\tilde{S}^R_0$	-4/3	2	e_Rd	ed	1
S^L_1	-1/3	2	e_Lu	eu	1/2
				ν_ed	1/2
	-4/3	2	e_Ld	ed	1
$V^L_{1/2}$	-4/3	2	e_Ld	ed	1
$V^R_{1/2}$	-4/3	2	e_Rd	ed	1
	-1/3	2	e_Ru	eu	1
$\tilde{V}^L_{1/2}$	-1/3	2	e_Lu	eu	1

Table 2.1: *The BRW model leptoquark states that can be produced in e^-p collisions. The upper block shows leptoquarks with fermion number $F \equiv L + 3B = 0$, and the lower block shows leptoquarks with $F = 2$.*

for the process $e^{\pm}p \to e^{\pm}(\nu)X$ contains the following five terms:

$$\sigma(e^{\pm}p \to e^{\pm}(\nu)X) = \sigma_{SM} + \sigma^{Int}_{s/SM} + \sigma^{Int}_{u/SM} + \sigma_s + \sigma_u. \tag{2.13}$$

For $M_{LQ} < \sqrt{s}$, leptoquarks may be produced as resonances (the leptoquark exchanged

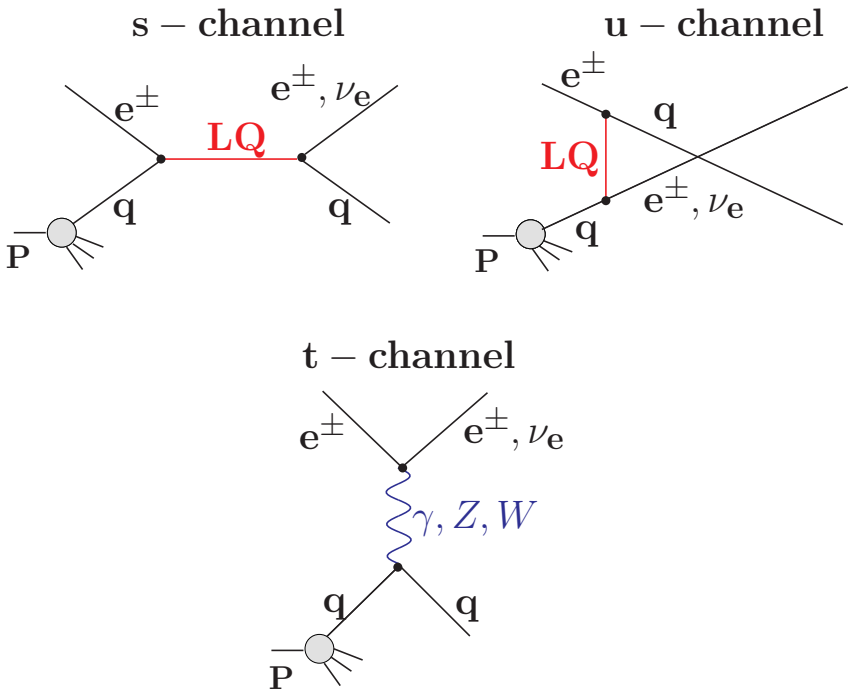

Figure 2.5: *Leptoquark exchange in the s-channel and the u-channel in $e^{\pm}p$ collisions and the SM DIS process.*

in the s-channel is real) and subsequently decay into electron (neutrino) and quark. This would lead to a peak in the invariant mass spectrum of the final state. For masses up to $\sqrt{s}$ the leptoquark contribution to the DIS cross section is dominated by resonance production, especially if the leptoquark is produced from a valence quark. This is the case for the production of leptoquarks with F=2 in e^-p scattering and leptoquarks with F=0 in e^+p scattering. Figure 2.6a) shows the $e^-p \to e^-X$ differential cross section $d^2\sigma/dxdy$ with and without a contribution from a S_0^R leptoquark state ($F = 2$) as a function of x. The value of y is fixed at $y = 0.1$ and the LQ state is assumed to have a mass of 200 GeV and a Yukawa coupling $\lambda = 0.3$ (this value corresponds to the electromagnetic coupling $g = \sqrt{4\pi\alpha_{em}} \approx 0.3$). Figure 2.6b) shows the same cross section with the SM contribution subtracted, leaving the s-channel and the u-channel leptoquark exchange terms and their interference with the SM (Eq. 2.13). The s-channel term and its interference with the SM are also indicated seperately, the u-channel and its interference with the SM are negligible

and thus not shown. The plots show a resonance peak that overshoots the SM-only cross section by two orders of magnitude. The contribution of the s-channel interference term is negligible at the peak, but clearly visible to its sides. Both an increase or a decrease of the SM cross section are possible, depending on the sign of the interference term.

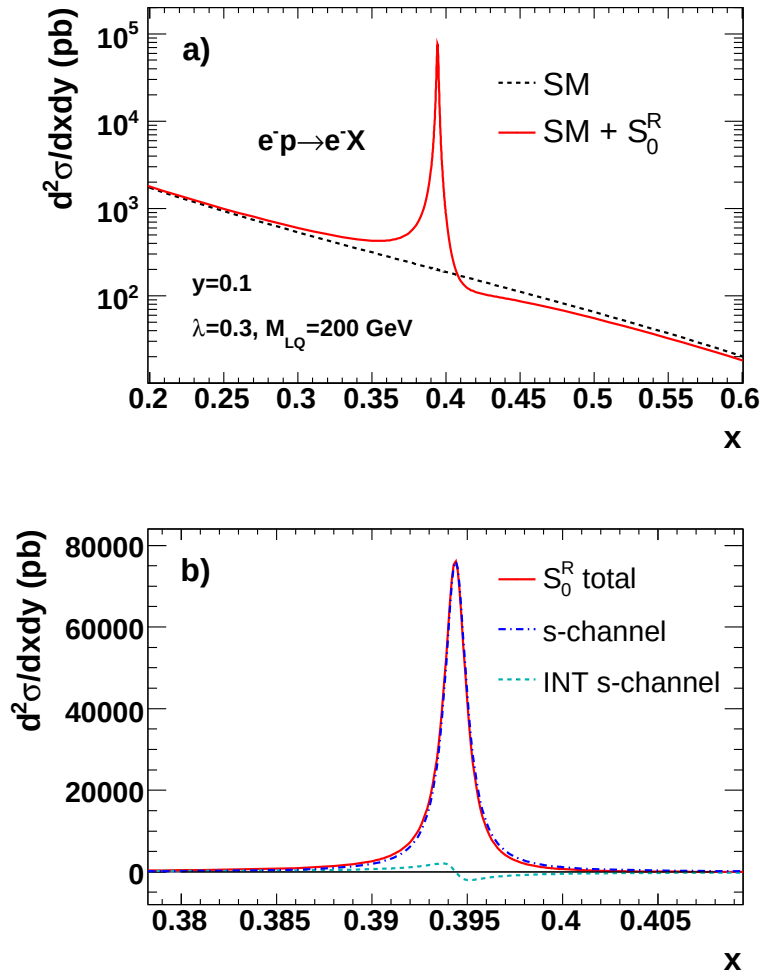

Figure 2.6: *The $e^- p \to e^- X$ differential cross section as a function of x at $y = 0.1$, a) with and without a contribution from a S_0^R leptoquark state, b) only the additional contribution from a S_0^R leptoquark state, as well as the important terms (s-channel LQ exchange and its interference with the SM process) separately. The leptoquark is assumed to have a mass of 200 GeV and a coupling $\lambda = 0.3$.*

The partial decay width of a leptoquark is given by

$$\Gamma_{LQ} = \frac{\lambda^2 M_{LQ}}{8\pi(J+2)}, \tag{2.14}$$

where λ is the Yukawa coupling (lepton-quark-leptoquark coupling) and J is the spin of the leptoquark. Assuming λ of the order of the electromagnetic coupling $g \approx 0.3$, the width of a leptoquark with a mass of 300 GeV is smaller than 1 GeV. For small decay widths, the narrow-width approximation (NWA) of the cross section is valid, which for the resonance production of leptoquarks reads [3]:

$$\sigma^{NWA} = (J+1)\frac{\pi}{4s}\lambda^2 q(x_0, \mu^2), \tag{2.15}$$

where $q(x_0, \mu^2)$ is the quark density in the proton evaluated at $x_0 = m_{LQ}^2/s$ and $\mu^2 = m_{LQ}^2$ is taken to be the factorization scale.

For $M_{LQ} > \sqrt{s}$, all cross section terms given in Eq. 2.13 are important. The presence of a leptoquark would lead to an increase or a decrease of the high-x and high-Q^2 NC and CC DIS cross sections with respect to the SM predictions, depending on the sign of the interference term.

Leptoquarks and DIS events are characterized by a different y-dependence of the differential cross section $d\sigma/dy$. The NC and CC DIS cross sections are roughly proportional[2] to $1/y^2$. The leptoquark s-channel exchange term (the dominant term for $M_{LQ} < \sqrt{s}$) is independent of y for scalar leptoquarks, and proportional to $(1-y^2)$ for vector LQs. Since the DIS cross section falls more rapidly in y than the cross section for vector LQs, and the cross section for scalar LQs is even independent of y, the signal to background ratio can be improved by restricting the LQ search to the region of large y. Furthermore, if a LQ resonance is seen, the y distribution could indicate whether the resonant state is a scalar or a vector leptoquark. Since y is related to the lepton scattering angle $\theta^\star$ in the lepton-quark center-of-mass-system by Eq. 2.2, the region of negative $\cos\theta^\star$ is most sensitive to leptoquark searches.

Since leptoquarks in the BRW model couple only to left-handed or to right-handed fermions, the LQ cross section has a linear polarization-dependence, as the CC DIS cross section (Eq. 2.10). Depending on the LQ type, the polarization can enter in the LQ and the CC DIS cross sections with equal or opposite sign. The NC DIS cross section has a weaker polarization dependence (Eq. 2.4). Since data samples with different polarization are analyzed separately, the analysis is sensitive to the differences in the polarization dependence between LQ and DIS cross sections.

[2]This is not true for very low values of y in CC DIS, as well as for low y in NC DIS if the kinematic region is restricted to very high values of Q^2. This is due to the mass of the W and the Z boson for CC and NC DIS, respectively.

2.4.4 Leptoquark Interactions at Other Colliders

Tevatron

The Tevatron is a proton-antiproton collider with a center of mass energy of up to 1.96 TeV. Searches for leptoquarks are performed by the two collider experiments CDF and D0. Leptoquarks can be pair produced ([18], Figure 2.7), primarily via strong interactions in quark-antiquark annihilation and gluon-gluon fusion. For $M_{LQ} > 100$ GeV, the $q\bar{q}$ annihilation (Figure 2.7a) is the dominating process. The production is independent of the lepton-quark-leptoquark Yukawa coupling (except for a negligible contribution from the process in Figure 2.7b). For vector LQs the production cross section depends on the gVV and the $ggVV$ couplings (where g is a gluon and V a vector LQ) which are unknown [19] and thus assumptions have to be made.

At the Tevatron, all the three generations of leptoquarks can be produced. In contrast to HERA, second and third generation LQs can be produced without flavor violating couplings. First generation LQs would decay to a quark and an electron (neutrino), and thus the possible final states are $eejj$, $e\nu jj$, and $\nu\nu jj$, where j is a jet originating from an up or down quark or antiquark.

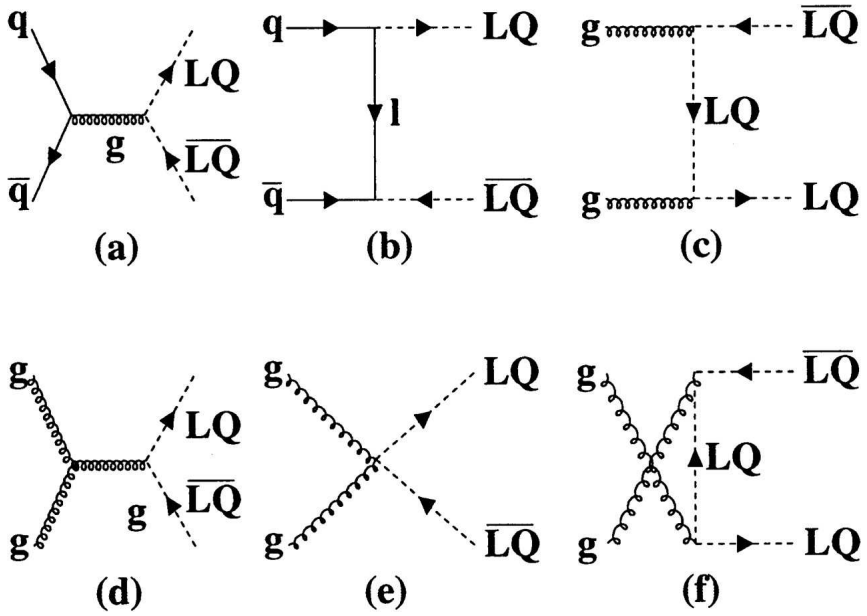

Figure 2.7: *Leading-order Feynman diagrams for leptoquark pair production at the Tevatron [20].*

LEP

LEP was an electron-positron collider operating at a center-of-mass energy of up to 209 GeV. Searches for leptoquarks were performed by all four main experiments: ALEPH, DELPHI, L3 and OPAL. The most stringent leptoquark limits were obtained from a search for indirect effects in the process $e^+e^- \to q\bar{q}$. First generation leptoquarks can contribute to this process if they are exchanged in the t-channel ($F = 0$) or in the u-channel ($F = 2$) ([21], Figure 2.8). These processes depend on the Yukawa coupling λ.

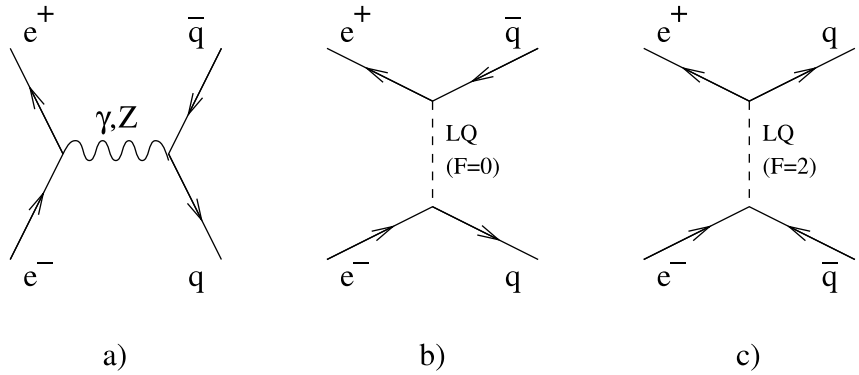

Figure 2.8: *Leptoquark exchange in b) the t-channel and c) the u-channel in the process $e^+e^- \to q\bar{q}$ and a) the SM DIS process [21].*

2.4.5 Contact Interactions

Four-fermion contact interactions are an effective theory which allows to describe low energy effects from physics at much higher energy scales. Heavy leptoquark exchange ($M_{LQ} \gg \sqrt{s}$) at HERA can be described by a vector-type $eeqq$ or $e\nu qq$ four-fermion contact interaction [22]. The effective coupling is proportional to λ^2/M_{LQ}^2, the square of the ratio of the leptoquark Yukawa coupling to the leptoquark mass. Thus, the cross section depends only on the ratio λ/M_{LQ}. Both s-channel and u-channel LQ exchange are important at high LQ masses. A heavy LQ contribution to the SM would lead to an increase or a decrease of the high-x and high-Q^2 NC and CC DIS cross sections with respect to the SM predictions, depending on the sign of the interference term.

2.4.6 R-parity Violating Supersymmetry

The Minimal Supersymmetric Standard Model (MSSM) [23] is considered as a promising candidate for a theory beyond the Standard Model. In the MSSM, each particle has a su-

persymmetric partner particle (superpartner). The spins of a particle and its superpartner differ by $\frac{1}{2}$, thus for each fermion a supersymmetric boson exists and vice versa.

Lepton and baryon number conservation is not explicitly postulated in the MSSM. They might have been violated by non-perturbative electroweak effects that played a role in the early universe but are negligible at ordinary energies. Instead, the conservation of a multiplicative quantum number called R-parity is assumed in most MSSM scenarios. The R-parity of a particle is defined as:

$$R = (-1)^{L+3B+2S}, \tag{2.16}$$

where L is the lepton number, B is the baryon number and S is the spin of the particle. The R-parity is +1 for all SM particles and -1 for their superpartners. This means that the lightest supersymmetric particle is stable and, if it is electrically neutral, is a candidate for non-baryonic dark matter in the universe.

In some extensions of the MSSM the R-parity is not a conserved quantum number [24]. This means that lepton and baryon number cannot be both conserved. However, if they were both violated at ordinary energies, this would lead to rapid proton decays. Thus only one of them can be violated. If the lepton number is not conserved, processes with electron-quark-squark[3] couplings are possible.

At HERA, this means that the same processes as in Figure 2.5 are possible in R-parity violating supersymmetry if instead of the leptoquark state $\tilde{S}^L_{1/2}$ an up-type squark $\tilde{u}_L$ is exchanged, or instead of S^L_0 a down-type squark $\tilde{d}_R$ is exchanged [25]. An important difference is that leptoquarks carry both lepton and baryon number, whereas squarks carry only baryon number and the conservation of the lepton number is violated by the interaction. The limit obtained for the Yukawa coupling of the $\tilde{S}^L_{1/2}$ (S^L_0) would be identical to the limit on the R-parity violating coupling of $\tilde{u}_L$ to eq ($\tilde{d}_R$ to eq and νq) if the branching fractions to eq and νq were the same for LQs and squarks. However, squarks can decay also into gaugino (chargino, neutralino or gluino)[4] and quark, depending on the masses of these particles. Thus, only limits on $\lambda\sqrt{\beta}$ can be obtained in this analysis, where β is the unknown branching fraction of the squarks to lepton (e or ν) and quark. The branching fractions of the squarks to eq and νq are assumed to be $\beta_{eq} = \beta,\ \beta_{\nu q} = 0$ for $\tilde{u}_L$, and $\beta_{eq} = 0.5\,\beta,\ \beta_{\nu q} = 0.5\,\beta$ for $\tilde{d}_R$.

[3] Squarks are the scalar superpartners of quarks.

[4] Charginos and Neutralinos are mixing states of the superpartners of electroweak gauge bosons and Higgs bosons. The gluino is the superpartner of the gluon.

2.5 Monte Carlo Simulation

The measured event distributions cannot be directly compared to model predictions and thus are compared to events generated with Monte Carlo (MC) simulations. Furthermore, the MC events are used to test different reconstruction methods considered for the analysis, and to estimate the efficiency of the event selection.

NC and CC DIS events were simulated using HERACLES [26] with the DJANGOH 1.6 [27, 28] interface to the hadronization programs. Electroweak radiative effects (initial and final state radiation, vertex and propagator corrections, as well as two-boson exchange were included in the simulation. The CTEQ5D PDFs [29] were used in the cross section calculation. The hadronic final state was simulated with ARIADNE [30], which uses the color dipole model. The hadronization was modelled by JETSET [31], which uses the Lund string model. To take into account the effect of the polarization in the measured data, the MC was reweighted. In the case of NC DIS where the cross section has a non-linear polarization-dependence (Eq. 2.4), this is done using predictions from HECTOR [32].

Leptoquark Monte Carlo samples were used to estimate the resolution of different reconstruction methods for the invariant mass of the final state, which corresponds to the leptoquark mass. Different samples for scalar leptoquark states with fixed masses between 130 and 290 GeV were simulated using PYTHIA 6.1 [33]. Only the s-channel contribution is considered. Initial state radiation from the electron, initial and final state QCD radiation from the quark and the effect of LQ hadronization before decay [34] are taken into account.

The generated MC events are processed through the ZEUS detector and trigger simulation programs, and then reconstructed in the same way as real data (Section 3.3 and Chapter 4).

Chapter 3

The ZEUS Experiment at HERA

3.1 The HERA Accelerator

The HERA (**H***adron* **E***lektron* **R***ing* **A***nlage*) collider was located in Hamburg, Germany, at DESY (**D***eutsches* **E***lektronen* **SY***nchrotron*). Up to now, it was the only electron–proton collider in the world, offering unique opportunities to explore the structure of the proton and to study various processes involving strong, electromagnetic and weak interactions.

HERA was running from 1992-2007. It was located underground inside a tunnel and consisted of one storage ring for protons and one for electrons[1]. The circumference was 6.3 km. Electrons and protons were accelerated independently in opposite directions. The electrons and protons reached an energy of 27.5 GeV and 920 GeV (820 GeV until 1997), respectively. The resulting center–of–mass energy was 318 GeV (300 GeV until 1997).

Four experiments were situated on the HERA ring, two collider experiments (H1 and ZEUS) and two fixed target experiments (HERMES and HERA-B). At H1 and ZEUS, electrons and protons collided head-on at zero crossing angle. HERMES used only the electron beam and HERA-B only the proton beam. HERMES [35] was investigating the spin structure of the nucleon and HERA-B [36] aimed to study the $\mathcal{CP}$ –violation in the $B^0\overline{B^0}$ -system.

Figure 3.3 shows the layout of the HERA collider, with the four experimental halls and the system of pre–accelerators used for initial acceleration of electron and proton beams. In the first step electrons and protons were accelerated using linear accelerators. A small storage ring PIA (Positron-Intensity-Accumulator) could be used after the linear

[1]Unless otherwise specified, 'electron' refers to both positron and electron.

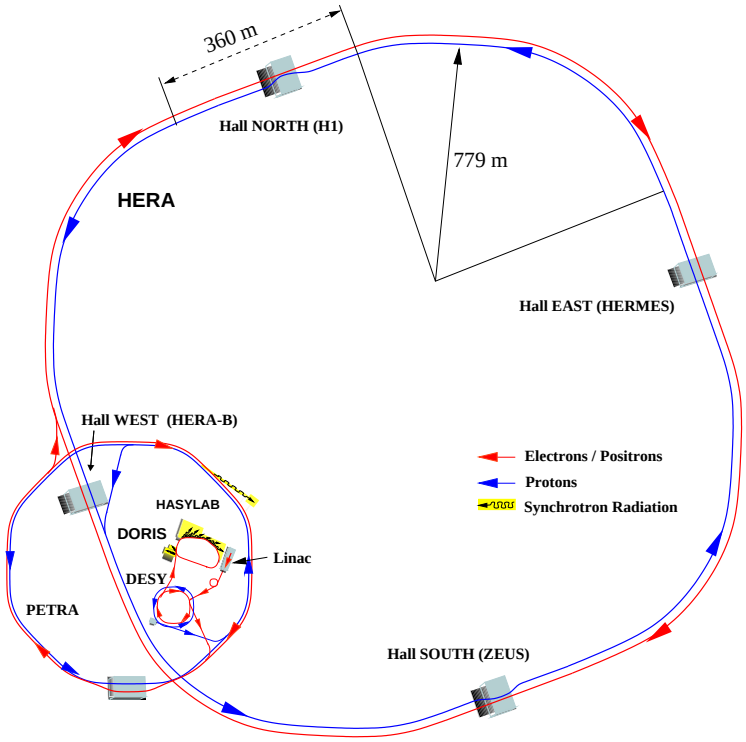

Figure 3.1: *A schematic view of the HERA collider and the pre-accelerators. The H1 detector was located in the north hall and the ZEUS detector in the south hall.*

accelerator to accumulate positrons. In the next step the particles were injected into the DESY II (electrons) and DESY III (protons) accelerators and accelerated to 7.5 GeV. After injection into PETRA and further acceleration, 12 GeV electrons and 40 GeV protons were injected into HERA.

The running of HERA was divided into two data taking periods known as HERA-I and HERA-II. Between these periods, a luminosity upgrade was made and spin rotators (Section 3.1.1) were installed for the H1 and ZEUS experiments. Both the HERA-I and the HERA-II periods can be divided into subperiods. The HERA-I subperiods are characterized by different lepton beam charge and proton beam energy, while the HERA-II subperiods are characterized by different lepton beam charge and longitudinal lepton beam polarization. In the HERA-I period, the lepton beam was longitudinally unpolarized. Figure 3.2 shows the integrated luminosity taken by the ZEUS detector as a function of days of running.

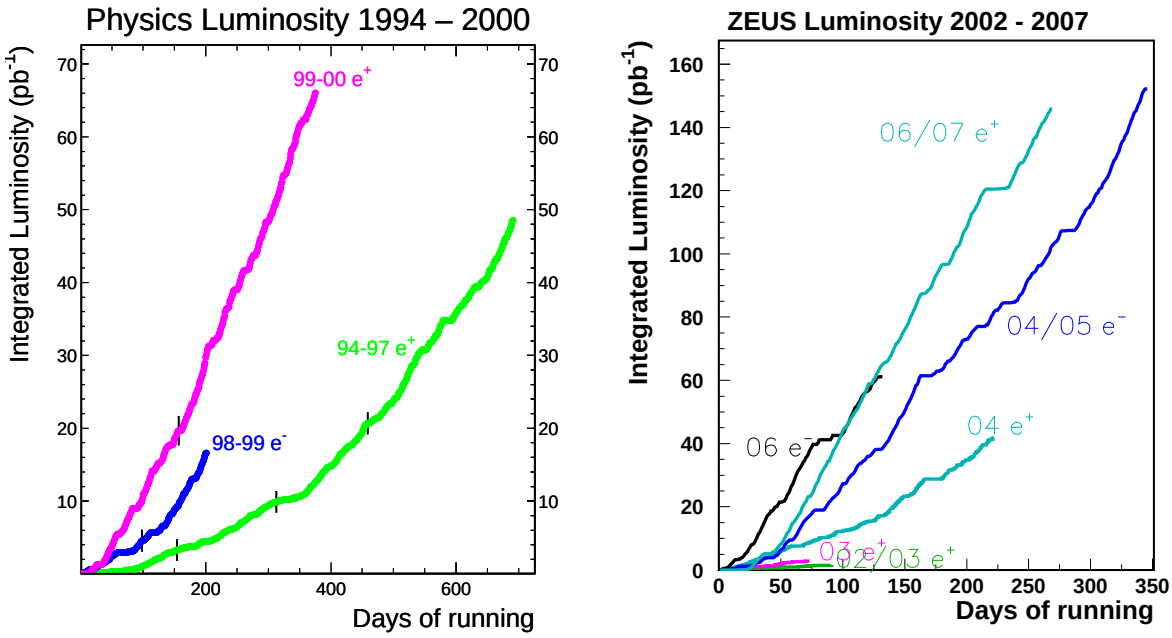

Figure 3.2: *Integrated luminosity taken with the ZEUS detector as a function of days of running. The left plot shows the HERA-I subperiods, the right plot shows the HERA-II subperiods.*

3.1.1 Polarization at HERA

At HERA, transverse polarization of the electron beam built up naturally due to the Sokolov-Ternov-effect [37] with a build-up time of approximately 40 minutes. However, of interest is the longitudinal polarization since the projection of the spin of a particle in the direction of its motion defines its helicity. Longitudinal polarization at HERA was achieved via spin rotators [38] that converted the transverse polarization into longitudinal polarization (and vice versa to ensure the preservation of the polarization around the ring). They were installed in the shutdown between the HERA-I and the HERA-II data taking periods.[2] The polarization of the electron beam was measured by two independent polarimeters, the Transverse Polarimeter (TPOL) [39] and the Longitudinal Polarimeter (LPOL) [40]. The spin-dependence of the Compton scattering cross section of circularly polarized photons on polarized leptons was used to determine the polarization. The typical level of polarization at HERA was 30-40%. The relative uncertainty on the polarization measurement was 4.2% for TPOL and 3.6% for LPOL. Figure 3.3 shows the location of the spin rotators and of the two polarimeters.

[2]The spin rotators for HERMES were already installed in 1994.

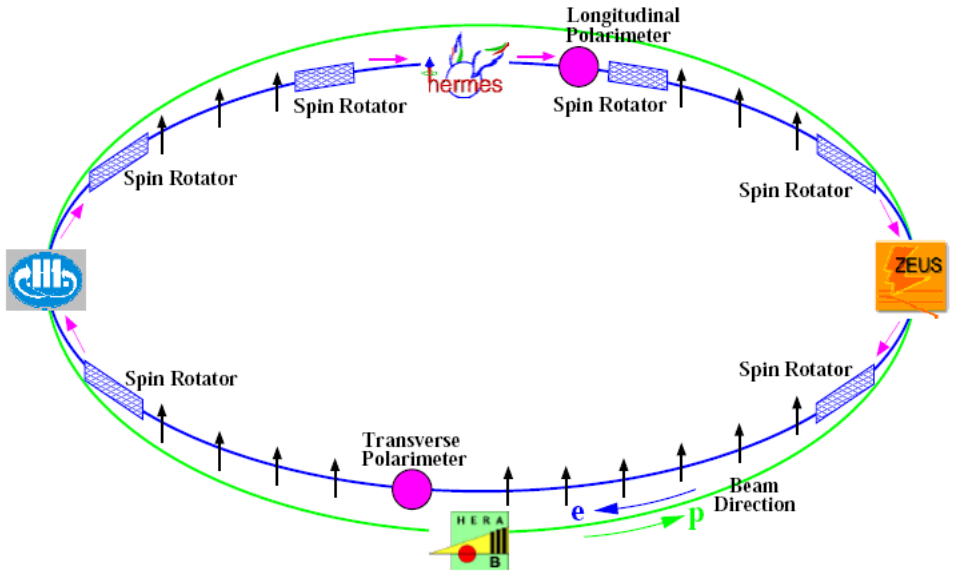

Figure 3.3: *A schematic view of HERA showing the location of the spin rotators, polarimeters and experiments. The blue line represents the electron beam with the arrows denoting transverse or longitudinal polarization.*

3.2 The ZEUS Detector

The ZEUS detector [41] was a general purpose detector designed to study various aspects of electron–proton scattering. It was in operation from 1992 to 2007. Different components were used to measure final state hadrons and leptons and to characterize the observed final state in terms of particle energy, direction and type. The experiment consisted of the main detector surrounding the nominal interaction point and several small components positioned along the beam line on either side of the detector.

The ZEUS geometry is described using a right-handed coordinate system with its origin at the nominal interaction point. The Z-axis points in the direction of the incoming protons. The X-axis points horizontally towards the center of HERA and the Y-axis points upwards. A schematic view of the main detector is shown in Figures 3.4 and 3.5 (cross section along and perpendicular to the beam direction, respectively).

The design of the detector is not symmetric with respect to the nominal interaction point ($z = 0$). The difference in the energy of the electron beam (27.5 GeV) and the proton beam (820/920 GeV) resulted in a large boost of the center-of-mass system in the direction of the proton beam and in a large forward–backward asymmetry of the particle production. Therefore the forward part of the detector was better equipped to deal with highly energetic particles than the rear part.

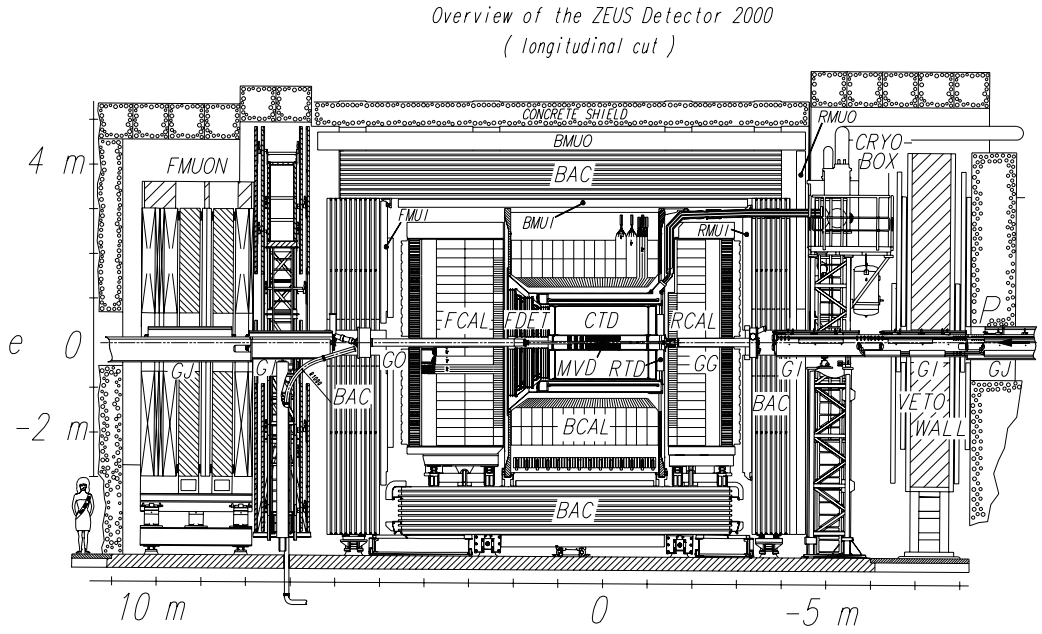

Figure 3.4: *View of the ZEUS detector along the beam direction. Electrons enter from the left and protons enter from the right. See text for a description of the components.*

The inner part of the main detector consisted of the tracking system enclosed by a thin superconducting solenoid producing an axial magnetic field of 1.43 T. The main components of the tracking system were the Central Tracking Detector (CTD) and the Microvertex Detector (MVD). They were arranged cylindrically around the beam pipe, the MVD was the inner component. The CTD was a drift chamber, the MVD was a silicon strip detector. They will be described in more detail in Sections 3.2.1 and 3.2.2, respectively. CTD and MVD are supplemented by forward and rear tracking detectors (FDET and RTD).

The Uranium Calorimeter (CAL) was located outside the solenoid. The CAL is divided into a forward part (FCAL), a barrel part (BCAL), and a rear part (RCAL). It will be described in more detail in Section 3.2.3.

The CAL was surrounded by an iron yoke providing a return path for the magnetic field flux of the solenoid. Furthermore, it is instrumented with proportional chambers making it possible to measure energy leakage out of the CAL and to reconstruct high energy muons. The yoke is therefore referred to as the backing calorimeter (BAC). Since the return field of the solenoid is too small and nonuniform to measure the muon momentum, the yoke was in addition magnetized to 1.6 T by copper coils producing a toroidal field. Further muon detectors are located inside (FMUI, BMUI, RMUI) and outside (FMUO,

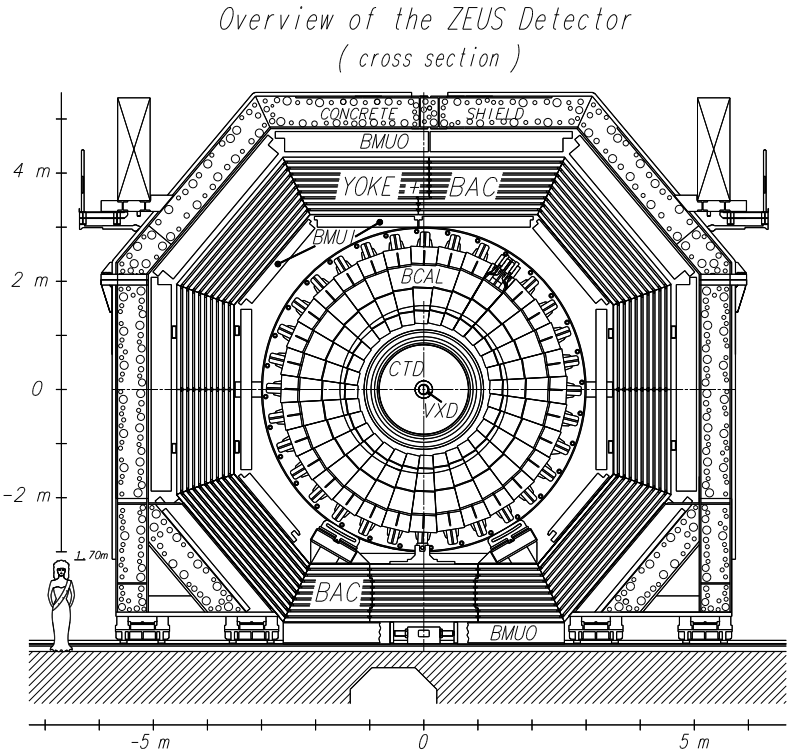

Figure 3.5: *View of the ZEUS detector perpendicular to the beam direction. See text for a description of the components. The vertex detector (VXD) was not in use after 1994; during the upgrade between the HERA–I and HERA–II running periods the MVD was installed at the same position.*

BMUO, RMUO) the iron yoke.

The detectors used for luminosity measurement were located outside the central ZEUS detector and will be described in more detail in section 3.2.4.

3.2.1 The Central Tracking Detector (CTD)

The CTD [42] was a cylindrical drift chamber which provided a high precision measurement of the position, direction and momentum of charged particles produced in *ep* collisions. Furthermore, the measurement of the mean energy loss dE/dx of charged particles along their tracks allowed to distinguish different particle types.

The superconducting solenoid that enclosed the CTD produced a magnetic field of 1.43 T parallel to the beam pipe. The curvature of the track in the magnetic field provided information about charge and momentum of the charged particles.

The chamber was filled with a mixture of argon, CO_2 and ethane. It covered the polar angle range $15° < \theta < 164°$ and the full range in the azimuthal angle ϕ. Its active

volume had a length of 205 cm, an inner radius of 18.2 cm and an outer radius of 79.4 cm. The CTD was a multi-layer drift chamber. It was divided into octants and had nine superlayers. Figure 3.6 shows a CTD octant.

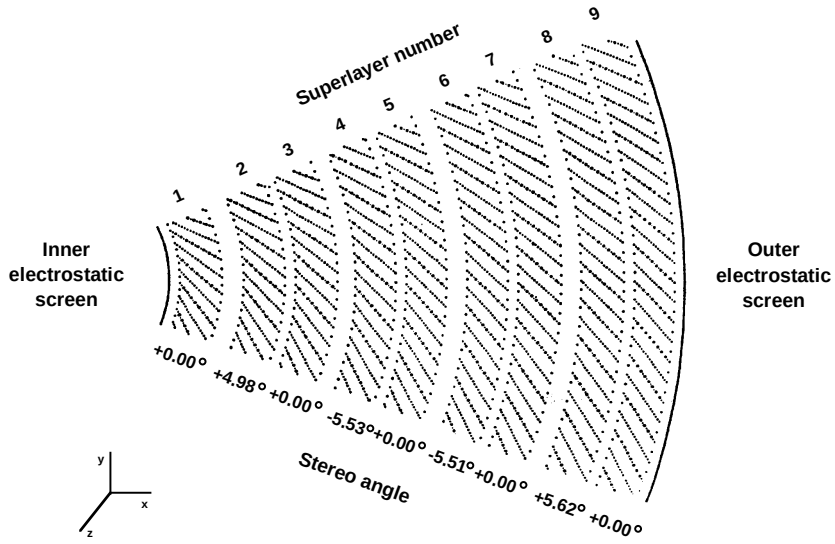

Figure 3.6: *Layout of a CTD octant. Each octant had nine superlayers.*

Charged particles traversing the CTD ionized the gas and the produced electrons drifted towards the sense wires. In the high electric field close to the wires they produced further electron–ion pairs; typically the signal was amplified by a factor $10^4 - 10^5$. The magnetic field tilted the path of the drift electrons by a Lorentz angle of 45° with respect to the radial direction. To take into account this effect, the wire planes were oriented at the same angle.

The odd–numbered superlayers had sense wires parallel to the beam axis, while the sense wires of the even–numbered superlayers were tilted by ±5° with respect to the beam axis ('Stereo angle' in Figure 3.6). In this way the measurement of the z coordinate was possible. The achieved resolution was ≈ 200 μm in the $r - \phi$ plane and ≈ 2 mm in the z coordinate. The resolution of the transverse momentum p_T of tracks traversing through all the 9 superlayers was in the HERA–I data taking period [43]:

$$\frac{\sigma(p_T)}{p_T} = 0.0058 \cdot p_T(\text{GeV}) \oplus 0.0065 \oplus \frac{0.0014}{p_T}, \tag{3.1}$$

where $\oplus$ denotes the quadratic sum. The first term is related to the resolution of the CTD hits, while the second and third term arise from multiple scattering within and before the CTD, respectively.

3.2.2 The Microvertex Detector (MVD)

The MVD [44] was a silicon strip detector positioned between the beam pipe and the inner radius of the CTD. It consisted of a barrel section with three cylindrical layers and a forward section with four planar layers perpendicular to the HERA beam direction. The MVD improved the vertex reconstruction and extended the tracking acceptance.

3.2.3 The Uranium Calorimeter (CAL)

The CAL [45] was a sampling calorimeter which consisted of alternating layers of absorber (depleted uranium) and detector (plastic scintillator) material of a thickness 3.3 mm and 2.6 mm, respectively. When a particle entered the absorber, it generated secondary particles. These shower particles produced light in the scintillator which is detected as described later. Different types of incoming particles cause different shower shapes: electromagnetic showers induced by electrons or photons start as soon as the particle enters the CAL and are much less penetrating than hadronic showers, which are deeper and broader. The CAL was a compensating calorimeter, which means that the response to electromagnetic and hadronic particles was equal. This led to a very good hadronic energy resolution of $\sigma_E/E = 0.35/\sqrt{E(\mathrm{GeV})}$. The electromagnetic energy resolution was $\sigma_E/E = 0.18/\sqrt{E(\mathrm{GeV})}$.

The CAL was almost hermetic with a solid angle coverage of 99.7%. It was divided into three parts, as shown in Figure 3.7: the forward (FCAL), barrel (BCAL) and rear (RCAL) calorimeter. To account for the boost of the center–of–mass in the direction of the proton beam, the FCAL had a total depth of 7.1 hadronic interaction length, whereas the BCAL (RCAL) had a total depth of 5.3 (4.0) interaction length. The polar angle coverage was $2.2 - 39.9^\circ$ for FCAL, $36.7 - 129.1^\circ$ for BCAL and $128.1 - 176.5^\circ$ for RCAL.

The three calorimeter parts are subdivided into modules. FCAL and RCAL are divided vertically into modules with the module face perpendicular to the beam axis. The BCAL modules were wedge-shaped and each covered 11.25° in azimuthal angle. The modules were transversally separated into towers and the towers were in turn longitudinally divided into electromagnetic (EMC) and hadronic (HAC) sections. In FCAL and BCAL, the EMC section was divided transversally into four cells, while the HAC section was divided longitudinally into two cells (HAC1 and HAC2). In RCAL only the EMC section of a tower is divided into two cells.

To read out the scintillator plates, two wavelength shifters were attached to each cell on both sides of the module. The light from the wavelength shifters was transferred via

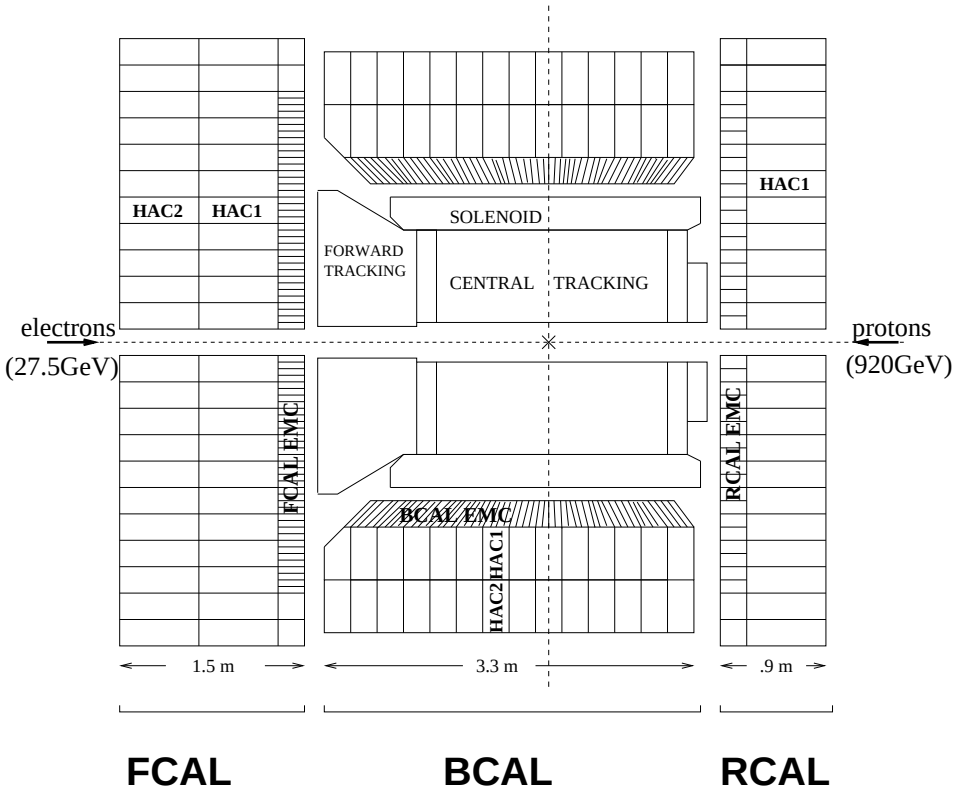

Figure 3.7: *Layout of the ZEUS Uranium Calorimeter along the beam direction.*

light guides to photomultipliers placed behind the module. Since each cell was read out on two sides, it was possible to reconstruct the particle position in the cell.

The natural radioactivity of ^{238}U was used as a reference signal to calibrate the readout channels to a precision of $< 1\%$. The time resolution was < 1 ns for energy deposits greater than 4.5 GeV and thus the timing information could be used to reject non-ep background.

3.2.4 The Luminosity Measurement

The luminosity of ep–collisions at HERA was determined from the measurement of the rate of the bremsstrahlung process $ep \to e\gamma p$ (Bethe–Heitler process [46])[3]. The luminosity at the ZEUS detector was measured by two independent detectors: the Photon Calorimeter (PCAL) [47] and the Spectrometer (SPEC) [48]. Both detectors measured the Bethe–Heitler photons. The luminosity is given by

$$L = \frac{R}{\sigma \mathcal{A}}, \tag{3.2}$$

[3]This process is chosen because the cross section is large and theoretically well known, which minimizes both the statistical and the theoretical error on the luminosity measurement.

where R is the observed rate of Bethe–Heitler events, σ is the Bethe–Heitler cross section and $\mathcal{A}$ is the acceptance of the luminosity detector (PCAL or SPEC).

PCAL

The PCAL measured the rate of the Bethe–Heitler photons using a lead–scintillator sampling calorimeter positioned $z = 107$ m from the interaction point. To shield the calorimeter from synchrotron radiation, a set of carbon filters was placed in front of it. Since thess filters worsened the energy resolution, two Cherenkov detectors measured the number of electron-positron pairs produced by the Bethe–Heitler photons as they passed through the filters.

The electron scattered in the Bethe–Heitler process had a lower energy than the beam electrons and thus was bent at a different angle by the beam magnets. Is was detected in another lead–scintillator sampling calorimeter positioned 35 m from the interaction point. The detection of the Bethe–Heitler electrons was used for systematic studies of the PCAL measurement.

The systematic uncertainty on the PCAL luminosity measurement is 2.5 %.

SPEC

The SPEC detected Bethe–Heitler photons through their pair conversion, $\gamma \rightarrow e^+e^-$, in material. When the photons left the beam pipe at about 92 m from the nominal interaction point, they passed through a 3 mm thick window made of copper (90 %) and Beryllium (10 %), and around 10 % of the photons converted into e^+e^- pairs. These e^+e^- pairs were split by a dipole magnet and detected by two tungsten–scintillator calorimeters. The luminosity was measured from the rate of coincidence in the two calorimeters. The systematic uncertainty on the SPEC luminosity measurement is 2.6 %.

3.2.5 Trigger and Data Acquisition Systems

The time between two bunch crossings at HERA was 96 ns, which is equivalent to a rate of about 10 MHz. The total interaction rate was 10-100 kHz and was dominated by background from upstream interactions of the proton beam with residual gas in the beam pipe. Other important background sources were electron-beam-gas collisions, beam halo and cosmic muon events. For most types of interesting ep physics events the event rate was only of the order of a few Hz. The purpose of the trigger [49] was to separate the interesting ep events from the background events, in particular because the event rate

needed to be reduced to a few Hz to make the events recordable. The trigger was based on three levels, as shown in Figure 3.8.

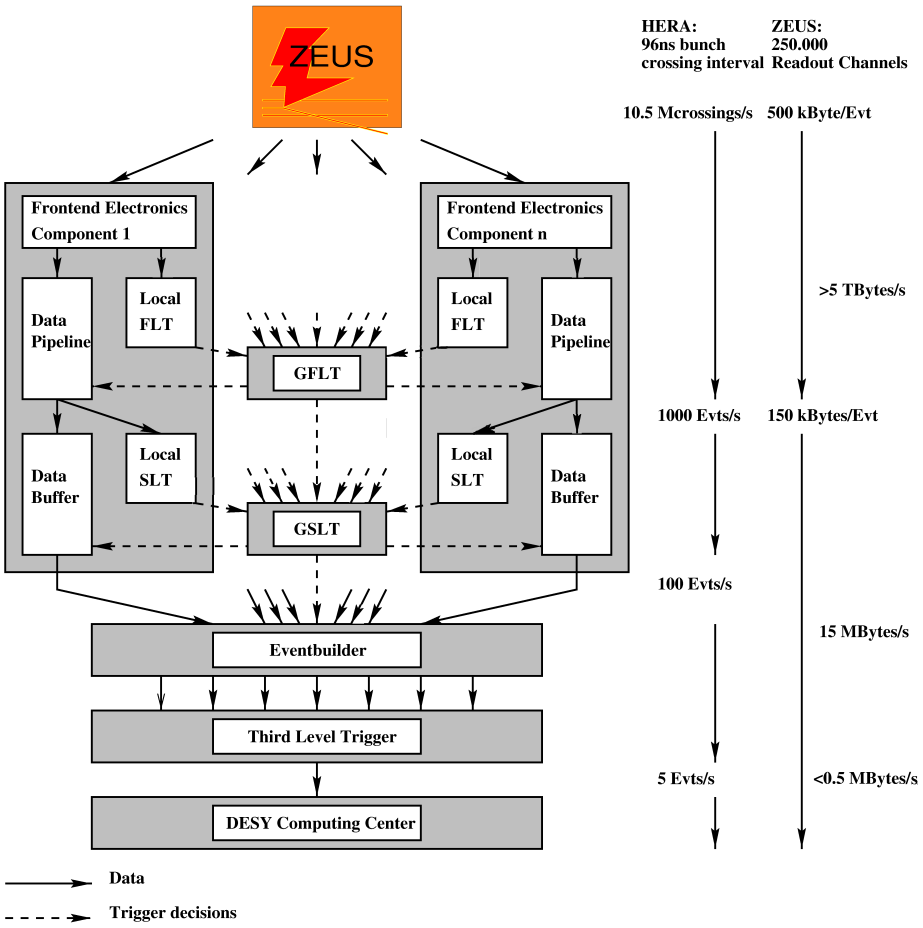

Figure 3.8: *Schematic diagram of the ZEUS trigger and data acquisition systems. The approximate event rate is shown on the right.*

- **First Level Trigger (FLT):** the FLT [50] was a hardware trigger that reduced the event rate to < 1 kHz. Each detector component had its own local FLT which provided the trigger information within 2 μs after the bunch crossing. This information was send to the Global First Level Trigger (GFLT), which decided whether to accept or reject the event and passed this decision back to the components within 4.4 μs. To avoid deadtime, each component stored the raw data in an analog or digital pipeline during the decision process. The relevant information used at the GFLT was based on UCAL energies (e.g. total transverse energy, missing transverse momentum), CTD tracks (e.g. number of tracks, vertex position) and hits in the muon chambers.

- **Second Level Trigger (SLT):** if the event was accepted by the GFLT, the raw data measured by each component was transferred from the data pipeline to a data buffer and to the local SLT. Due to the lower input rate and the depth of the buffer, $\sim$ 10 ms were available for the trigger decision. Thus the event variables reconstructed at the SLT had a better resolution and new information like CAL timing was available. The local SLTs passed their trigger information to the Gobal Second Level Trigger (GSLT) [51], which, like the GFLT, decided whether to accept or reject the event and passed this decision back to the components. The SLT was designed to reduce the event rate to about 50-100 Hz.

- **Third Level Trigger (TLT):** if an event was accepted by the GSLT, all detector components sent the raw data of this event from the data buffers to the Event Builder (EVB) [52], which stored the data in an ADAMO [53] database record, the data structure used for ZEUS data storage. The TLT [54] consisted of a computer farm and fully reconstructed events basing on the information stored in the ADAMO tables. Sophisticated algorithms like electron finders could be used at this level. The final output rate was 5-10 Hz. If the events passed the TLT, they were stored on tape for reprocessing with complete detector calibrations and full reconstruction software (Section 3.3).

3.3 Event Reconstruction and Analysis

The scheme of the ZEUS offline and Monte Carlo simulation programs is shown in Figure 3.9.

The data events that passed the trigger chain were reconstructed using the program ZEPHYR and were stored on tape. Using this information, an offline event analysis is performed by the user using the ORANGE analysis framework. ORANGE is a software library that executes standard ZEUS analysis routines like electron and jet finders, or calorimeter energy corrections.

The program package AMADEUS is used as interface to the Monte Carlo event generators (Section 2.5) and converts the output record of each simulated event to an ADAMO [53] database record (the same format used to store the real data) for the following simulation of the ZEUS detector response with the programs MOZART and CZAR. MOZART is based on the simulation package GEANT [55] and simulates the interaction of the particles with the detector. CZAR simulates the three trigger levels. Finally, as for the data

events, a full reconstruction of the event is performed using ZEPHYR and the user can do an offline analysis using ORANGE.

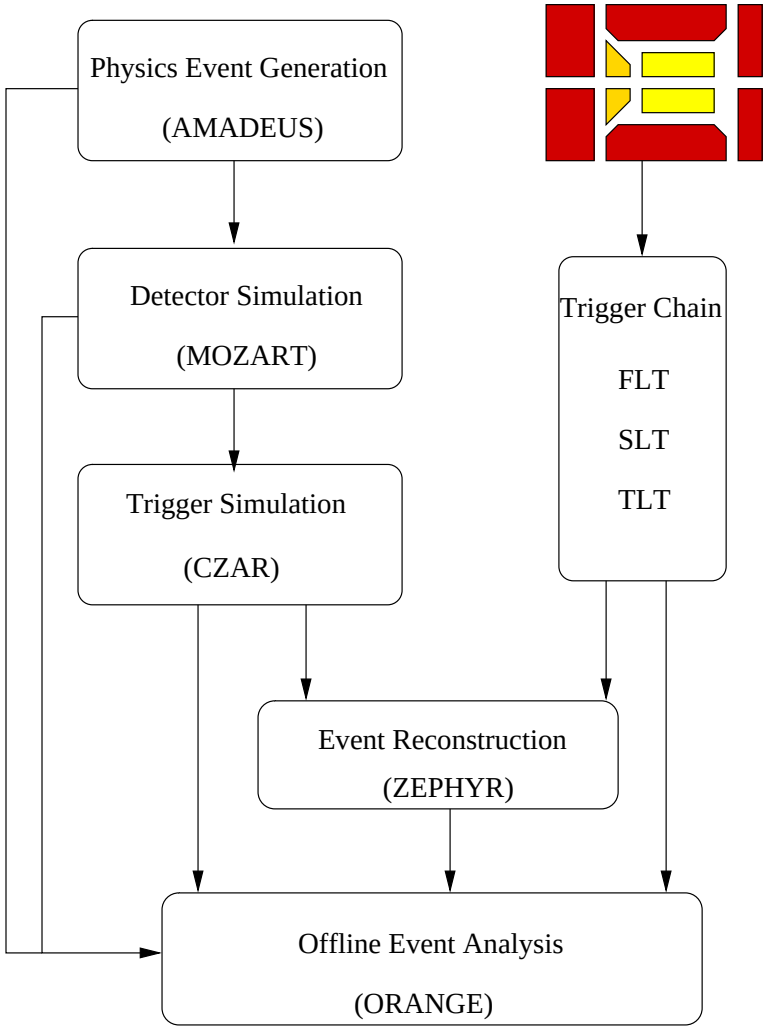

Figure 3.9: *Scheme of the ZEUS offline and Monte Carlo simulation programs, as well as the trigger chain for data events. The left side shows the different steps for simulated events and the right side for data events.*

Chapter 4

Event Selection and Reconstruction

4.1 Data Sets

This analysis is based on data recorded with the ZEUS detector in the years 2003-2007, the so-called HERA-II data taking period (Section 3.1). For the limit setting, these data are combined with the data from the HERA-I period. The HERA-II data are divided in four subsamples: left-handed and right-handed electron data, and left-handed and right-handed positron data. Table 4.1 shows the luminosity and the average longitudinal lepton beam polarization for the different subsamples. In total, data with an integrated luminosity of 356.1 pb^{-1} (352.7 pb^{-1}) for NC (CC) were analyzed. Only runs fulfilling data quality cuts ensuring that the necessary detector components were properly functioning are used.

For the polarization measurement, the polarimeter (LPOL and TPOL, Section 3.1.1) that had a longer up-time during each run (in terms of ZEUS gated luminosity) was used. If the up-times were equal, the polarization measured by the LPOL is used since the uncertainty is smaller than for the TPOL. Runs for which both LPOL and TPOL were not working are discarded from this analysis. Figure 4.1 shows the integrated luminosity as a function of the lepton beam polarization for electron and positron data. The plot for the positron data is done with the runs used in the NC analysis. It looks similar for the runs used in the CC analysis.

data set	luminosity (pb^{-1})	pol.
04–06 LH e^-	104.5	-0.27
04–06 RH e^-	79.1	0.30
03–07 LH e^+	75.7 (NC), 72.3 (CC)	-0.37
03–07 RH e^+	96.8	0.32

Table 4.1: *Integrated luminosity and average polarization of the different data sets.*

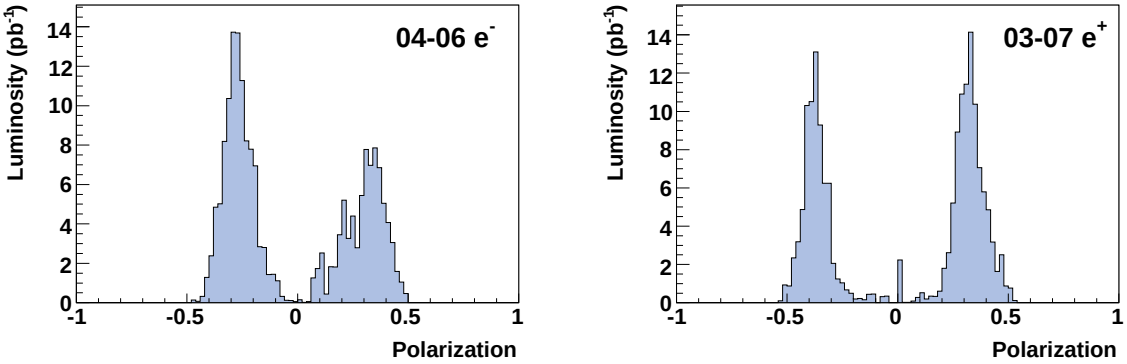

Figure 4.1: *Integrated luminosity as a function of the lepton beam polarization for electron and positron data.*

4.2 Electron and Jet Reconstruction

4.2.1 Electron Identification

The EM electron finder [56, 57] evaluates whether a calorimeter energy cluster (in this analysis reconstructed as a cone island [56, 58]) is compatible with an electron energy deposit. Several cuts based on calorimeter information [57] are applied to the cluster. If a cluster passes these cuts and is inside the CTD acceptance, it is checked if a matching track exists. For candidate clusters outside the CTD acceptance or without a matching track, four variables based on calorimeter information are used to evaluate the probability that the cluster belongs to an electron. These variables are the fraction of the cluster energy measured in the HAC layers, the energy deposited close to the electron[1] but not belonging to the electron (later referred to as $E_{cone,had}$), and parameters related to the width of the electron shower. For candidate clusters with a matching track, three

[1]The area close to the electron is defined as a cone with radius $R_{cone} = \sqrt{(\Delta\phi)^2 + (\Delta\eta)^2} = 0.8$, where η is the pseudorapidity, $\eta = -\ln(\tan\frac{\theta}{2})$.

additional variables based on tracking information are used: the difference in polar and azimuthal angle between the track and the calorimeter cluster and the energy difference of the particle evaluated using tracking and calorimeter information. Each of these four (or seven) variables is converted into a sub-probability; these sub-probabilities are then combined to an overall probability that the cluster is an electron. Eventually, the electron candidates are sorted according to this global probability.

4.2.2 Jet Finding Algorithm

In DIS, the final state contains one or more jets originating from the hadronization of the scattered quark and possible particles from QCD initial or final state radiation. In this analysis, the longitudinally invariant[2] k_T-clustering algorithm in inclusive mode [59] is used to reconstruct jets.

The algorithm starts from a list of protojets, which are CAL cone islands [56, 58] in this analysis, and an empty list of jets. It proceeds recursively as follows:

1. For each protojet i, a parameter d_i is defined as:

$$d_i = E_{T,i}^2, \tag{4.1}$$

   and for each pair i and j of protojets, a parameter d_{ij} is defined:

$$d_{ij} = \min(E_{T,i}^2, E_{T,j}^2) \left[(\eta_i - \eta_j)^2 + (\phi_i - \phi_j)^2\right], \tag{4.2}$$

   where $E_{T,i}$, η_i, and ϕ_i are the transverse energy, the pseudorapidity, and the azimuthal angle of jet i. The transverse energy is defined as $E_{T,i} = E_i \sin\theta_i$, where E_i and θ_i are energy and polar angle of jet i.

2. The smallest of all the d_i and d_{ij} is labelled d_{min}.

3. If d_{min} is of type d_{ij}, the protojets i and j have nearly parallel momenta and thus are merged to a new protojet k by:

$$\begin{aligned} E_{T,k} &= E_{T,i} + E_{T,j}\ , & (4.3)\\ \eta_k &= \left(E_{T,i}\eta_i + E_{T,j}\eta_j\right)/E_{T,k}\ , & (4.4)\\ \phi_k &= \left(E_{T,i}\phi_i + E_{T,j}\phi_j\right)/E_{T,k}\ , & (4.5) \end{aligned}$$

   assuming that the protojets have negligible masses.

[2] The algorithm is invariant under Lorentz boosts along the z-direction.

4. If d_{min} is of type d_i, no other protojet is close to protojet i. It is removed from the list of protojets and added to the list of jets.

5. Start again at point 1 until the list of protojets is empty.

4.3 Reconstruction of the Calorimetric Variables

The total transverse energy E_T, the total transverse momentum p_T and the difference between the energy and the longitudinal momentum , $E - P_z$, are calculated as follows from calorimeter information:

$$E_T = \sum_i E_i \sin\theta_i, \tag{4.6}$$

$$p_T^2 = p_x^2 + p_y^2 = \left(\sum_i E_i \sin\theta_i \cos\phi_i\right)^2 + \left(\sum_i E_i \sin\theta_i \sin\phi_i\right)^2, \tag{4.7}$$

$$E - P_z = \sum_i (E_i - p_{z,i}) = \sum_i E_i(1 - \cos\theta_i), \tag{4.8}$$

where the sums run over all CAL cone islands [56, 58].

4.4 Reconstruction of the Kinematic Variables

Different methods exist to reconstruct the kinematic variables x, y, and Q^2 defined in section 2.1. The electron method [60] uses information only from the scattered DIS electron, the Double Angle Method [60] uses electron and hadronic information, and the Jacquet-Blondel method [61] uses information exclusively from the hadronic final state. The electron method and the Double Angle method can only be used if the final state lepton is detected. Since the final state neutrino in CC DIS is not detected, the Jacquet-Blondel method is the only viable method for CC DIS analyses. Therefore, in the discusion of the electron method and the Double Angle method the final state lepton will be referred to as electron.

The Electron Method

The electron method [60] uses the energy E'_e and the scattering angle θ_e of the scattered electron to calculate the kinematic variables. The variables E'_e and θ_e are reconstructed in the laboratory frame. It is assumed that there is no initial state radiation (emission of

a photon from the incoming electron). The kinematic variables are given by:

$$Q_e^2 = 2E_e E'_e(1 + \cos\theta_e), \tag{4.9}$$

$$x_e = \frac{E_e}{E_p} \cdot \frac{E'_e(1 + \cos\theta_e)}{2E_e - E'_e(1 - \cos\theta_e)}, \tag{4.10}$$

$$y_e = 1 - \frac{E'_e}{2E_e}(1 - \cos\theta_e), \tag{4.11}$$

where E_e and E_p are the electron and proton beam energies and the electron scattering angle θ_e is calculated with respect to the proton beam direction ($\theta_e = 180°$ corresponds to no deflection). From Eq.(4.9), it can be seen that electrons in reactions with large Q^2 have large energies E'_e and small θ_e (which means the electrons are scattered under large angles).

The Double Angle Method

The Double Angle method [60] uses the polar angles of the scattered electron, θ_e, and of the scattered quark, γ_h. The polar angle of the scattered quark is calculated via

$$\cos\gamma_h = \frac{P_{T,had}^2 - (E - P_z)_{had}}{P_{T,had}^2 + (E - P_z)_{had}}, \tag{4.12}$$

In this analysis, $P_{T,had}^2$ and $(E - P_z)_{had}$ are calculated as in Equations 4.7 and 4.8, but with the sum running only over the CAL cone islands [56, 58] belonging to the hadronic final state[3].

The kinematic variables are given by:

$$Q_{DA}^2 = \frac{4E_e^2 \sin\gamma_h(1 + \cos\theta_e)}{\sin\gamma_h + \sin\theta_e - \sin(\gamma_h + \theta_e)}, \tag{4.13}$$

$$x_{DA} = \frac{E_e}{E_p} \cdot \frac{\sin\gamma_h + \sin\theta_e + \sin(\gamma_h + \theta_e)}{\sin\gamma_h + \sin\theta_e - \sin(\gamma_h + \theta_e)}, \tag{4.14}$$

$$y_{DA} = \frac{Q_{DA}^2}{s x_{DA}}, \tag{4.15}$$

where E_p denotes the proton beam energy. The unique feature of the DA method is that it does not depend on the absolute energy measurement in the detector, so it is almost

[3]In the CC analysis this means all energy deposits, and in the NC analysis this means all energy deposits except for the one belonging to the highest probability electron candidate found by the EM finder.

insensitive to the calorimeter energy scale uncertainties. The energy of the scattered electron can be calculated as:

$$E_{DA} = \frac{Q^2_{DA}}{2E_e(1+\cos\theta_e)}. \tag{4.16}$$

The Jacquet-Blondel Method

With the Jacquet-Blondel method [61], the kinematic variables are reconstructed exclusively from the energy and momentum of the hadronic final state:

$$y_{JB} = \frac{(E-P_z)_{had}}{2E_e}\,, \tag{4.17}$$

$$Q^2_{JB} = \frac{P^2_{T,had}}{1-y_{JB}}\,, \tag{4.18}$$

$$x_{JB} = \frac{Q^2_{JB}}{sy_{JB}}\,, \tag{4.19}$$

where $(E-P_z)_{had}$ and $P_{T,had}$ are calculated in this analysis as in Eq.(4.8) and Eq.(4.7), with the sum running over all CAL cone islands [56, 58] belonging to the hadronic final. As already mentioned, the Jacquet-Blondel method is the only viable method in case of CC DIS because the final state neutrino is not detected.

Performance of the Reconstruction Methods

The choice of the reconstruction method used in the NC analysis depends on how well it reproduces the true kinematic variables of the MC simulation. To investigate this, the resolutions in x, y, and Q^2 were evaluated using:

$$Res(x) = \frac{x_{rec}-x_{true}}{x_{true}}, \tag{4.20}$$

$$Res(y) = \frac{y_{rec}-y_{true}}{y_{true}}, \tag{4.21}$$

$$Res(Q^2) = \frac{Q^2_{rec}-Q^2_{true}}{Q^2_{true}}, \tag{4.22}$$

where the index *rec* refers to the reconstructed variable and the index *true* refers to the generated variable. The distributions were analyzed in different bins of x, y, and Q^2. If a variable is well reconstructed, the distributions are peaked at zero, while the width of the distribution indicates the resolution of the reconstructed variable. Figures 4.2–4.4 show the distribution of $Res(x)$, $Res(y)$, and $Res(Q^2)$ for the three different reconstruction methods (using the NC DIS MC simulation for left-handed e^- data). The Double Angle

Method performs best in most regions of phase space, only at high y and very high Q^2 the Electron Method performs slightly better. Thus, the kinematic cuts in the NC analysis are generally based on the Double Angle variables.

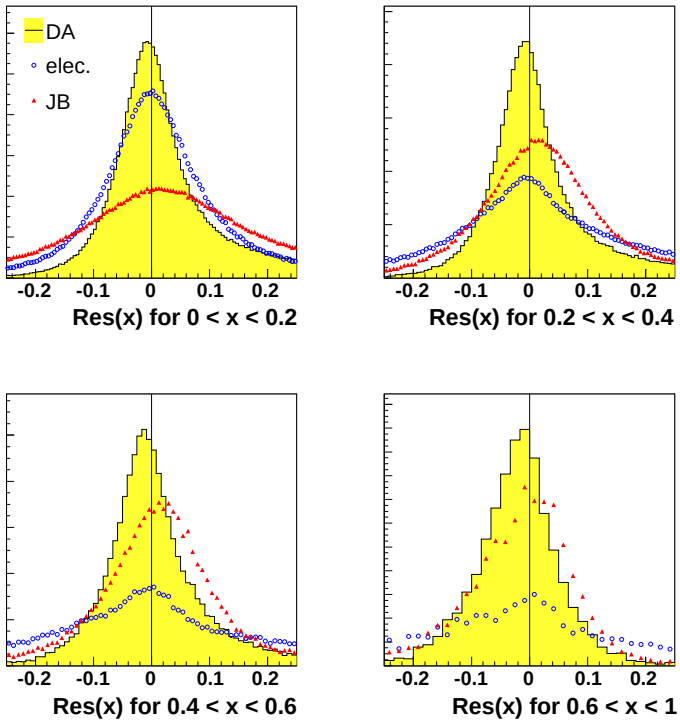

Figure 4.2: *Distribution of Res(x) in different bins of x for the Double Angle method (histogram), the electron method (circles) and the Jacquet-Blondel method (triangles), evaluated using the NC DIS MC simulation for left-handed e^- data.*

4.5 Event Topology and Background Description

The most characteristic feature of NC DIS is the scattered electron, which is deflected at a sufficiently large angle to be seen in the central detector. Typical events have an isolated scattered electron that is balanced in transverse momentum by the hadronic final state. The EM electron finding algorithm (Section 4.2.1, [56, 57]) is used to identify electron candidates. In addition to the scattered electron, at least one jet is found in the final state, originating from the hadronization of the scattered quark. To reconstruct the jets, the k_T-clustering algorithm (Section 4.2.2, [59]) is used . In the final state more than one jet can be present due to QCD final state radiation. Events are discarded in this analysis

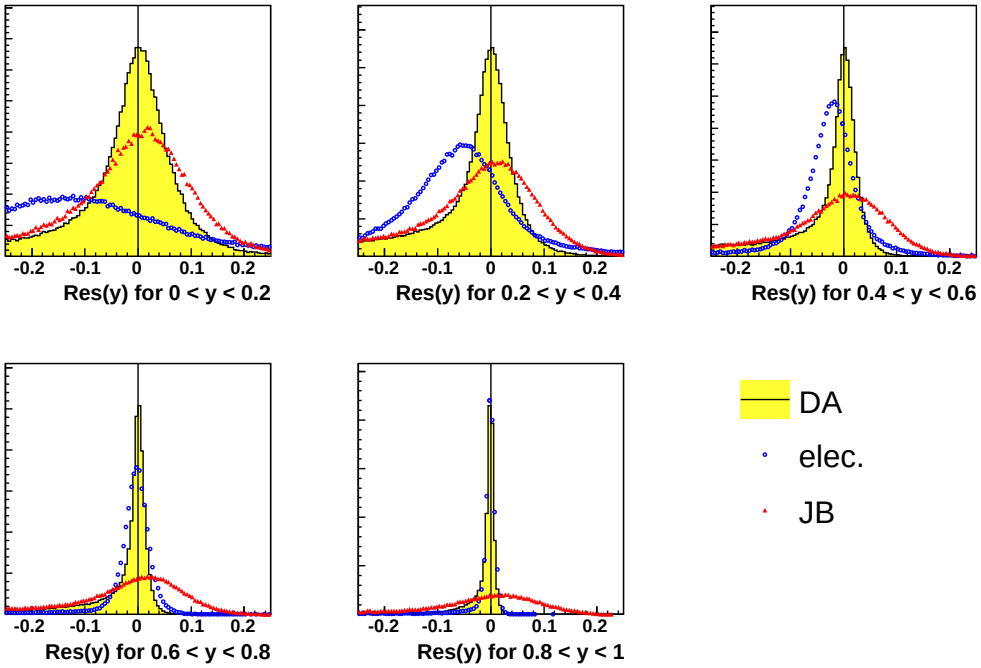

Figure 4.3: *Distribution of Res(y) in different bins of y for the Double Angle method (histogram), the electron method (circles) and the Jacquet-Blondel method (triangles), evaluated using the NC DIS MC simulation for left-handed e^- data.*

in which an electron is found in the final state, compatible with the NC DIS scattered electron, but no jet could be reconstructed, because the jets are used to reconstruct the invariant mass of the final state (Section 4.8).

In CC events the final state neutrino leaves the detector undetected and thus a large missing transverse momentum is the most characteristic feature of CC DIS events. As for NC, at least one jet in the final state is required, and events where no jet could be reconstructed are discarded in this analysis.

Several sources of background to the NC and CC DIS process have been considered and studied. Background events can come from other physical processes occurring in electron-proton collisions. Background can also be due to non *ep* interactions, as for beam-gas interactions or cosmic and halo muon events.

- **Photoproduction Background:** In photoproduction events, a quasi-real photon is exchanged ($Q^2 \approx 0$). At leading order, two different regimes of photoproduction can be distinguished: in direct photoproduction (Fig. 4.5a), the photon behaves like a point-like particle and transfers all its energy to the partons in the proton.

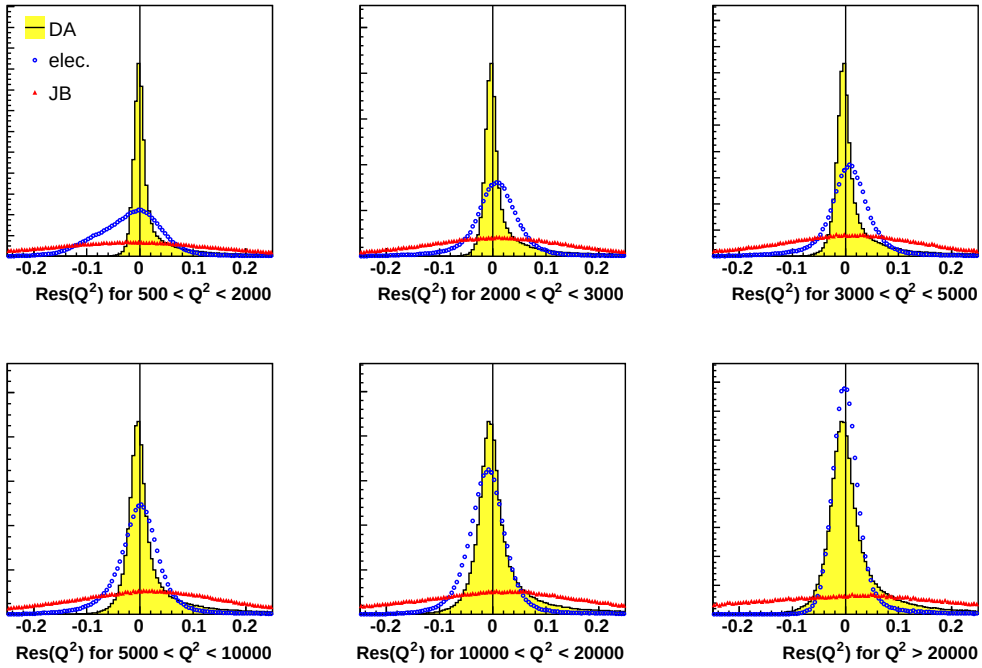

Figure 4.4: *Distribution of $Res(Q^2)$ in different bins of Q^2 for the Double Angle method (histogram), the electron method (circles) and the Jacquet-Blondel method (triangles), evaluated using the NC DIS MC simulation for left-handed e^- data.*

In resolved photoproduction (Fig. 4.5b), the photon can fluctuate into a $q\bar{q}$-pair or form a hadronic bound state. Thus only a fraction of the photon momentum is transferred in the hard interaction.

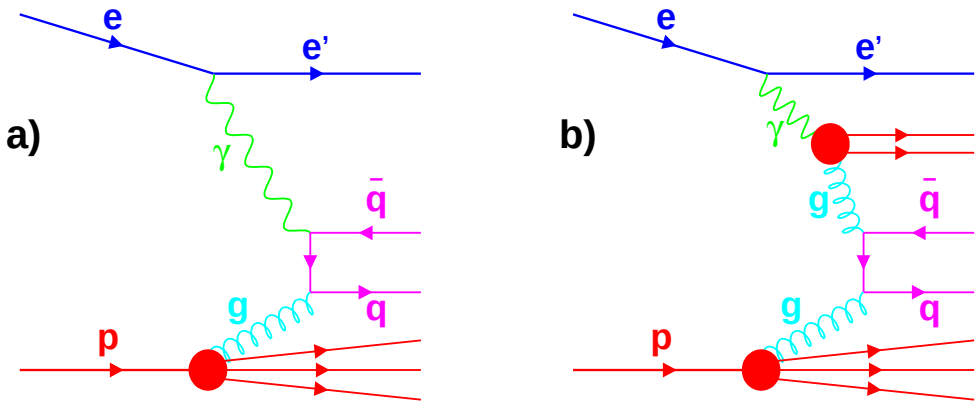

Figure 4.5: *Diagrams of a) direct and b) resolved photoproduction*

Since γ-exchange is proportional to $1/Q^4$, the rate of photoproduction events is much higher than the rate of high-Q^2 NC DIS events. Furthermore, the CC DIS cross section is lower or comparable to the NC DIS cross section (Figure 2.2), and thus the rate of photoproduction events is also higher than the rate of high-Q^2 CC DIS events.

In photoproduction events, the electron is typically scattered at very small angles and lost undetected in the rear beam pipe. Neutral pions resulting from photoproduction events can decay into photons and fake an electron signal in the calorimeter. These events may be falsely classified as NC DIS events. Furthermore, mis-measured jets in photoproduction events can lead to a fake missing transverse momentum and thus these events may be falsely classified as CC DIS events.

- **Beam-gas Interactions:** Even though the beampipe is evacuated, residual gas atoms remain that can interact with the proton or electron beam. Beam-gas interactions can occur outside or inside the detector.

- **Halo and Cosmic Muons:** In inelastic interactions of beam protons with the residual gas, or of protons from the proton halo with components of the HERA accelerator upstream of the detector, charged pions are produced that mainly decay into muons. These so-called halo muons pass through the detector parallel to the proton beam.

  If halo and cosmic muons radiate, they can cause large missing p_T. They also give a small contribution to the NC DIS background because the muon can fake the signal of the scattered DIS electron if it showers in an electromagnetic cell of the calorimeter.

- **Elastic QED Compton Scattering:** In elastic QED compton scattering ($ep \rightarrow e\gamma p$), the proton escapes undetected into the beam pipe. Thus, the measured energy comes almost entirely from the electron and the photon, and they are balanced in transverse momentum. They can fake a DIS electron and a hadronic energy cluster that are balanced in p_T and thus look like the final state of a NC DIS event.

- **NC DIS as Background to CC DIS:** If the energy of the NC DIS electron or a jet is not reconstructed properly, large missing transverse momentum can be measured. These events might pass the CC event selection. Therefore, a NC rejection is done in the CC event selection.

4.6 Neutral Current Selection

4.6.1 NC Events

Events were selected online by using the ZEUS three-level trigger system (Section 3.2.5, [41, 49]). The trigger chains used for the selection of NC DIS events required an energy deposit in the CAL consistent with an isolated electron and timing information from the CAL consistent with an *ep* bunch crossing [9, 62].

The offline event selection is optimized to select the phase-space region with the highest leptoquark-to-SM ratio. Moreover, cleaning cuts are applied to remove background and badly reconstructed events from this region.

- **Kinematic region:** since the NC DIS differential cross section $\frac{d\sigma}{dxdQ^2}$ is approximately proportional to $\frac{1}{xQ^4}$ times the parton distribution function (Eq. 2.4), most NC events are measured at low Q^2 and low x. This region is not of interest in this analysis because the high event rate would hide a possible leptoquark signal. Furthermore, small leptoquark masses are already excluded independent of the size of the Yukawa coupling λ by the D0 and the CDF experiments [63, 64]. The invariant mass of the final state can be calculated via

$$M = \sqrt{xs} = \sqrt{\frac{Q^2}{y}}, \tag{4.23}$$

  where Eq. 2.1 was used. Therefore, events with low Q^2 and low x are not relevant to the LQ search. To restrict the phase space to the most interesting region, cuts on Q^2 and x are applied:

$$Q^2_{DA} > 2500 \text{ GeV}^2, \tag{4.24}$$

$$x_{DA} > 0.1 \tag{4.25}$$

  The distributions of Q^2_{DA} and x_{DA} for left-handed electron data after all selection cuts are shown in Figure 4.10. The distributions for the other three data samples can be found in Appendix A.

  Due to the high Q^2 cut, no events with electrons scattered at large angles θ_e (meaning small deflection) are selected (Eq. (4.9)). The maximum value of θ_e found in the data after these cuts is 1.64.

- **DIS electron:**

- **Electron probability:** the EM electron finder (Section 4.2.1) provides the probabilities of the electron candidates being real electrons. The candidate with the highest probability is assumed to be the DIS electron. Its probability is required to be greater than 0.001. The distribution of the probability for left-handed electron data after all selection cuts is shown in Figure 4.8.
- **Isolated electron:** to make sure that the electron is isolated from the hadronic energy deposits, a cut on the amount of energy deposited close to the electron but not belonging to the electron,$E_{cone,had}$ (Section 4.2.1), is applied. The electron is considered as isolated if $E_{cone,had} < 5$ GeV. The distribution of $E_{cone,had}$ for left-handed electron data after all selection cuts is shown in Figure 4.8.
- **Electron track:** if the electron is detected within the CTD acceptance (0.3 rad $< \theta <$ 2.85 rad) a matching track is required. The momentum of the track has to fulfill $P^e_{track} > 3$ GeV because a very low track momentum might indicate that the track does not belong to the electron but to a low energy charged particle, since the scattered electron normally has a higher momentum. The distance of closest approach (DCA) [56, 57] between the calorimeter energy cluster belonging to the electron candidate and the CTD track extrapolation at the calorimeter entrance is required to be less than 10 cm. In this way, events are rejected that have an energy cluster belonging to a photon and a CTD track that is wrongly associated to it. The distance of the extrapolated track to the CAL module edges is required to be greater than 1.5 cm because energy measurements close to the module edges are not reliable.
- **Electron outside the CTD acceptance:** outside the CTD acceptance, no reliable tracks are measured and thus it is difficult to distinguish a photon from an electron. Therefore, the transverse momentum of the electron is required to be greater than 30 GeV in this region.

- **Photoproduction Background:** if a low energy photon from a π^0 decay in a photoproduction event is falsely misidentified as an electron in the FCAL region, y is typically high (Eq. 4.11). Therefore, an upper cut on y_e is applied:

$$y_e < 0.95. \tag{4.26}$$

The distribution of y_e for left-handed electron data after all selection cuts is shown in Figure 4.10.

- **Calorimeter:**

  - $\mathbf{E - p_z}$: a useful quantity to distinguish background and signal events is the global $E - p_z$ (Eq. 4.8). Before the interaction, the following holds for $E - p_z$:

$$\sum_{e,p} E - p_z = E_e - (-E_e) + E_p - E_p = 2E_e = 55 \text{ GeV}, \tag{4.27}$$

    where the masses of proton and electron are neglected. In a perfectly measured NC DIS event, where the detector covers the full angular region, the same value should be measured from the final state. Particles escaping through the rear beampipe change $E - p_z$ significantly because E and p_z have opposite sign and do not cancel. However, particles escaping through the forward beam pipe have very little influence on $E - p_z$. In photoproduction events, the electron is typically lost undetected in the rear beam pipe and thus $E - p_z$ is much lower than 55 GeV. In overlaid events (NC DIS events in coincidence with a background event), $E - p_z$ can have values significantly larger than 55 GeV. To reject photoproduction and overlaid events, a value of 38 GeV $< E - p_z <$ 65 GeV is required. The distribution of $E - P_z$ for left-handed electron data after all selection cuts is shown in Figure 4.9.

  - **Balance of the transverse momentum:** in an ideal NC event, the total transverse momentum p_T (Eq. 4.7) is zero. On the other hand, cosmic muons or beamgas events can show a significant p_T imbalance. Since the resolution of the p_T measurement is approximately proportional to $1/\sqrt{E_T}$ (where E_T is the total transverse energy given in Eq. 4.6), a cut on $p_T/\sqrt{E_T} < 4\sqrt{\text{GeV}}$ is done. At low E_T ($E_T < 16$ GeV), this cut is unphysical because p_T is greater than E_T. Thus, an additional cut on $p_T/E_T < 0.7$ is applied to take into account for the low-E_T region.

  - **Elastic QED Compton rejection:** in elastic QED compton events, the proton escapes undetected through the forward beam pipe, and the event contains only an electron and a photon balanced in transverse momentum. The second electron candidate found by the EM finder is assumed to be the photon. The electron and the photon make up for almost all the energy of the event. An event is rejected as QED Compton if the following requirements are fulfilled:

    * $|\phi_e - \phi_\gamma| > 3$ rad
    * $0.8 < p_T^e/p_T^\gamma < 1.2$

* $E^{tot}_{CAL} - (E^{e}_{CAL} + E^{\gamma}_{CAL}) < 3$ GeV

Here, the index e refers to the electron candidate and the index γ refers to the photon candidate.

– **Super cracks:** the edges of the BCAL next to the FCAL and RCAL are called super-cracks. In these regions the energy measurement is inaccurate due to a large amount of inactive material. Furthermore, the scenario of a particle hitting the BCAL and leaking into the FCAL or RCAL is not well simulated in the MC. Thus, events where the scattered electron hits the CAL in the region -104 cm $< z_e < -98.5$ cm or 164 cm $< z_e <$ 174 cm, where z_e is the z-position of the electron cluster, are rejected.

– **FCAL projection of γ_h:** when the hadronic final state points in the forward direction (very low values of γ_h), a fraction of it might be lost down the forward beam hole. Thus, a cut on the projection radius of γ_h on the FCAL surface is done: $R^{FCAL}_{proj} \geq 20$ cm is required. This cut corresponds to a cut on $\gamma_h > 5.1^\circ$ assuming the nominal interaction vertex position, $Z_{VTX} = 0$ cm. The distribution of γ_h for left-handed electron data after all selection cuts is shown in Figure 4.9.

- **z-vertex:** at HERA, the beams collide in a region around the nominal interaction vertex, $Z_{VTX} = 0$ cm, with a σ of 11 cm. Thus, a cut on the event vertex of $|Z_{VTX}| < 50$ cm is applied. This cut also helps to remove background events because for example beam gas events are randomly distributed in z. The Z_{VTX}-distribution for left-handed electron data after all selection cuts is shown in Figure 4.9.

- **Validity of the MC:** for very small values of y and/or large values of x, the Monte Carlo generator DJANGOH is not valid due to missing higher-order QED corrections. This region is excluded by a cut on $y_{DA}(1 - x_{DA})^2 > 0.004$, as recommended by the authors [28, 27].

4.6.2 NC+Jet Events

To reconstruct the invariant mass of the final state, the DIS electron and the hadronic jet(s) are used. Therefore, only events with at least one well reconstructed jet are accepted in this analysis. It is also possible that events have more than one jet in the final state due to QCD final state radiation.

The k_T-clustering algorithm (Section 4.2.2, [59]) reconstructs the jets and sorts them in descending order of transverse momentum p_T. The first three jets found with $p_T > 4$ GeV and pseudorapidity $|\eta| < 3$ are stored for further investigation.

If a jet points in the very forward direction, it is possible that a part of it is lost down the beam hole. Furthermore, energy from the proton remnant may contribute to the measured jet energy. Therefore, only jets that have an impact point on the FCAL face that lies outside the first inner ring of the FCAL (60×60 cm^2 around the beam hole), and that have a pseudorapidity of $|\eta| < 2.73$ are accepted in this analysis. Additionally, it is required that the leading jet (the accepted jet with the highest p_T) has a transverse momentum of $p_T > 15$ GeV. Figure 4.11 shows the distribution of the jet variables for left-handed electron data after all selection cuts were applied.

Figure 4.6 shows a typical NC DIS event with $x_{DA} = 0.17$ and $y_{DA} = 0.57$. The left plot (XY-view) shows a cross section of the inner parts of the detector perpendicular to the beam pipe, the right plot (ZR-view) shows a cross section of the inner parts of the detector parallel to the beam pipe. The scattered electron and the jet are both in the BCAL and are labelled in the plots. The energy deposits in the FCAL very close to the beam pipe originate from the proton remnant. Figure 4.7 shows the ZR-view of a NC event with high values of x and y ($x_{DA} = 0.59$, $y_{DA} = 0.48$), the kinematic region most sensitive to leptoquark signals. Both electron and jet are scattered into the FCAL.

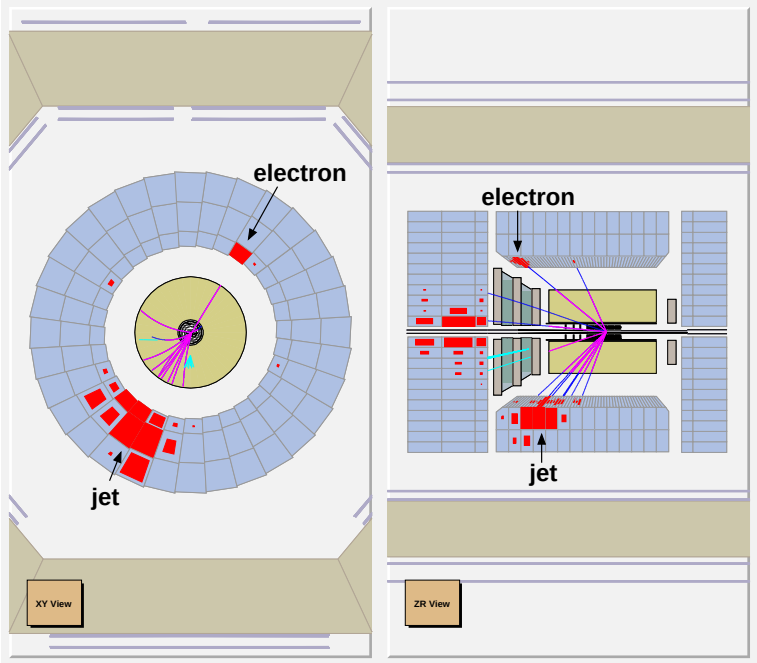

Figure 4.6: *A typical NC DIS event ($x = 0.17$, $y = 0.57$).*

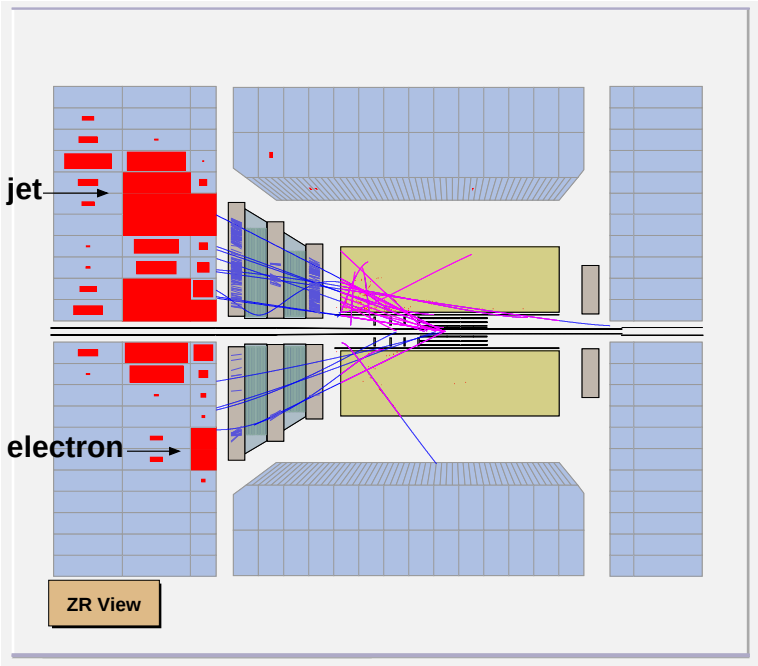

Figure 4.7: *A NC DIS event with high values of x and y ($x = 0.59$, $y = 0.48$).*

4.6.3 Control Distributions

In this Section, the control distributions for left-handed electron data after all the cuts were applied are shown. The distributions for the other three data sets (right-handed electrons and left- and right-handed positrons) look very similar and can be found in Appendix A.

Figure 4.8 shows some of the variables used by the EM finder to calculate the electron probability (Section 4.2.1), as well as the electron probability itself. Figure 4.9 shows the polar angle, the azimuthal angle and the energy of the scattered electron, the polar angle and the transverse momentum of the hadronic system, as well as the global p_T, the global $E - P_z$ and the z-vertex position. Figure 4.10 shows the distributions of the kinematic variables reconstructed using the Double Angle method and of y reconstructed using the electron method. The jet variables for the leading jet and for all jets, as well as the number of jets, are shown in Figure 4.11. Figure 4.12 shows several variables calculated from electron and jet information: the difference in azimuthal angle between the electron and the leading jet, the vectorial and the scalar sums of the transverse momenta of electron and all jets, as well as $E - P_z$ reconstructed from the electron and all jets.

The MC is normalized to the data luminosity and describes the data generally well.

The description of the $E - P_z$ distribution is not very good since the data peak is broader than the MC peak. This problem is present only in the electron data (see Appendix A). Furthermore, a shift is seen in the vectorial sum of the transverse momenta of electron and jets, whereas for the scalar sum good agreement is found. The effect, which is due to differences in the electromagnetic and the hadronic energy scale and resolution, is of the order of 1%. In the distribution of $\Phi_{tracking} - \Phi_{CAL}$ of the electron, the data peak is broader than the MC peak. This is due to the non perfect simulation of the detector resolution in the MC.

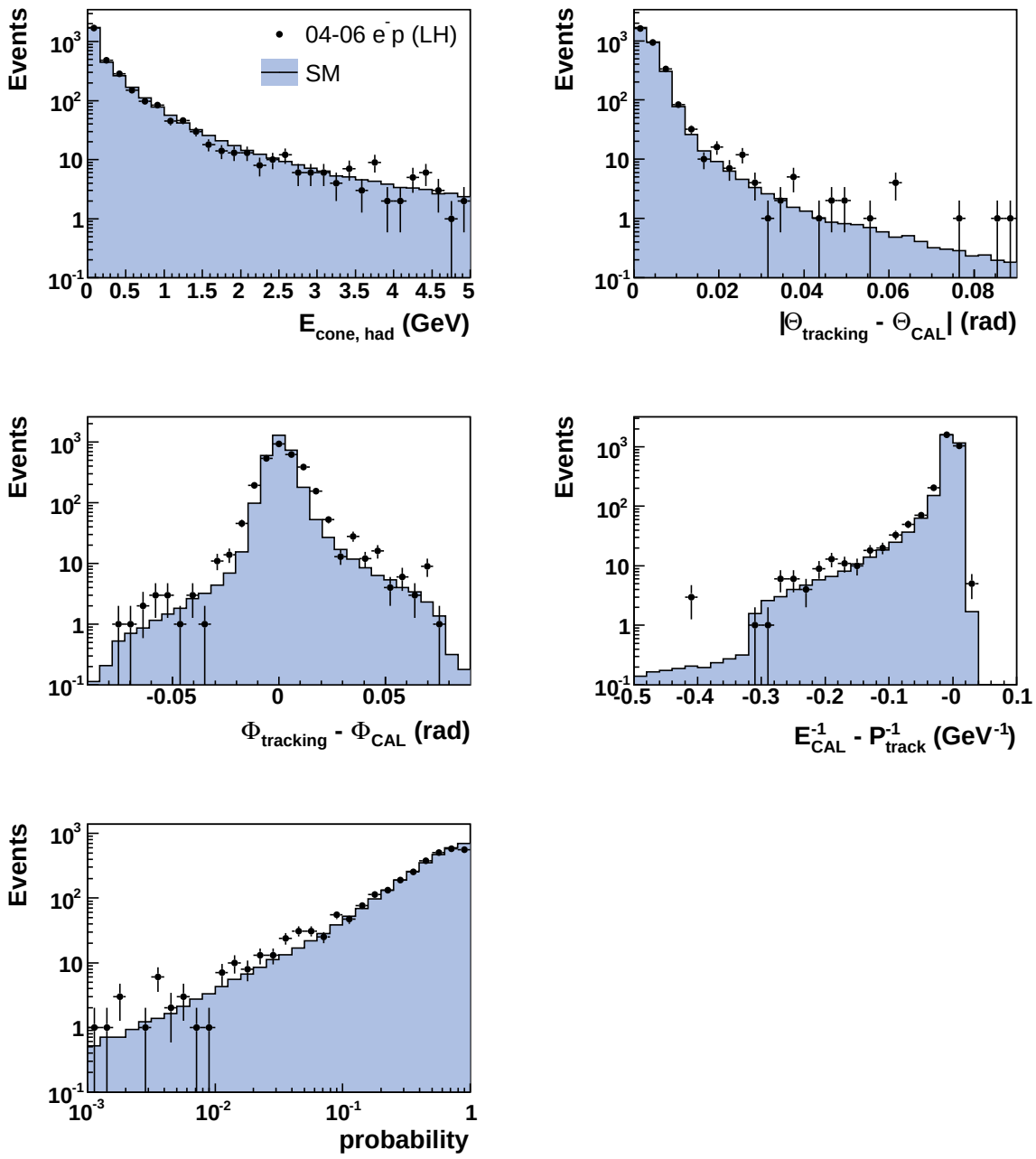

Figure 4.8: *Variables used by the EM finder for the evaluation of the electron probability, and the electron probability itself, shown for left-handed electron data after all selection cuts. The dots are the data and the histograms show the luminosity normalized Standard Model expectation.*

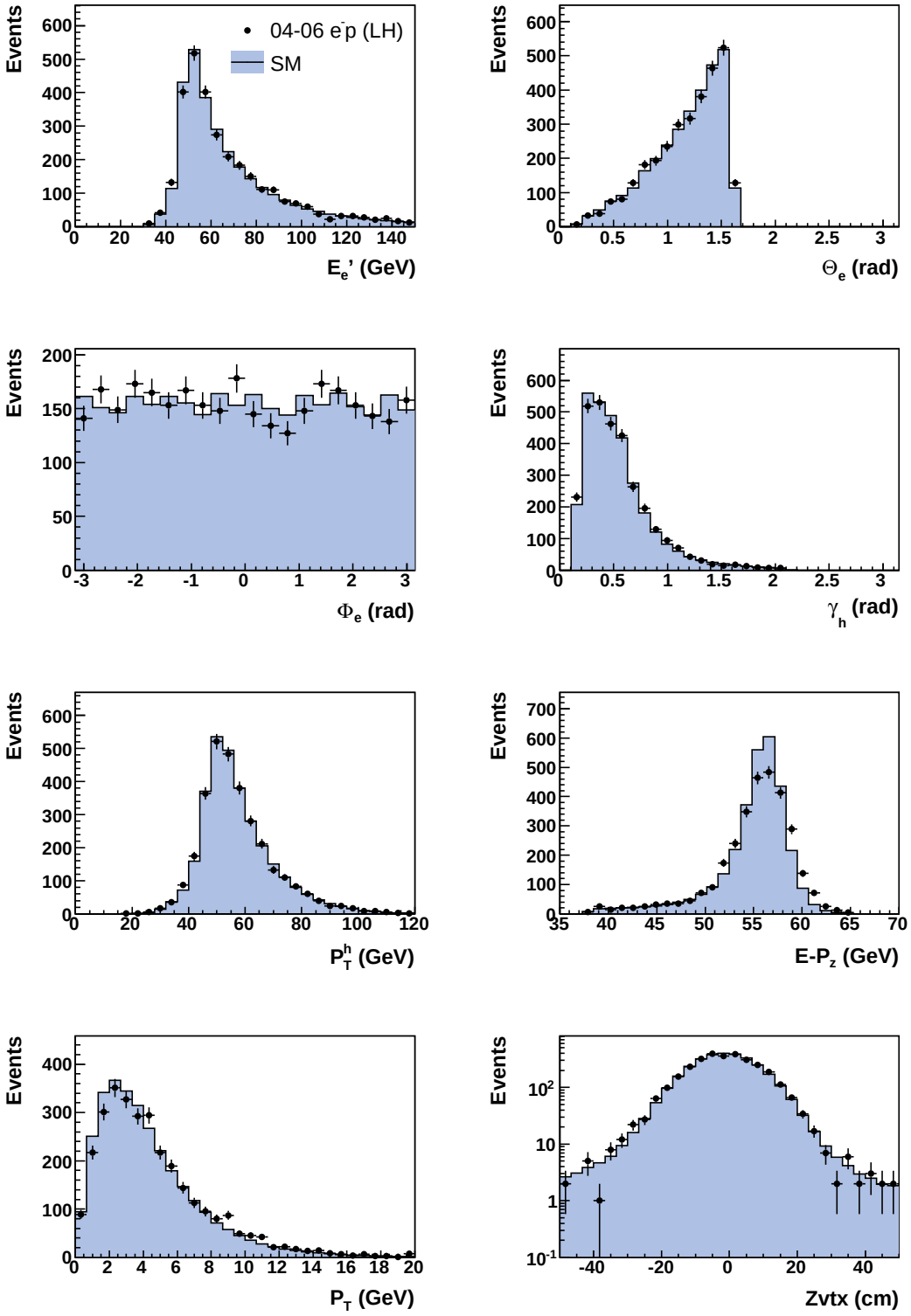

Figure 4.9: *Electron, hadronic, and global variables for left-handed electron data after all selection cuts. The dots are the data and the histograms show the luminosity normalized Standard Model expectation.*

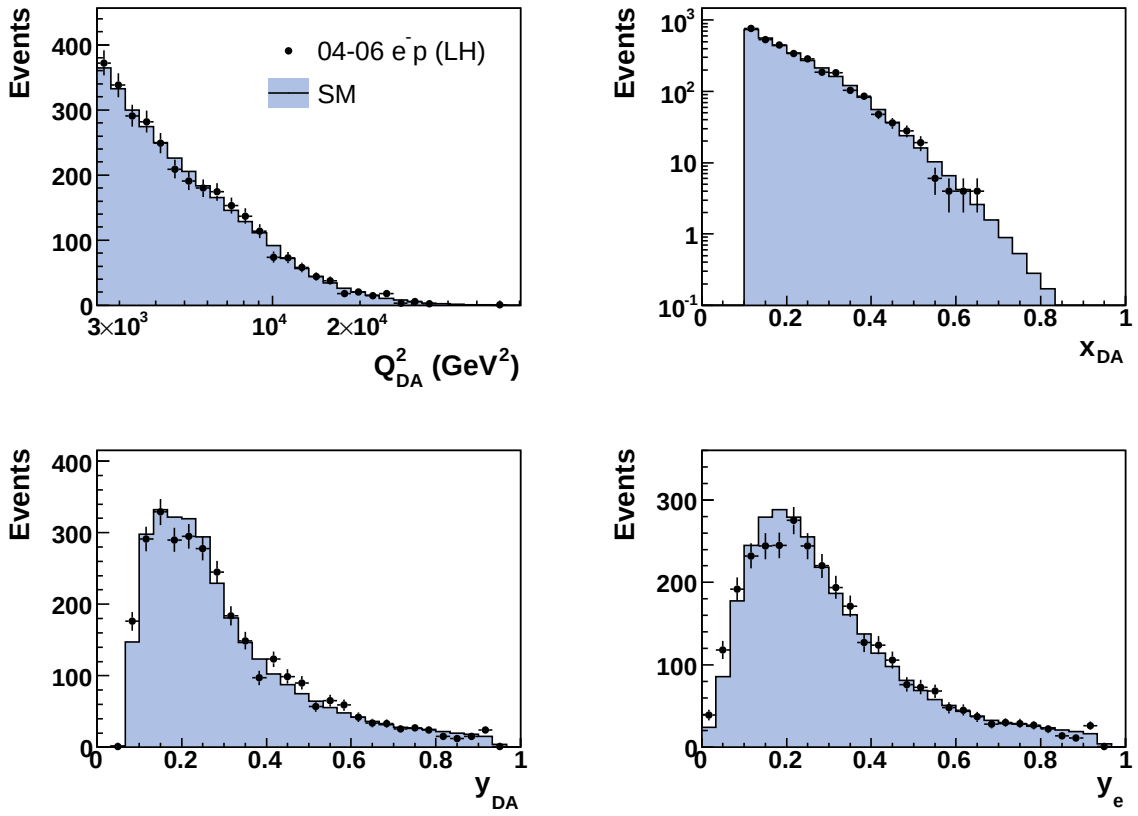

Figure 4.10: *Kinematic variables for left-handed electron data after all selection cuts. The dots are the data and the histograms show the luminosity normalized Standard Model expectation.*

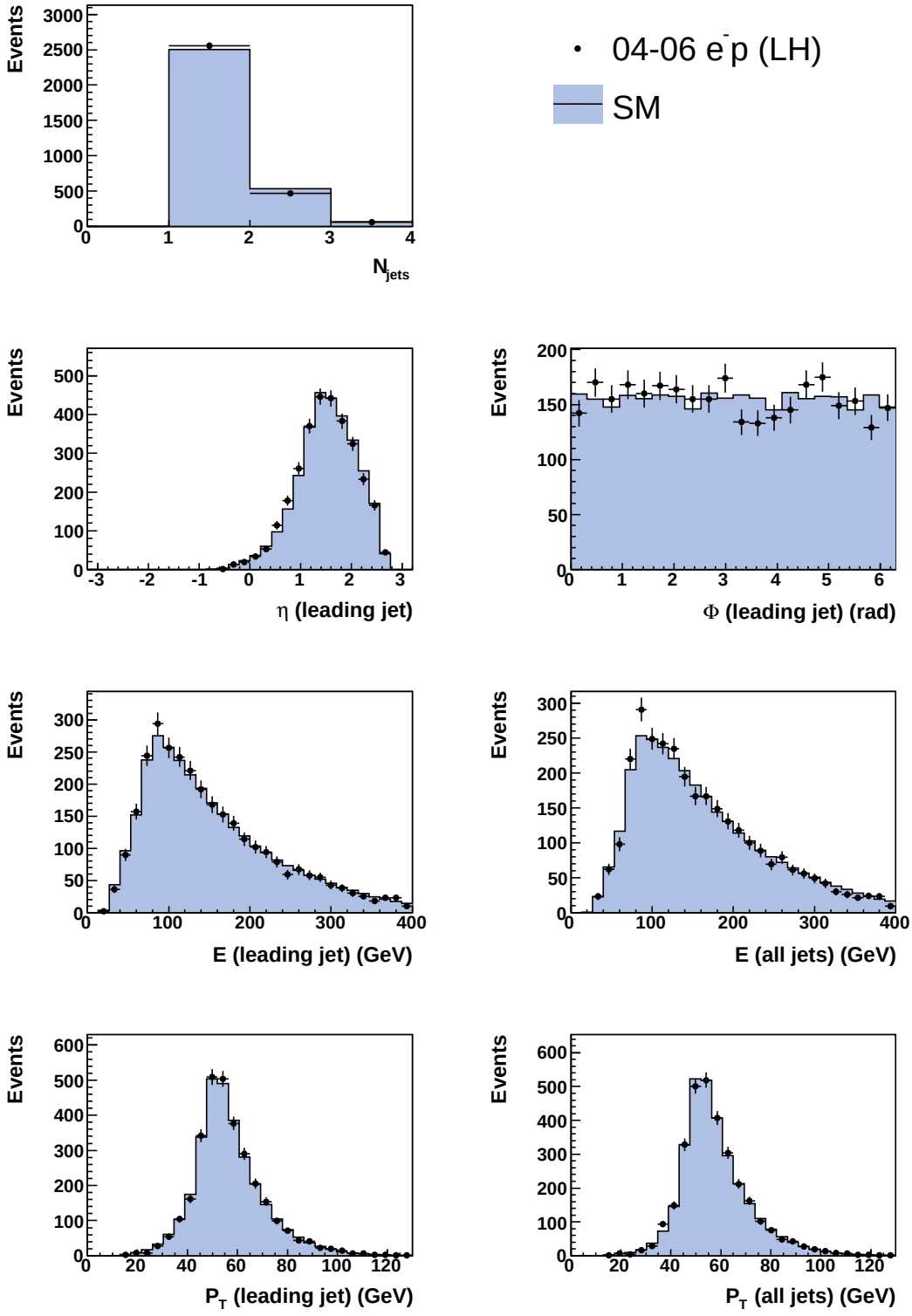

Figure 4.11: *Jet variables for left-handed electron data after all selection cuts. The dots are the data and the histograms show the luminosity normalized Standard Model expectation.*

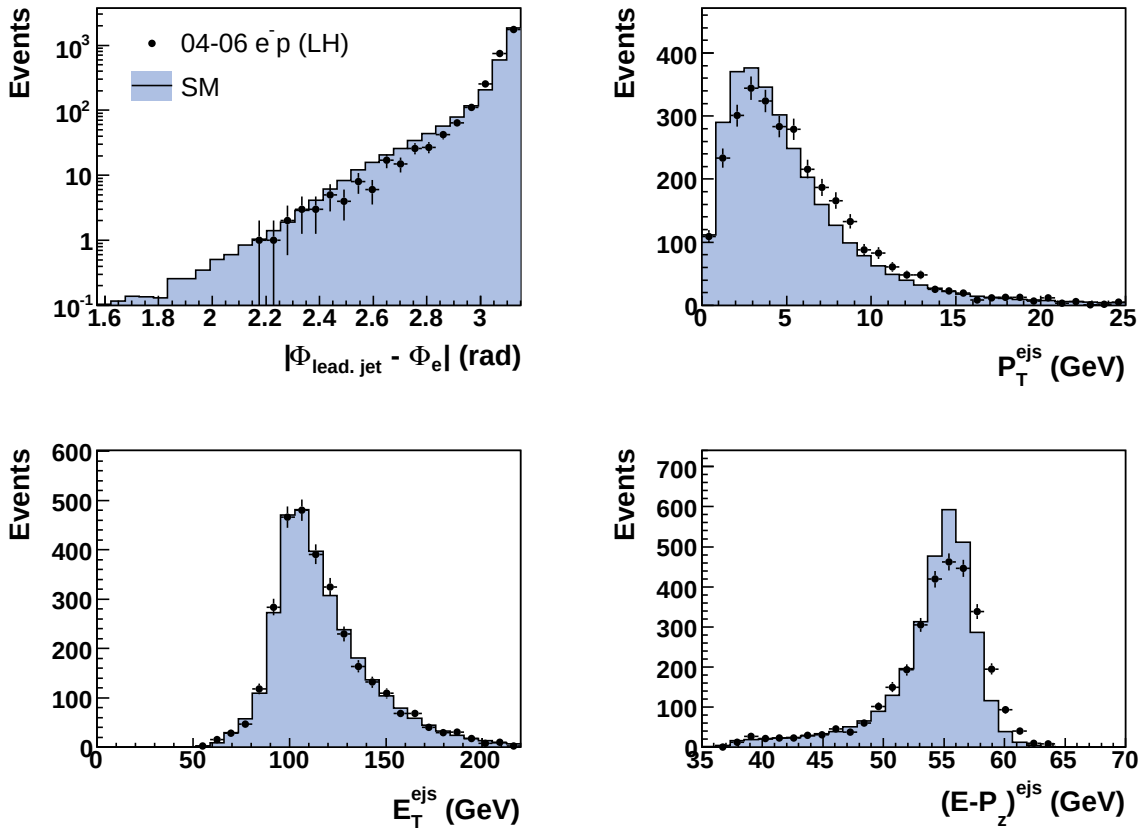

Figure 4.12: *Variables from electron and jet information for left-handed electron data after all selection cuts. The dots are the data and the histograms show the luminosity normalized Standard Model expectation.*

4.6.4 Cut Efficiencies

The effect of the event selection cuts was studied applying the following preselection on both data and MC events:

- trigger preselection (Section 4.6.1, [9, 62]);
- at least one electron candidate from the EM finder is required;
- $Q^2_{DA} > 500$ GeV;
- events are required to be in the valid phase space region of the MC generator DJANGOH: $y_{DA}(1 - x_{DA})^2 > 0.004$ (Section 4.6.1, [28, 27]);
- the z vertex coordinate is restricted to $|Z_{VTX}| < 80$ cm.

After the preselection, 1474869 data events and 266851 MC events (luminosity normalized) remain. The differences in the numbers is due to background events in the data. After all cuts were applied, 8949 data events and 9002.6 MC events were selected. Table 4.2 shows the absolute and relative efficiencies of the event selection cuts for both data and MC events. The absolute efficiency $\mathcal{E}_{abs}$ is defined as the ratio between the number of events after both the preselection and cut i in Table 4.2 was applied and the number of events after only the preselection was applied:

$$\mathcal{E}_{abs} = \frac{\#\text{pres. \& cut } i}{\#\text{pres.}} \tag{4.28}$$

The relative efficiency $\mathcal{E}^{N-1}_{rel}$ is defined as the ratio between the number of events after all N cuts were applied and the number of events after all cuts except for cut i in Table 4.2 was applied:

$$\mathcal{E}^{N-1}_{rel} = \frac{\#\text{all } N \text{ cuts}}{\#N - 1 \text{ cuts}} \tag{4.29}$$

The absolute efficiencies are usually lower for data than for MC due to background events in the data samples. This can for example be seen from the cuts on electrons in the forward region ($y_e < 0.95$ and $p^e_T > 30$ outside the CTD acceptance region): they remove almost no MC events, but more than half of the data events.

The relative efficiencies in data and MC agree well. The most important cuts are those restricting the kinematic region ($Q^2_{DA} > 2500$ GeV and $x_{DA} < 0.1$), as well as the jet cuts and the requirement of a matching track for electrons in the CTD acceptance region. The cut on the FCAL projection of γ_h is redundant when the jet cuts are applied, but since the jet cuts do not belong to the NC DIS selection, this cut is listed in the Table.

cut	$\mathcal{E}_{abs}$ (%) (data)	$\mathcal{E}_{rel}^{N-1}$(%) (data)	$\mathcal{E}_{abs}$ (%) (MC)	$\mathcal{E}_{rel}^{N-1}$(%) (MC)
Q^2_{DA}	37.09	26.29	8.28	26.21
x_{DA}	7.58	60.40	27.76	59.57
y_e	28.50	99.97	98.12	99.95
EM probability	78.57	99.83	98.75	99.93
$E_{cone,had}$	46.59	98.16	97.70	98.18
electron track	78.14	86.39	84.84	86.96
p_T^e outside CTD	39.83	99.77	99.17	99.80
$E - P_z$	85.41	96.60	97.06	96.06
$p_T/\sqrt{E_T}$, p_T/E_T	91.35	99.94	100.00	99.99
QED Compton	99.88	99.78	99.98	99.99
super cracks	99.11	99.61	96.14	99.58
FCAL γ_h proj.	99.69	100	98.55	100
z-vertex	98.84	98.64	98.42	98.70
jet cuts	23.76	94.35	74.20	93.97

Table 4.2: *Absolute and relative efficiencies of the NC event selection cuts for data (first two columns) and Monte Carlo (last two columns).*

The selection efficiency $\mathcal{E}_{sel}$ was calculated using the SM Monte Carlo. The following preselection was applied:

- events are required to be in the kinematic region of the analysis: $Q^2_{true} > 2500\ \mathrm{GeV}^2$, $x_{true} > 0.1$, $y_{true} < 0.95$, and $y_{true}(1 - x_{true})^2 > 0.004$, where Q^2_{true}, x_{true} and y_{true} are the generated values of the kinematic variables Q^2, x and y;
- trigger preselection (Section 4.6.1, [9, 62]) is applied;
- at least one electron candidate from the EM finder is required;
- the z vertex coordinate is restricted to $|Z_{VTX}| < 80$ cm.

$\mathcal{E}_{sel}$ is evaluated in bins of x and y and is defined as the fraction of events generated in a bin passing all selection cuts:

$$\mathcal{E}_{sel} = \frac{\#\text{ events generated in bin passing all cuts}}{\#\text{ events generated in bin passing preselection cuts}}. \tag{4.30}$$

For $y < 0.1 - 0.2$ the selection efficiency is lower than 70% mainly due to the jet cuts. For $0.1 - 0.2 < y < 0.5$ it is greater than 70%, while for $y > 0.5$ it is lower due

to the electron cuts. In the $x > 0.6$, $y > 0.7$ region $\mathcal{E}_{sel}$ is again greater than 70% due to the looser electron selection criteria outside the CTD acceptance region. The selection efficiencies extracted from the other MC samples are very similar and are therefore not shown.

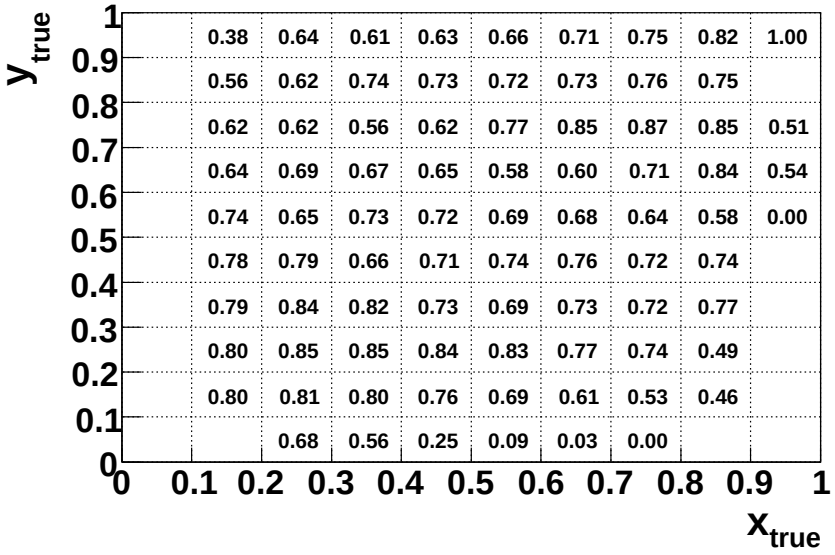

Figure 4.13: *Selection efficiency $\mathcal{E}_{sel}$ in the (x_{true}, y_{true})-plane estimated using the NC DIS MC for left-handed electron data.*

4.7 Charged Current Selection

4.7.1 CC Events

Events were selected online by using the ZEUS three-level trigger system (Section 3.2.5, [41, 49]). The trigger chains used for the selection of CC DIS events required missing transverse momentum reconstructed in the CAL, and the timing of the event and the vertex position consistent with an *ep* interaction [10, 65].

The offline event selection is optimized to select the phase-space region with the highest signal-to-background ratio for leptoquark events. Moreover, cleaning cuts are applied to remove background and badly reconstructed events from this region.

If the hadronic system points very forward, it is outside of the CTD acceptance. Thus, no selection based on tracking information can be applied. The CC events are classified according to γ_0, which is the hadronic angle assuming the nominal vertex position $Z_{vtx} = 0$. The "low-γ_0 events", for which the hadronic system points outside the CTD acceptance, have an angle of $\gamma_0 \leq 0.4$ rad. The "high-γ_0 events" have a $\gamma_0 > 0.4$ rad. Since in the latter events the hadronic system is inside the CTD acceptance, more cuts based on tracking information can be applied.

- **Kinematic Region:** the kinematic region is restricted to

$$Q^2_{JB} > 700 \text{ GeV}^2 \tag{4.31}$$

$$y_{JB} < 0.9 \tag{4.32}$$

This analysis is focusing on the high-Q^2 region because at lower Q^2 the rate of CC events is very high (Eq. 2.10) and a leptoquark signal would be hidden. Furthermore, low-mass LQs are already excluded by the D0 and CDF experiments [63, 64]. Since a higher Q^2 corresponds to a higher LQ mass (Eq. 4.23), the low-Q^2 region is not interesting in this analysis. Since the CC cross section is lower than the NC cross section (except of very high Q^2 values, see Figure 2.2), a lower Q^2 cut than in the NC analysis and no x-cut are applied.

The cut on y_{JB} is done because the Q^2 resolution is poor at high y, as can be deduced from Eq. (4.18), and it is not well reconstructed. Figure 4.14 shows $Res(Q^2)$ (Eq. 4.22) in different bins of y.

The distributions of Q^2_{JB} and y_{JB} for left-handed electron data after all selection cuts were applied are shown in Figure 4.18. The distributions for the other three data samples can be found in Appendix B.

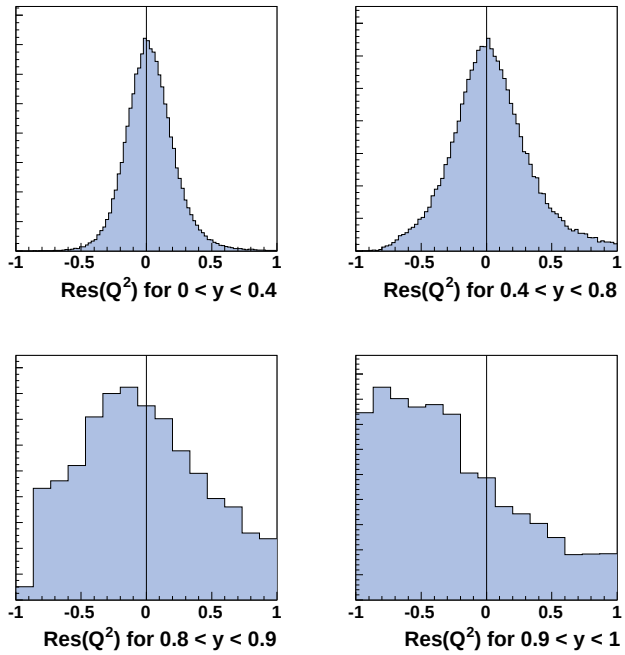

Figure 4.14: *Distribution of $Res(Q^2)$ in different bins of y for the Jacquet-Blondel reconstruction method.*

- **p_T Cuts:** since CC events are characterized by a large missing transverse momentum p_T, a cut on this quantity is applied. However, also other classes of events can show a large missing p_T. For example, beam gas events show missing p_T close to the forward beam pipe. To reject these events a cut on p_T calculated from all CAL cells excluding the first inner ring of the FCAL is applied:

$$p_T > 22 \text{ GeV} \quad (4.33)$$

$$p_T^{-1ir} > 20 \text{ GeV} \quad (4.34)$$

  Comparing to the ZEUS CC DIS analyses [66, 10], these cuts are higher because CC events with low p_T lead to low invariant masses of the LQs and are therefore not of interest in this analysis. The distributions of p_T and p_T^{-1ir} for left-handed electron data after all selection cuts were applied are shown in Figure 4.17.

- **Tracking:**
  - **Number of Tracks:** in the high-γ_0 region, cuts based on the number and quality of tracks can be applied. Tracks are selected with a transverse momentum $p_T > 0.2$ GeV. They are required to start from the MVD or the innermost

superlayer of the CTD, and have to reach at least the third superlayer of the CTD. If in addition they point to the primary vertex, they are considered as "good tracks". At least one good track is required in the event and the ratio of the total number of tracks to the number of good tracks has to fulfill the requirement

$$\frac{N_{trk} - 20}{N_{gtrk}} < 4, \tag{4.35}$$

where N_{trk} is the total number of tracks and N_{gtrk} is the number of good tracks. This cut removes beam gas events which are characterized by a high number of poor quality tracks. Figure 4.15 shows the distributions of $(N_{trk} - 20)/N_{gtrk}$, before the cut on this quantity was applied, for data and MC using a "beamgas enriched" sample of left-handed electron data. To select a sample where the contribution of beam gas events is more significant, the Q^2_{JB} cut was lowered to 150 GeV and the cuts on p_T and p_T^{-1ir} were lowered to 12 GeV. The data are well described by the MC in the region $(N_{trk} - 20)/N_{gtrk} < 4$, while for $(N_{trk} - 20)/N_{gtrk} \geq 4$ the descrption is not so good due to the presence of background events.

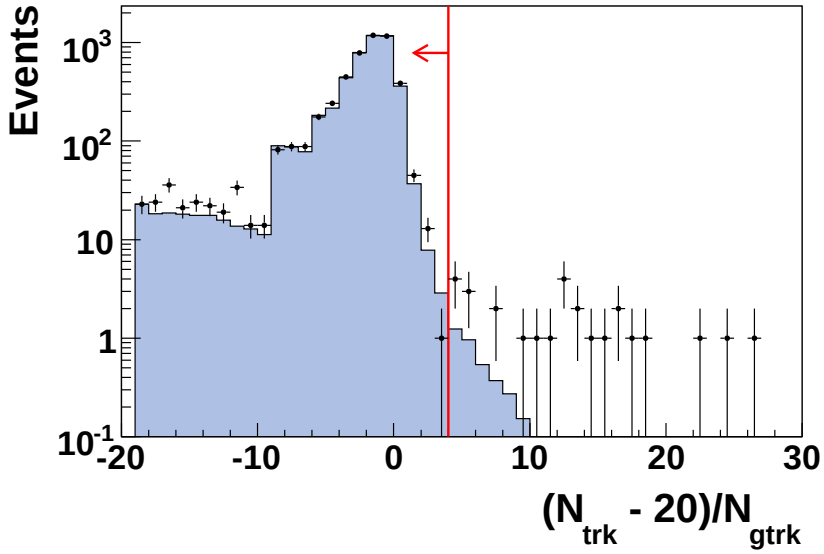

Figure 4.15: *Distibution of* $(N_{trk} - 20)/N_{gtrk}$ *for left-handed electron data and MC. All selection cuts except for the cut on* $(N_{trk} - 20)/N_{gtrk}$ *were applied, and the* Q^2 *and* p_T *cuts were lowered to include more beamgas events. The dots are the data and the histograms show the luminosity normalized Standard Model expectation.*

– **z-vertex:** as in the NC selection (section 4.6), a z-vertex cut of $|Z_{vtx}| < 50$ cm is required. Since the z-vertex is needed to calculate the jet impact position on the FCAL face, this cut is also done in the low-γ_0 region, even though the tracking information used to reconstruct the z-vertex is worse. However, the z-vertex distributions of data and MC in the low-γ_0 region are in reasonable agreement (Fig. 4.17) and thus the z-vertex reconstructed from tracking information can be used to calculate the jet position. A systematic uncertainty on the jet position of 0.5 cm is considered in the analysis but its effect is found to be negligible (section 5.2).

– **Azimuthal Angle:** for many kinds of background events (e.g. cosmic and halo muons, or beamgas events) the direction of the missing p_T calculated from tracking information differs from the p_T-direction calculated from calorimeter information. This is due to the fact that for the calculation of the p_T-direction from tracking information only tracks that point to the primary vertex are used. A cut on the difference in the azimuthal angles calculated from tracking information and from calorimeter information is applied [67]:

$$|\Phi_{tracking} - \Phi_{CAL}| < 45^\circ \quad \text{for} \quad p_T < 30 \text{ GeV} \tag{4.36}$$

$$|\Phi_{tracking} - \Phi_{CAL}| < 60^\circ \quad \text{for} \quad p_T > 30 \text{ GeV} \tag{4.37}$$

The distribution of $|\Phi_{tracking} - \Phi_{CAL}|$ for left-handed electron data after all selection cuts were applied is shown in Figure 4.17.

- **Background Rejection:**

– $\mathbf{V_{AP}/V_P}$: photoproduction events can be falsely identified as CC events if jets are misreconstructed. In this case the measured transverse momentum is less collimated than in CC events. To check this, a parallel and an antiparallel component of the vectorial transverse momentum $\vec{p_T}$ are defined:

$$V_P = \sum_i \vec{p}_{T,i} \cdot \vec{n}_{p_T} \quad \text{for} \quad \vec{p}_{T,i} \cdot \vec{n}_{p_T} > 0,$$

$$V_{AP} = -\sum_i \vec{p}_{T,i} \cdot \vec{n}_{p_T} \quad \text{for} \quad \vec{p}_{T,i} \cdot \vec{n}_{p_T} < 0, \tag{4.38}$$

where $\vec{n}_{p_T}$ is a unit vector having the direction of $\vec{p_T}$ and the sums run over all calorimeter cells with an energy deposit. The value of V_{AP} for photoproduction events is higher than for CC events. A cut of

$$V_{AP}/V_P < 0.35 \quad \text{for} \quad p_T < 30 \text{ GeV} \tag{4.39}$$

is applied [67]. The distribution of V_{AP}/V_P for left-handed electron data after all selection cuts were applied is shown in Figure 4.17.

– **Neutral Current Rejection:** if the energy of the NC DIS electron or a jet is not reconstructed properly, large missing transverse momentum can be measured. However, NC events can easily be identified by the presence of the scattered electron. Like in the NC analysis, the EM electron finding algorithm [57] is used to look for electron candidates. An event is rejected as NC DIS if all of the following requirements are fulfilled:

$$\begin{aligned} E - P_Z &> 30 \text{ GeV} \\ p_T &< 30 \text{ GeV} \\ E'_e &> 4 \text{ GeV} \\ E_{cone,had} &< 5 \text{ GeV} \\ P_e^{track}/E'_e &> 0.25 \quad \text{for} \quad 15^\circ < \theta_e < 164^\circ \\ E_T^e &> 2 \text{ GeV} \quad \text{for} \quad \theta_e \geq 164^\circ \end{aligned} \tag{4.40}$$

Here, E'_e is the energy of the highest probability electron candidate, $E_{cone,had}$ is the energy deposited close to the electron but not belonging to the electron (Section 4.2.1), P_e^{track} is the momentum of the electron track, θ_e is the polar angle of the electron, and E_T^e is the transverse energy of the electron.

The cut on $E - P_Z$ is done because $E - P_Z$ peaks at 55 GeV for NC events and is small for CC events. A value of $p_T < 30$ GeV is required because for NC events p_T is close to zero. The distributions of $E - P_Z$ and p_T for left-handed electron data after all selection cuts were applied are shown in Figure 4.17. In the acceptance region of the CTD ($15^\circ < \theta_e < 164^\circ$), an electron track can be reconstructed. The momentum of the track should ideally be the same as the measured electron energy. Thus, $P_e^{track}/E'_e > 0.25$ is required.

– **Energy Fractions in the CAL:** if a cosmic muon travels vertically through the FCAL or the RCAL, or a halo muon travels horizontally through the BCAL, most of the energy will be deposited only in the electromagnetic or the hadronic section. Furthermore, the FCAL topology of a halo muon event is different from the FCAL topology of an *ep* event: In *ep* events, most particles stop before reaching the HAC2 section, whereas halo muons typically distribute their energy uniformly. Events that fulfill one of the following conditions are rejected [10, 65]:

  - if $E_{FCAL} > 2$ GeV
    - $E_{FEMC}/E_{FCAL} < 0.1$ or
    - $E_{FEMC}/E_{FCAL} > 0.9$ or
    - $E_{FHAC1}/E_{FCAL} < 0.1$ or
    - $E_{FHAC1}/E_{FCAL} > 0.75$ or
    - $E_{FHAC2}/E_{FCAL} > 0.6$
  - if $E_{BCAL} > 2$ GeV
    - $E_{BHAC}/E_{BCAL} > 0.85$ or
    - $E_{BHAC2}/E_{BCAL} > 0.3$
  - if $E_{RCAL} > 2$ GeV
    - $E_{RHAC}/E_{RCAL} > 0.8$

  Here, for example, E_{FEMC} is the energy deposited in the electromagnetic section of the FCAL and E_{FCAL} is the total energy deposited in the FCAL. Furthermore, events which have less than 40 calorimeter cells with an energy deposit above the noise threshold are rejected because they are likely to be low activity events (cosmic muons, halo muons, etc.).

– **Spark Rejection:** sparks (electrical discharges) in a single CAL PMT can create large missing transverse momentum and thus fake CC events. Therefore, cuts on the calorimeter cell with the highest value of E_T are applied:

$$\begin{aligned} \mathbf{E_T}(\text{highest } \mathrm{E_T} \text{ cell})/\mathbf{E_T}(\text{all cells}) &< 0.7 \\ \mathbf{p_T}(\text{without highest } \mathrm{E_T} \text{ cell})/\mathbf{p_T}(\text{all cells}) &> 0.2 \end{aligned} \tag{4.41}$$

– **FCAL Shower Shape:** high energy muons can radiate a photon which causes an electromagnetic shower in the calorimeter. The shower originating from a halo muon transversing the FCAL is much narrower than the hadronic shower originating from a CC event, and a cut on the shower shape in the FCAL is applied. The event is rejected if the cluster has a width of no more than 3×3 towers, and additionally either a weighted transverse energy (Eq. 4.42) of less than 10 GeV or an energy in the corresponding RCAL cluster greater than 0.2 GeV. The energy is weighted according to the distance of the cell energy deposits in the cluster from the highest E_T cell:

$$\begin{aligned} E'_T &= \sum_{R_{HV}<10} E_{T,HV} R_{HV}, \quad \text{with} \\ R_{HV} &= \sqrt{(H-H_0)^2 + (V-V_0)^2}. \end{aligned} \tag{4.42}$$

$H - H_0$ and $V - V_0$ are the horizontal and vertical distances of FCAL cells (in units of towers) from the highest E_T cell.

- **Timing Cuts:** halo muons pass through the RCAL before the FCAL, and cosmic muons pass the upper half of the BCAL before the lower half. Thus, these events can be distinguished from *ep* interactions using timing information (Appendix C). These cuts are not applied for the MC because the CAL timing is not well simulated. The effect of these cuts in the data is shown in Table 4.3.
- **Additional Halo Muon Cuts:** to identify events with halo muons in the BCAL, the halo muon finder TSUBAME is used [68]. Furthermore, a cut of $p_T/E_T < 0.98$ is done for $p_T < 40$ GeV to remove halo and cosmic muon events overlaid with CC events.
- **Eye scan:** for the 06/07 positron data, events were rejected according to eye scan from other CC analyses. Five events that passed all other cuts were rejected because they were identified as background in this way.

4.7.2 CC+Jet Events

As in the NC case, only events with at least one jet passing all cuts are accepted because the jets are used to reconstruct the invariant mass of the final state. The jet selection is almost the same as for NC (Section 4.6.2): only jets with $|\eta| < 2.73$, whose impact point on the FCAL face lies outside the first inner ring of the FCAL (60×60 cm^2 around the beam hole) and having a transverse momentum $p_T > 4$ GeV are accepted. For the leading jet, $p_T > 10$ GeV is required. Figure 4.19 shows the distribution of the jet variables for left-handed electron data after all selection cuts were applied.

Figure 4.16 shows the CC event reconstructed with the highest x and very high y ($x_{JB} = 0.98$, $y_{JB} = 0.87$). The left plot (XY-view) shows a cross section of the inner parts of the detector perpendicular to the beam pipe, the right plot (ZR-view) shows a cross section of the inner parts of the detector parallel to the beam pipe. The jet is reconstructed in the BCAL, the energy deposits visible in the FCAL very close to the beam pipe originate from the proton remnant.

4.7.3 Control Distributions

In this section, the control distributions for left-handed electron data after all the cuts were applied are shown. The distributions for the other three data sets (right-handed

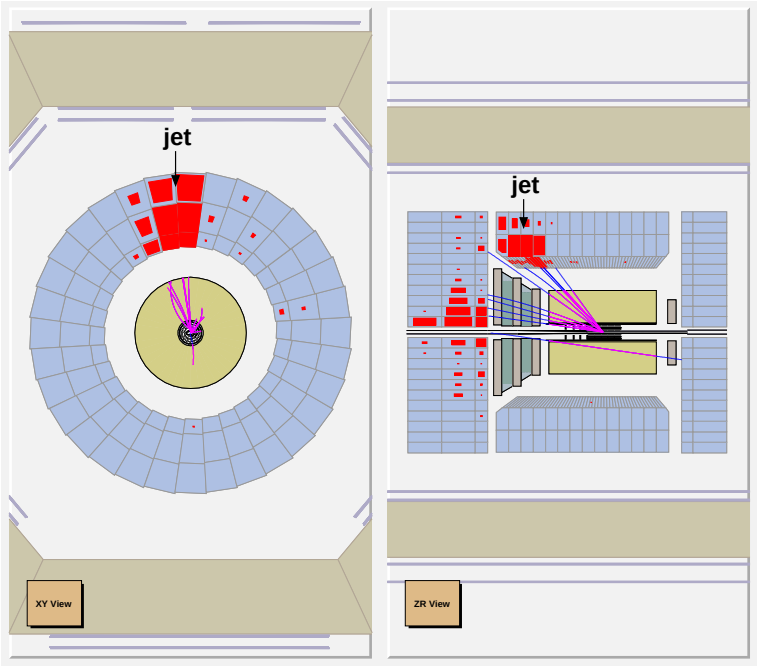

Figure 4.16: *The highest-x CC DIS event (x=0.98, y=0.87).*

electrons and left- and right-handed positrons) look very similar and can be found in Appendix B.

Figure 4.17 shows the missing transverse momentum p_T, the missing transverse momentum excluding the first inner FCAL ring p_T^{-1ir}, the global $E - P_z$, V_{AP}/V_P (Eq. 4.38), $|\Phi_{tracking} - \Phi_{CAL}|$ as well as the hadronic angle γ_0 and the z-vertex position separately for events with low γ_0 and high γ_0. Figure 4.18 shows the distributions of the kinematic variables reconstructed using the Jacquet-Blondel method. The jet variables for the leading jet and for all jets, as well as the number of jets, are shown in Figure 4.19. The data are reasonably well described by the MC.

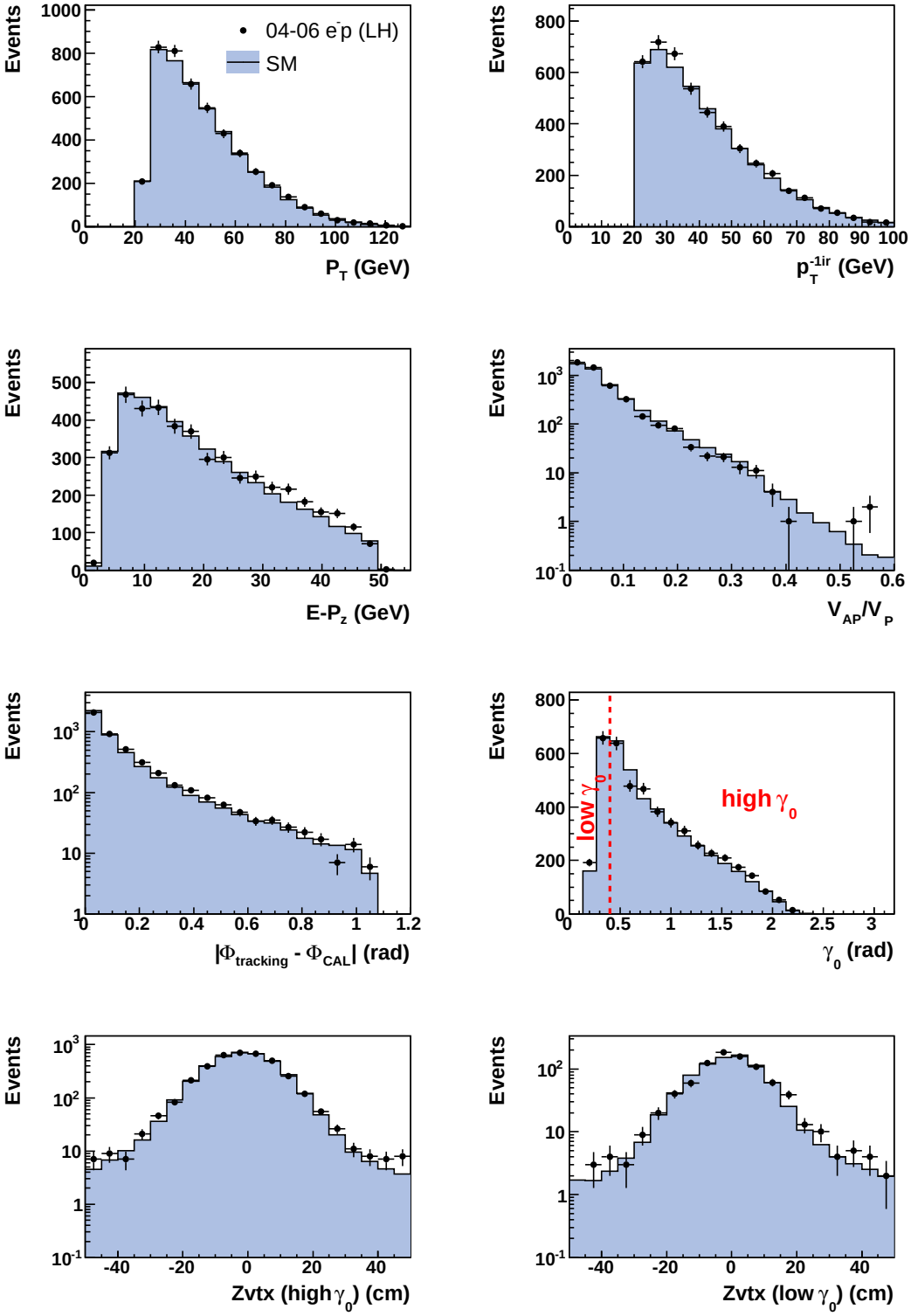

Figure 4.17: *Global variables for left-handed electron data after all selection cuts. The dots are the data and the histograms show the luminosity normalized Standard Model expectation.*

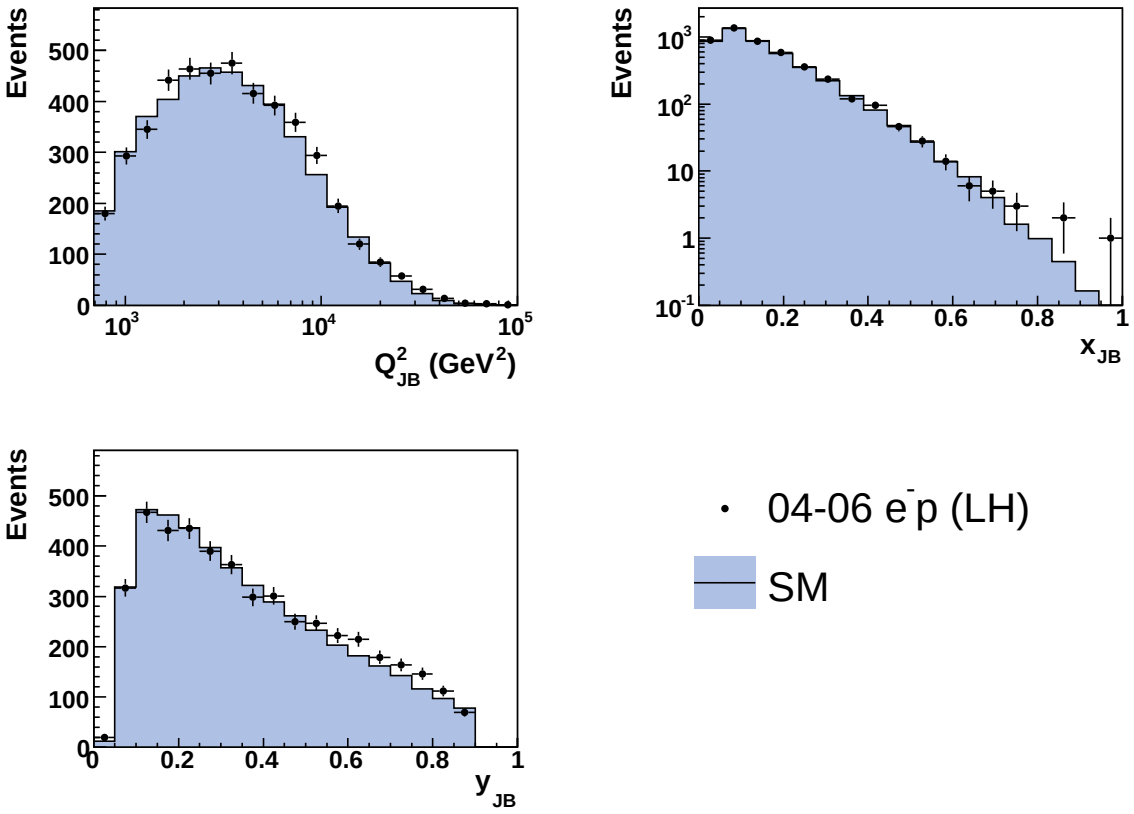

Figure 4.18: *Kinematic variables for left-handed electron data after all selection cuts. The dots are the data and the histograms show the luminosity normalized Standard Model expectation.*

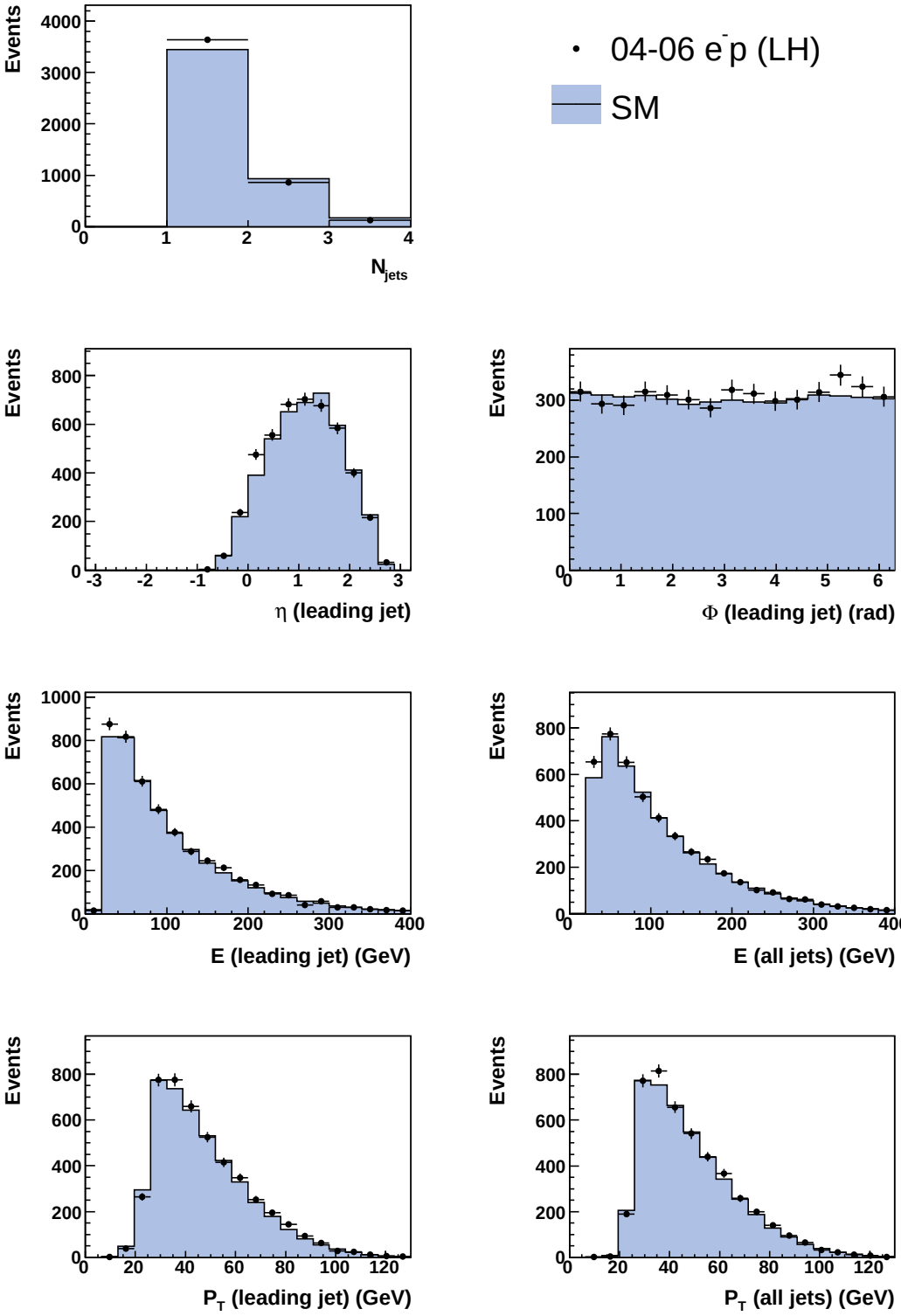

Figure 4.19: *Jet variables for left-handed electron data after all selection cuts. The dots are the data and the histograms show the luminosity normalized Standard Model expectation.*

4.7.4 Cut Efficiencies

The effect of the event selection cuts was studied applying the trigger preselection (Section 4.7, [10, 65]) and a cut on $Q^2_{JB} > 200$ GeV on both data and MC events. After the preselection, 2893314 data events and 17097.14 MC events (luminosity normalized) remained. The differences in the numbers is due to background events in the data. After all cuts were applied, 9017 data events and 9037.94 MC events were selected. Table 4.3 shows the absolute and relative efficiencies (Eq. 4.28 and 4.29) of the event selection cuts for both data and MC events.

cut	$\mathcal{E}_{abs}$ (%) (data)	$\mathcal{E}^{N-1}_{rel}$(%) (data)	$\mathcal{E}_{abs}$ (%) (MC)	$\mathcal{E}^{N-1}_{rel}$(%) (MC)
Q^2_{JB}	21.18	97.97	75.33	98.18
y_{JB}	98.82	98.37	97.32	98.45
p_T	21.78	99.83	72.11	99.89
p_T^{-1ir}	21.02	95.95	64.47	95.96
$N_{trk},\ N_{gtrk}$	27.84	95.17	97.78	95.96
z-vertex	33.94	97.09	95.54	97.80
$\Delta\Phi(\text{tracking}, \text{CAL})$	71.70	94.41	94.45	96.69
V_{AP}/V_P	53.61	99.57	95.51	99.70
NC rejection	99.82	99.62	98.12	99.40
energy fractions	53.76	95.74	96.01	96.45
spark rejection	84.64	99.68	99.67	99.95
FCAL shower shape	74.55	99.50	99.05	99.62
timing	75.22	98.94	–	–
halo muons	66.57	99.56	98.95	99.49
jet cuts	64.08	98.55	91.75	98.63

Table 4.3: *Absolute and relative efficiencies of the CC event selection cuts for data (first two columns) and Monte Carlo (last two columns).*

From the absolute efficiency, it can clearly be seen that the data sample contains background. The relative efficiencies in data and MC agree well. The biggest difference is seen in the cut on $|\Phi_{tracking} - \Phi_{CAL}|$, where the efficiency for data is lower by more than two percent. This means that this cut rejects background events that are not rejected by any other cut.

Figure 4.20 shows the selection efficiency $\mathcal{E}_{sel}$ (Eq. 4.30) obtained using the MC

simulation of the LH electron sample[4] in the (x_{true}, y_{true})-plane, where x_{true} and y_{true} are the generated values of the kinematic variables x and y. $\mathcal{E}_{sel}$ is determined using all events that fulfill $Q^2_{true} > 700\text{GeV}^2$ and $y_{true} < 0.9$ and that pass the trigger preselection (Section 4.7, [10, 65]). The efficiency is found to be about 90%. In the high-y region it is lower due to the cut on y_{JB}, and in the low-y region it is lower mainly due to the jet cuts. The efficiency in the low-x region is decreased mainly by the Q^2 and p_T cuts. The selection efficiencies extracted from the other MC samples are very similar and are therefore not shown.

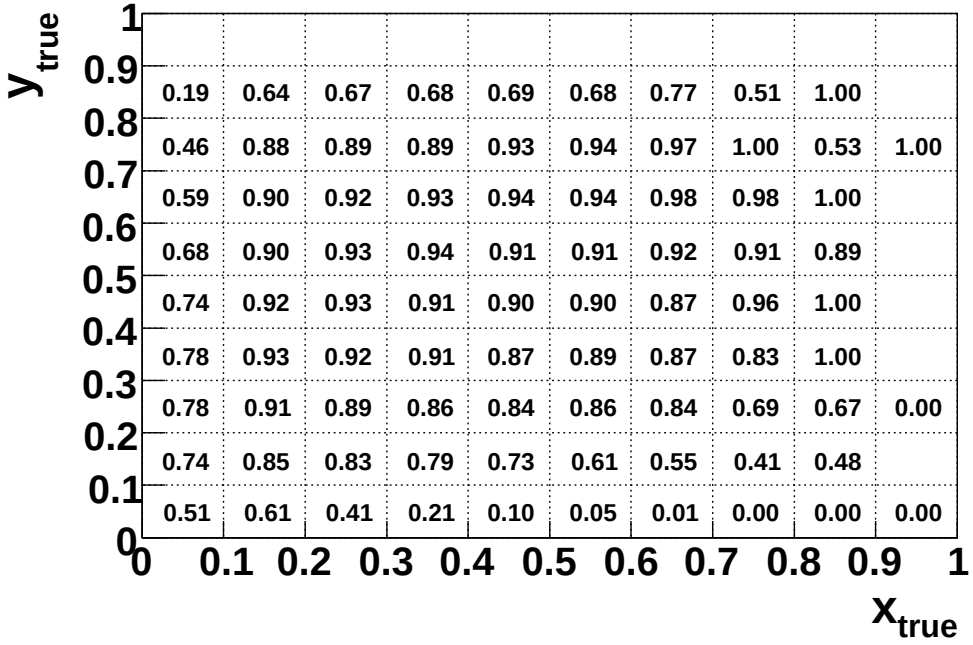

Figure 4.20: *Selection efficiency $\mathcal{E}_{sel}$ in the (x_{true}, y_{true})-plane estimated using the CC DIS MC for left-handed electrons.*

[4]The CC DIS MC is also used as the signal MC in the limit setting procedure (reweighted using theoretical cross sections).

4.7.5 Reconstruction of the Neutrino Kinematics

Since the neutrino leaves the detector undetected, its kinematic variables are reconstructed using the hadronic final state. The energy and the scattering angle (in the laboratory frame) can be calculated using the missing p_T (Eq. 4.7) and $E - P_z$ (Eq. 4.8) as

$$E_\nu = \frac{p_T^2 + \delta_\nu^2}{2\delta_\nu}\,, \tag{4.43}$$

$$\cos\theta_\nu = \frac{p_T^2 - \delta_\nu^2}{p_T^2 + \delta_\nu^2}\,, \tag{4.44}$$

where $\delta_\nu = 2E_e - (E - P_z)$ (with E_e denoting the electron beam energy). Figure 4.21 shows the control distributions of these two variables for left-handed electron data. The distributions for the other three data sets (right-handed electrons and left- and right-handed positrons) look very similar and can be found in Appendix B. The data are well described by the MC.

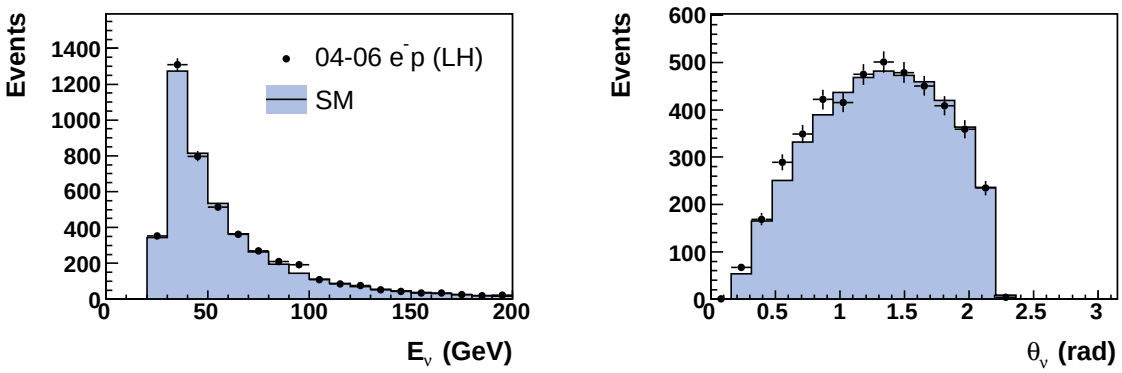

Figure 4.21: *Neutrino variables for left-handed electron data after all selection cuts. The dots are the data and the histograms show the luminosity normalized Standard Model expectation.*

4.8 Invariant Mass Reconstruction Methods

The production of leptoquark resonances decaying to a lepton and a quark would lead to a topology identical to NC or CC DIS events: an electron in case of decay to eq or missing transverse momentum in case of decay to νq and at least one jet. However, leptoquark resonances would lead to a peak in the eq or νq invariant mass spectrum. Furthermore, the y distribution and thus the lepton scattering angle is different for SM and LQ events (section 2.4.2). Hence, the invariant mass and the lepton scattering angle are crucial for distinguishing signal and background.

Three methods were considered to reconstruct the invariant mass:

- M_{lj} method: the invariant mass is calculated from the final state lepton and the jet with the highest p_T that fulfills the cuts in Section 4.6.2 and Section 4.7.2 for NC-like and CC-like event topologies, respectively;

- M_{ljs} method: the invariant mass is calculated from the final state lepton and all jets that fulfill the cuts in Section 4.6.2 and Section 4.7.2 for NC-like and CC-like event topologies, respectively;

- M_{DA}/M_{JB} method: the invariant mass is reconstructed using $M = \sqrt{xs}$, where x is an estimate of the Bjorken variable, x. In the NC case x_{DA} (Eq. 4.14) is used and in the CC case x_{JB} (Eq. 4.19) is used.

For events with QCD final state radiation, the M_{lj} method gives a biased result because the radiated gluon is not taken into account. This problem is cured if all jets in the final state are used to calculate the invariant mass, as it is done in the M_{ljs} method. This method however would also include jets from QCD initial state radiation.

In case of NC DIS, the M_{DA} method can be used to calculate the invariant mass. However, this method is sensitive to QED initial state radiation, since x_{DA} is proportional to the energy of the incoming electron, which is lower if the electron radiates a photon. Thus, this method underestimates the mass for events with QED initial state radiation.

In case of CC DIS, the M_{JB} method was investigated. However, x_{JB} is strongly affected by energy deposits from the proton remnant close to the beam pipe, leading to a significant bias of the invariant mass.

The three different mass reconstruction methods were compared using MC simulations of scalar leptoquark production (Section 2.5) in e^-q collisions with LQs decaying either to eq for the NC-like topology or to νq for the CC-like topology. Different MC samples were used assuming masses from 130 to 290 GeV. Figure 4.22 and Figure 4.23 show the

mass distributions for the three different reconstruction methods for a NC-like topology and for a CC-like topology, respectively, assuming a LQ mass of 200 GeV. The average

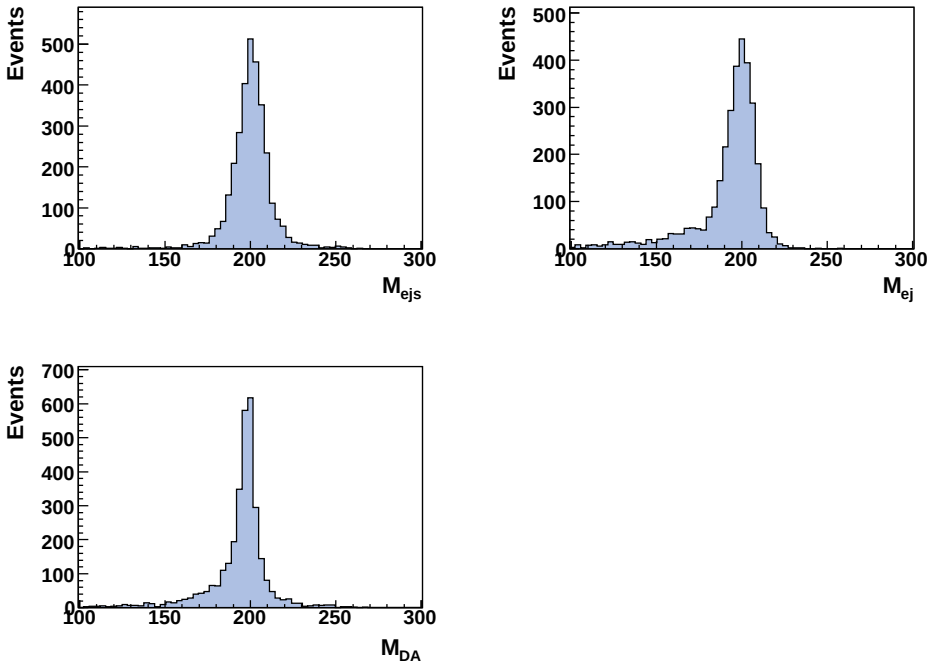

Figure 4.22: *Mass distributions for the different reconstruction methods for the NC-like topology.*

value of the reconstructed mass and the standard deviation were read from a Gaussian fit for each reconstruction method and each MC sample. This check is only done for electron samples, since the results for positron samples are expected to be very similar. Figure 4.24 shows the results of this check. The left side is for a NC-like topology, and the right side for a CC-like topology. The upper plots show the reconstructed mass relative to the true mass M_{true} as a function of M_{true}, the lower plots show the resolution as a function of M_{true}.

NC-like topology: The M_{ej} and the M_{DA} method underestimate the invariant mass, whereas the mass reconstructed using the M_{ejs} method lies within 0.5 % of the true mass. However, the M_{DA} method gives the best resolution, whereas the values for the two methods using jets are slightly worse. Since the M_{ejs} method has the least bias and the resolution is within the desired precision, this method is used in this analysis.

CC-like topology: The $M_{\nu j}$ and the M_{JB} method significantly underestimate the invariant mass, whereas the $M_{\nu js}$ slightly overestimates the mass, but it lies, except for

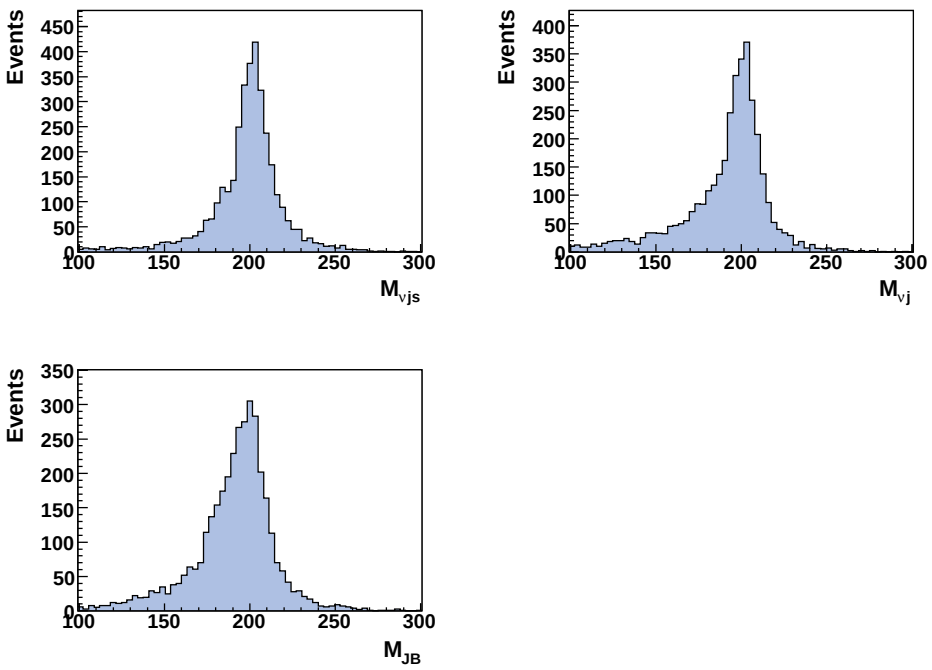

Figure 4.23: *Mass distributions for the different reconstruction methods for the CC-like topology.*

the lowest mass value that is not relevant for the limit setting (Section 6.1.1), within 1% of M_{true}. The $M_{\nu js}$ method also has the best resolution and thus is used in this analysis.

Another variable used in this analysis to distinguish between background and a possible leptoquark signal and also between scalar and vector leptoquarks is $\cos\theta^*$, the lepton scattering angle in the lepton-quark center-of-mass system. SM background, scalar and vector leptoquarks are characterized by a different $\cos\theta^*$ distribution (section 2.4.2). As for the masses, three different methods exist to reconstruct $\cos\theta^*$: it can be reconstructed in the rest frame of the lepton and the leading jet, in the rest frame of the lepton and all jets in the final state, or using the relation $\cos\theta^* = 1 - 2y$ (Eq. 2.2), where y is evaluated as y_{DA} in the NC case and as y_{JB} in the CC case. According to the choice of the mass reconstruction method, $\cos\theta^*$ is reconstructed in the rest frame of the lepton and all jets.

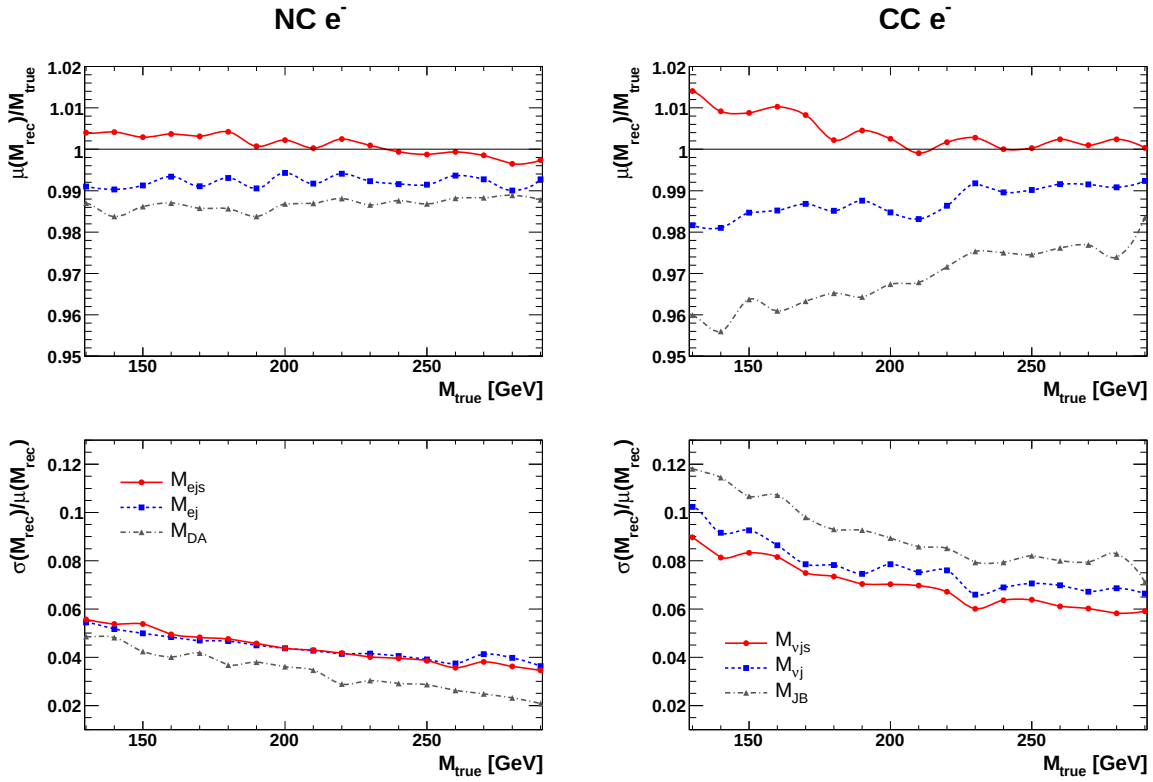

Figure 4.24: *Mean value (upper row) and resolution (lower row) as a function of the true mass for different mass reconstruction methods. The left plots are for NC-like electron events, the right plots are for CC-like electron events.*

Chapter 5

Results of the Resonance Search

5.1 Mass Distributions

In this chapter, the results of the leptoquark resonance search are presented. Figures 5.1 and 5.2 show the distributions of the invariant mass reconstructed from the electron and all jets (M_{ejs}) for NC electron and positron data, respectively, whereas Figures 5.3 and 5.4 show the invariant mass reconstructed from the neutrino and all jets ($M_{\nu js}$) for CC electron and positron data, respectively. Also shown are the mass spectra with a cut on $\cos\theta^* < 0.4$, which are more sensitive to a possible leptoquark signal. This cut is not used in the analysis since it reduces significantly the statistics. Additionally, the ratios of the observed spectra to the SM expectations without the $\cos\theta^*$ cut are presented. The data are well described by the MC and no resonances or other deviations from the Standard Model are visible.

Figures 5.5 and 5.6 show the distributions of $\cos\theta^*$ reconstructed in the rest frame of the lepton and all jets for the different NC and CC data samples, respectively. Again, no deviations from the Standard Model are visible.

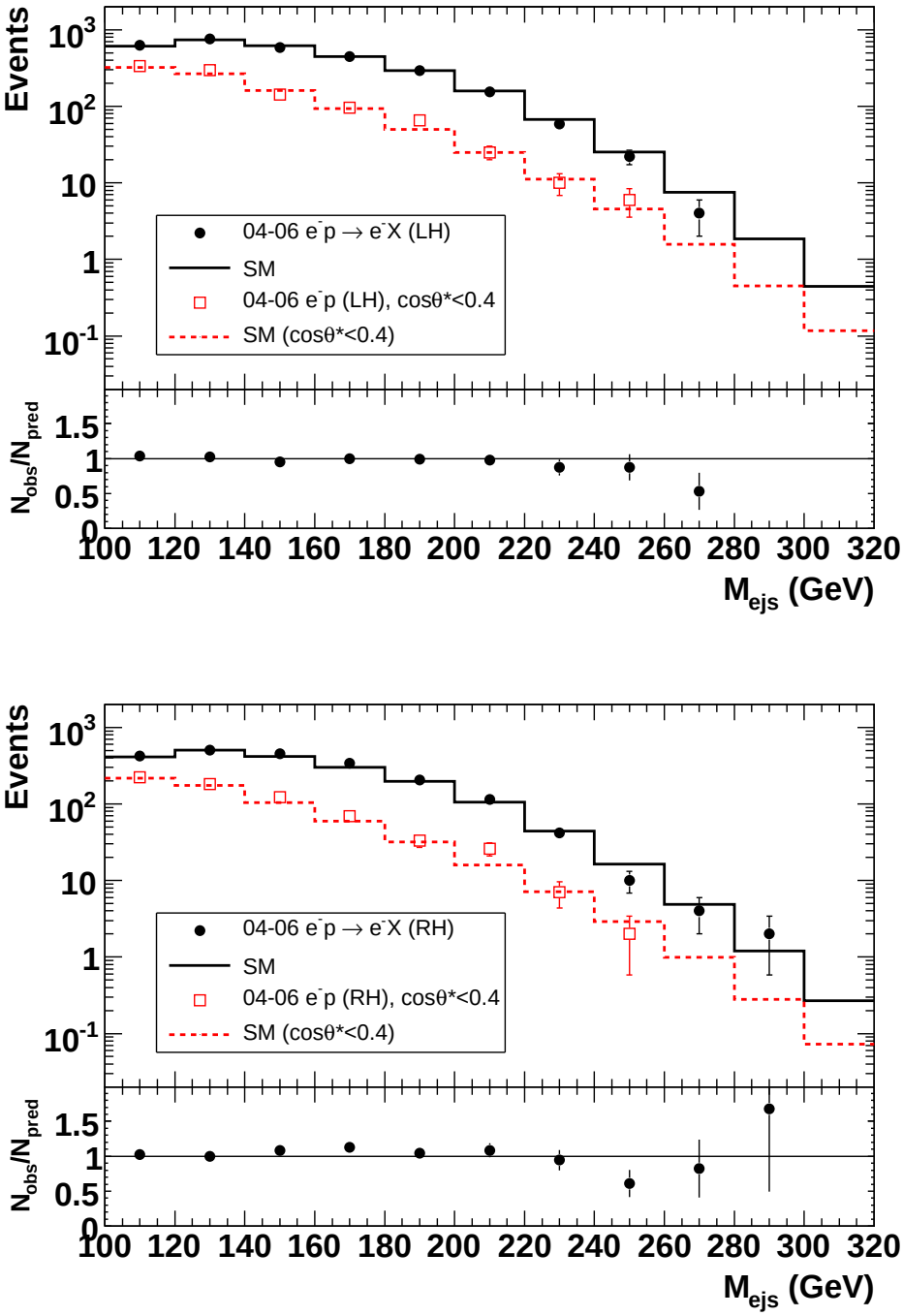

Figure 5.1: *Distributions of the invariant mass reconstructed from the electron and all jets for NC electron data (upper plot for left-handed electron data and lower plot for right-handed electron data). Shown are the mass spectra without the cut on* $\cos\theta^*$ *(full dots) and with the cut on* $\cos\theta^* < 0.4$ *(open squares). The lower halves of the plots show the ratio of the observed spectrum to the luminosity normalized SM expectation without the cut on* $\cos\theta^*$.

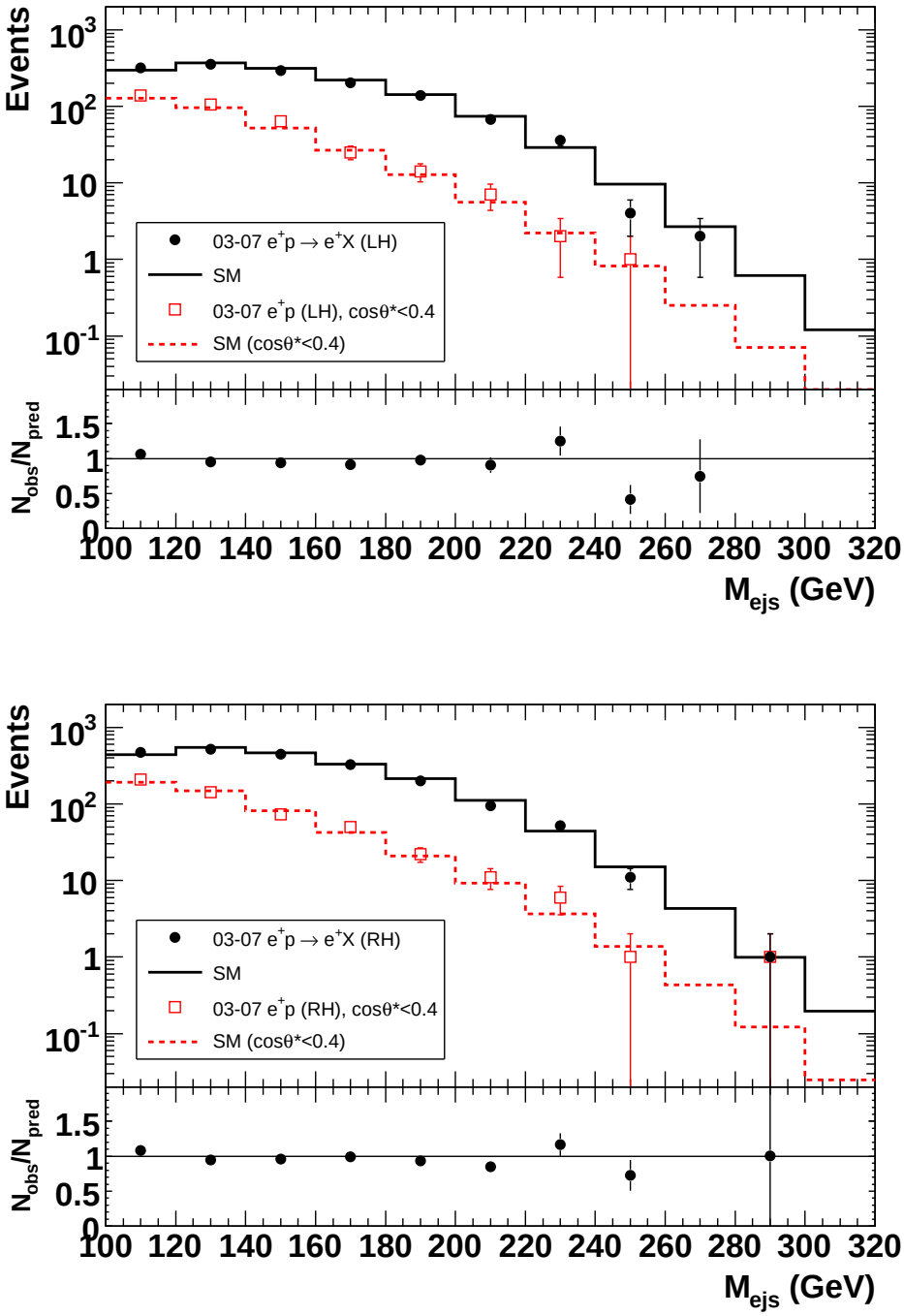

Figure 5.2: *Distributions of the invariant mass reconstructed from the electron and all jets for NC positron data (upper plot for left-handed positron data and lower plot for right-handed positron data). Shown are the mass spectra without the cut on* $\cos\theta^*$ *(full dots) and with the cut on* $\cos\theta^* < 0.4$ *(open squares). The lower halves of the plots show the ratio of the observed spectrum to the luminosity normalized SM expectation without the cut on* $\cos\theta^*$.

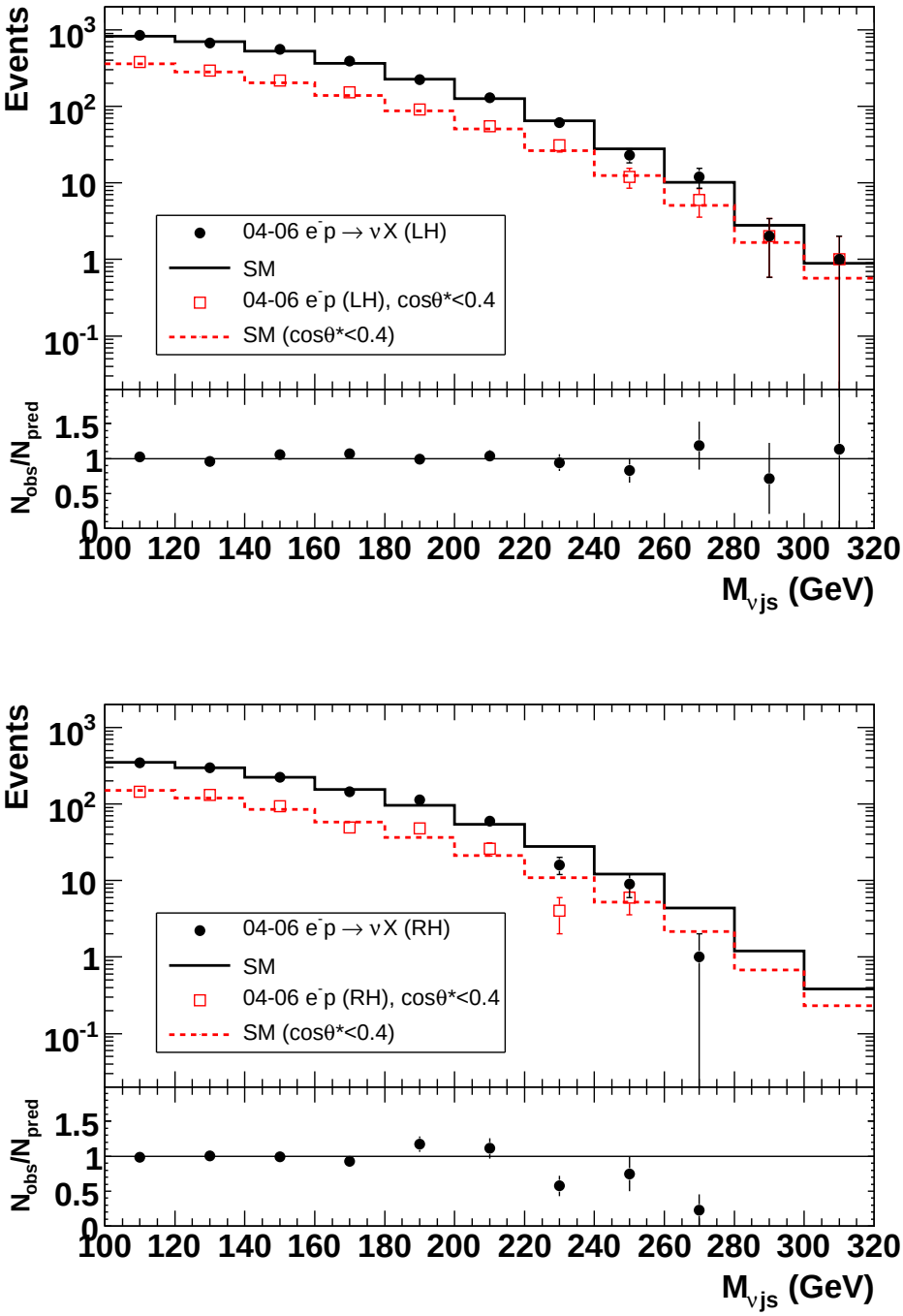

Figure 5.3: *Distributions of the invariant mass reconstructed from the neutrino and all jets for CC electron data (upper plot for left-handed electron data and lower plot for right-handed electron data). Shown are the mass spectra without the cut on* $\cos\theta^*$ *(full dots) and with the cut on* $\cos\theta^* < 0.4$ *(open squares). The lower halves of the plots show the ratio of the observed spectrum to the luminosity normalized SM expectation without the cut on* $\cos\theta^*$.

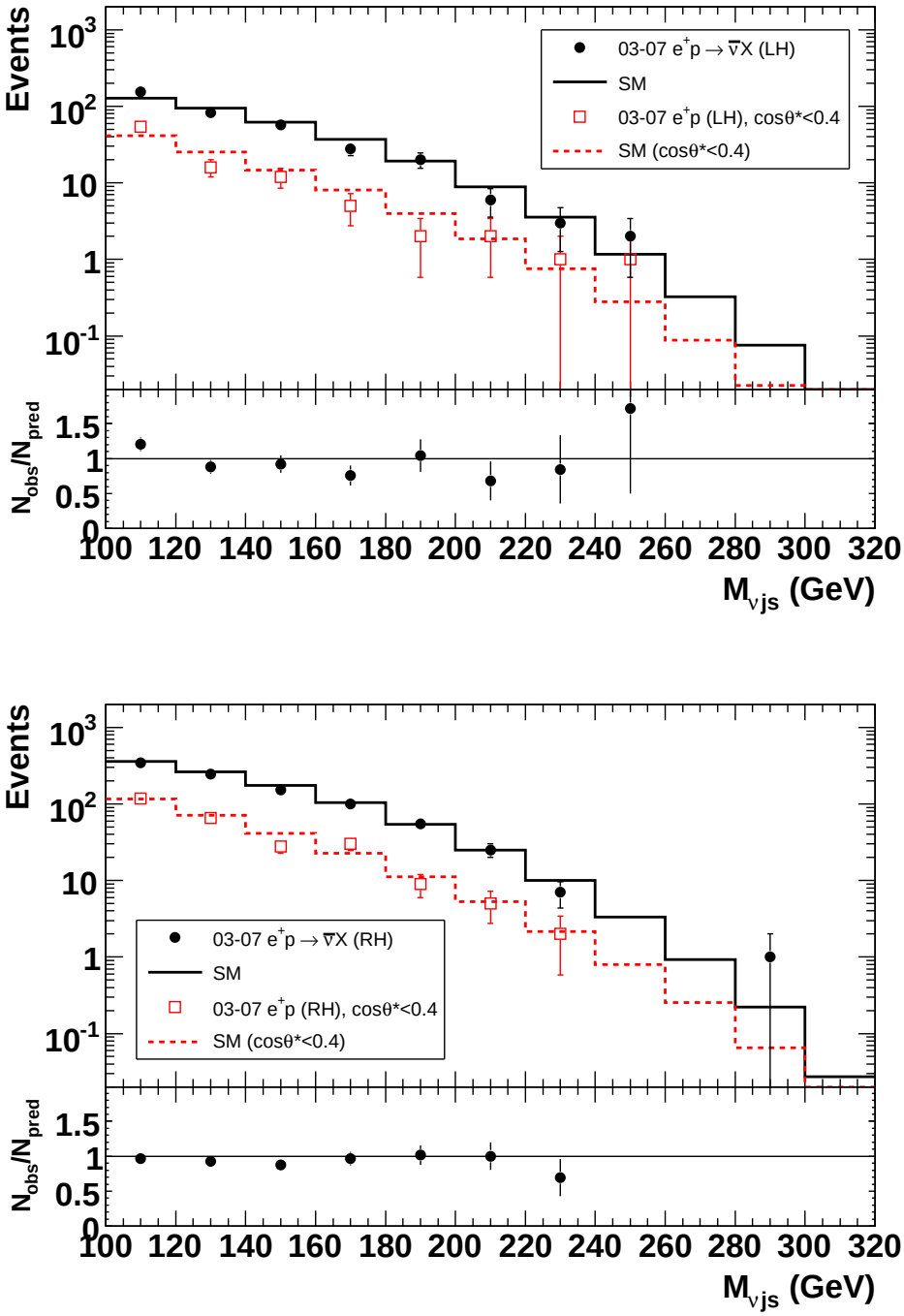

Figure 5.4: *Distributions of the invariant mass reconstructed from the neutrino and all jets for CC positron data (upper plot for left-handed positron data and lower plot for right-handed positron data). Shown are the mass spectra without the cut on* $\cos\theta^*$ *(full dots) and with the cut on* $\cos\theta^* < 0.4$ *(open squares). The lower halves of the plots show the ratio of the observed spectrum to the luminosity normalized SM expectation without the cut on* $\cos\theta^*$.

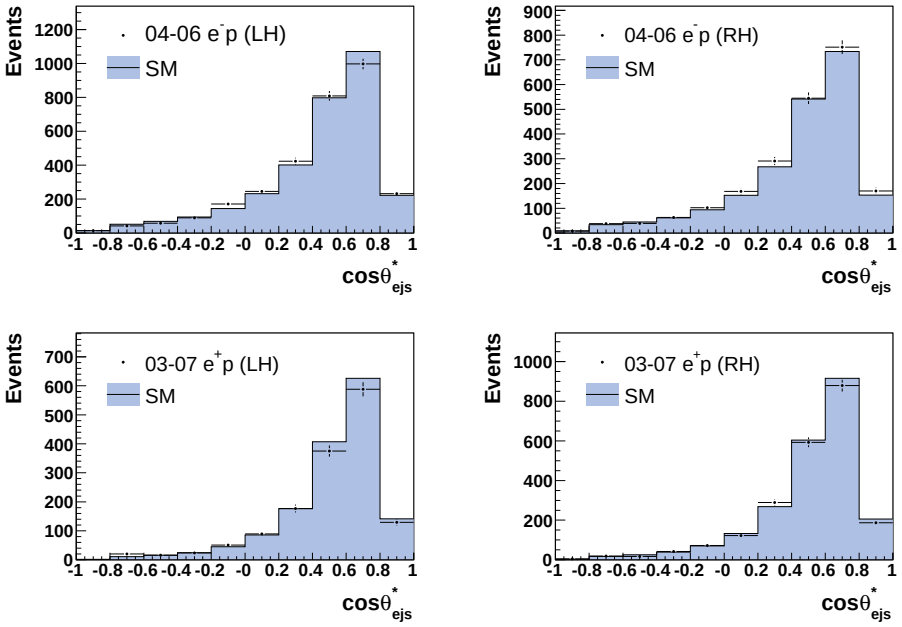

Figure 5.5: *Distributions of* $\cos\theta^*$ *reconstructed in the rest frame of the electron and all jets for the different NC data samples. The dots are the data and the histograms show the luminosity normalized Standard Model expectation.*

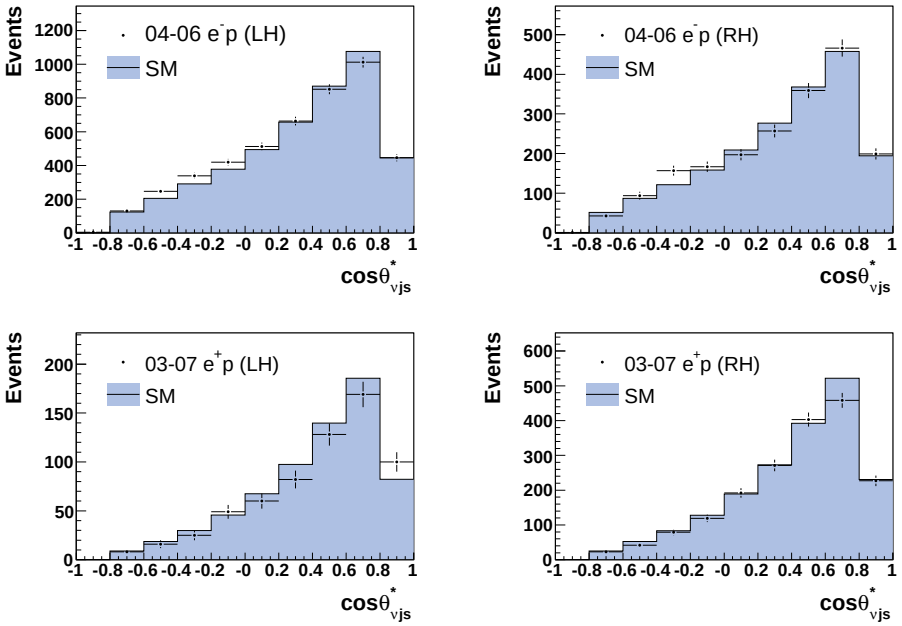

Figure 5.6: *Distributions of* $\cos\theta^*$ *reconstructed in the rest frame of the neutrino and all jets for the different CC data samples. The dots are the data and the histograms show the luminosity normalized Standard Model expectation.*

5.2 Systematic Uncertainties

Systematic uncertainties arise from uncertainties in the detector performance and calibration, from the indetermination of the theory used as input in the MC simulations, and from the resolution of the variables on which cuts are applied. The uncertainty originating from a systematic effect is estimated by applying the variation to the SM MC and comparing the resulting mass spectrum to the original one.

The uncertainty on the hadronic energy scale was determined to be 1% in both FCAL and BCAL [7, 9]. The uncertainty on the RCAL energy scale is neglected in this analysis since almost no energy is deposited there. The relative uncertainty between the HAC and EMC energy scales was estimated to be 2% [7]. The jet position uncertainty was determined to be 0.5 cm [69]. The uncertainty on the electron energy is 2% and was determined from measurements of E'_e/E_{DA} [9, 70]. Here, E'_e is the energy of the scattered electron after corrections for inactive material in the detector and for non-uniformities of the calorimeter, and E_{DA} is the energy of the scattered electron given in Eq. 4.16. The uncertainty on the electron scattering angle is 1 mrad and was determined from the comparison of the reconstructed scattering angle and the true scattering angle in the MC [9, 70]. It reflects the uncertainty in the alignment of the CAL with respect to the CTD. The uncertainty on the electron energy resolution was determined to be 1% [9, 70]. In the following, the systematic checks for both the NC and the CC analysis are described.

5.2.1 Neutral Current Events

The following sources of systematic uncertainties are considered:

for the electron: [9, 70]

1. energy scaled by $\pm 2\%$;
2. energy resolution used in MC varied by $\pm 1\%$;
3. polar angle varied by ± 1 mrad;

for jets: [7, 69]

4. FCAL energy $\pm 1\%$, BCAL energy $\pm 1\%$;
5. FCAL energy $\pm 1\%$, BCAL energy $\mp 1\%$;
6. FCAL EMC energy $\pm 2\%$, FCAL HAC energy $\pm 2\%$;

7. BCAL EMC energy ±2%, BCAL HAC energy ∓2%;
8. x-position on FCAL surface ±0.5 cm;
9. y-position on FCAL surface ±0.5 cm;
10. FCAL box cut ±0.5 cm in x-direction;
11. FCAL box cut ±0.5 cm in y-direction;

other sources

12. parton density $\pm 1\sigma$;
13. luminosity ±2.6%.

The checks on the jet energy are done by varying the energy of all calorimeter cells in the calorimeter part considered, except for the cells belonging to the highest probability electron candidate. The uncertainties on the PDFs are estimated using the parametrizations of EPDFLIB [71], which take into account uncertainties from experimental as well as theoretical input.

Figure 5.7 (electron data) and Figure 5.8 (positron data) show the relative systematic uncertainties arising from the different sources as a function of the invariant mass, as well as the total systematic uncertainty obtained by adding all the sources in quadrature. The energy uncertainties clearly dominate. The PDF uncertainty and the uncertainty of the luminosity measurement (which is not plotted here) also have a significant effect. At high masses, the variation of the FCAL box cut for the jets and the error on the electron angle are significant. The statistical uncertainty of the MC is negligible in comparison to the systematic uncertainty.

5.2.2 Charged Current Events

The following sources of systematic uncertainties are considered: [7, 69]

1. FCAL energy ±1%, BCAL energy ±1%;
2. FCAL energy ±1%, BCAL energy ∓1%;
3. FCAL EMC energy ±2%, FCAL HAC energy ±2%;
4. BCAL EMC energy ±2%, BCAL HAC energy ∓2%;

5. jet x-position on FCAL surface ±0.5 cm;
6. jet y-position on FCAL surface ±0.5 cm;
7. jet FCAL box cut ±0.5 cm in x-direction;
8. jet FCAL box cut ±0.5 cm in y-direction;
9. parton density $\pm 1\sigma$;
10. luminosity ±2.6%;
11. polarization ±4.2%.

As in the NC analysis, the uncertainties on the PDFs are estimated using the parametrizations of EPDFLIB [71]. For the calculation of the polarization, the polarimeter (LPOL or TPOL) that had a longer up-time during each run (in terms of ZEUS gated luminosity) is used. Since the TPOL error is larger than the LPOL error (Section 3.1.1), the TPOL error (4.2%) is used to determine the systematic uncertainty of the polarization measurement, in order to be conservative. The relative error due to the polarization measurement on the CC cross section (Eq. 2.10) and thus on the measured number of events is given in table 5.1 for the different data sets.

data set	$\Delta\sigma/\sigma$ (%)
03-07 LH e^+	2.42
03-07 RH e^+	1.02
04-06 LH e^-	0.88
04-06 RH e^-	1.78

Table 5.1: *Relative systematic error on the CC DIS cross section due to the polarization measurement.*

Figure 5.9 (electron data) and Figure 5.10 (positron data) show the relative systematic uncertainties arising from the different sources as a function of the invariant mass, as well as the total systematic uncertainty obtained by adding all error sources in quadrature. The energy uncertainty and the PDF error are the dominating sources. A significant effect also comes from the uncertainty of the luminosity measurement and the error on the polarization (both not plotted here). For positron data, the variation of the FCAL box cut is significant at high masses. The statistical uncertainty of the MC is negligible in comparison to the systematic uncertainty.

,

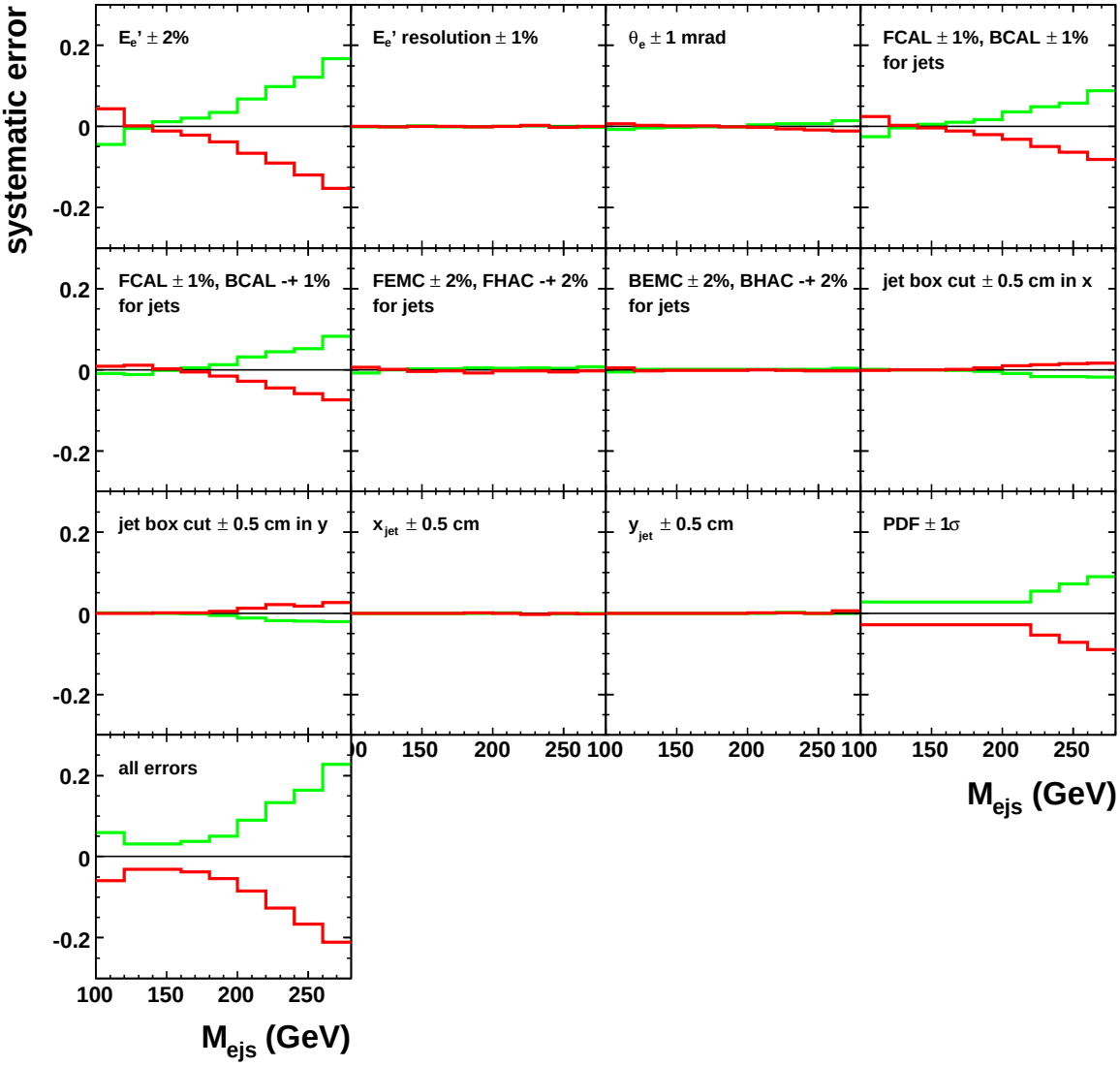

Figure 5.7: *Relative systematic error from different sources on the expected invariant mass spectrum for* **NC electron data**. *The last plot shows the overall uncertainty, calculated by summing all contributions in quadrature. The luminosity uncertainty of 2.6% is not shown.*

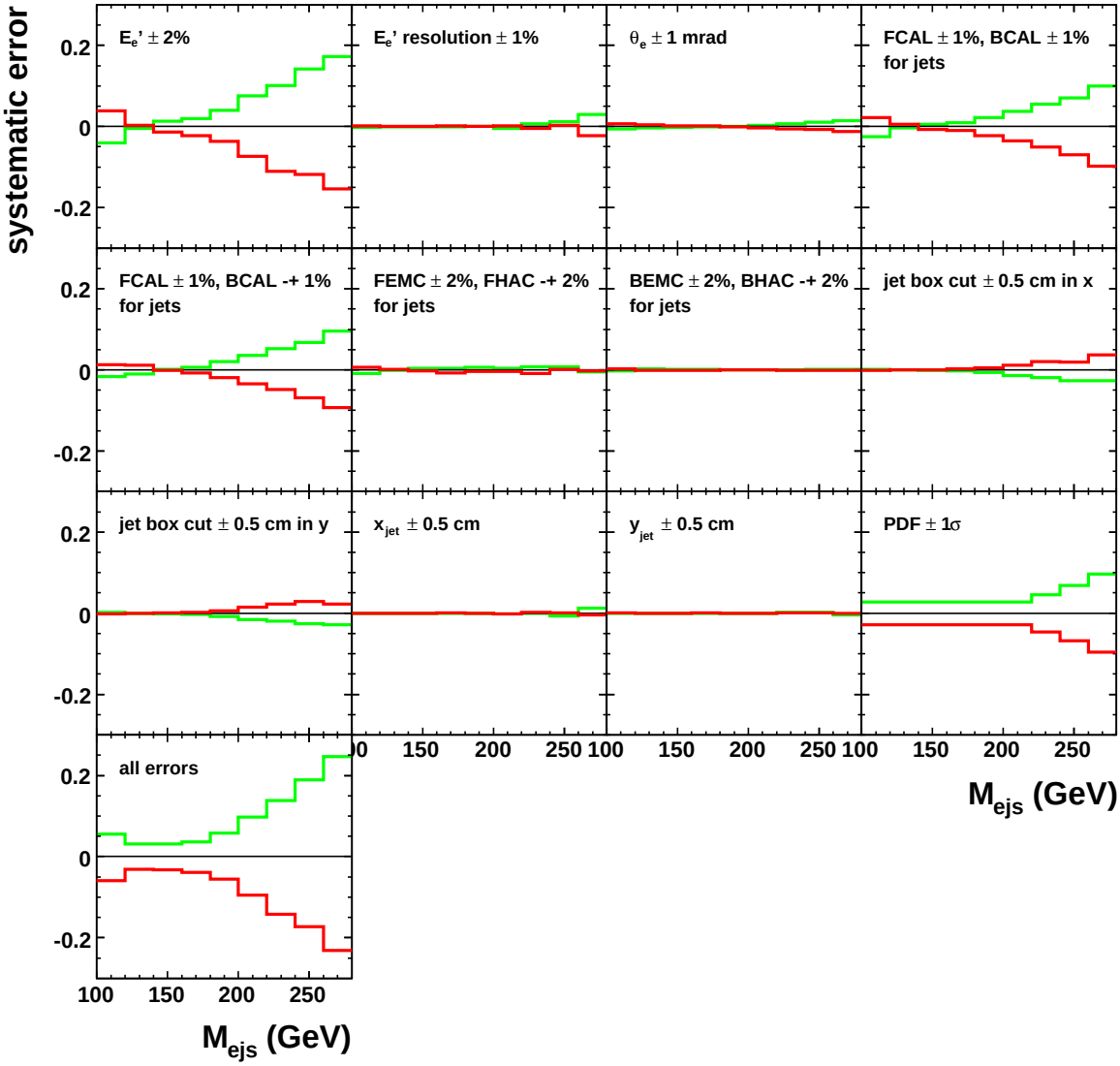

Figure 5.8: *Relative systematic error from different sources on the expected invariant mass spectrum for* **NC positron data**. *The last plot shows the overall uncertainty, calculated by summing all contributions in quadrature. The luminosity uncertainty of 2.6% is not shown.*

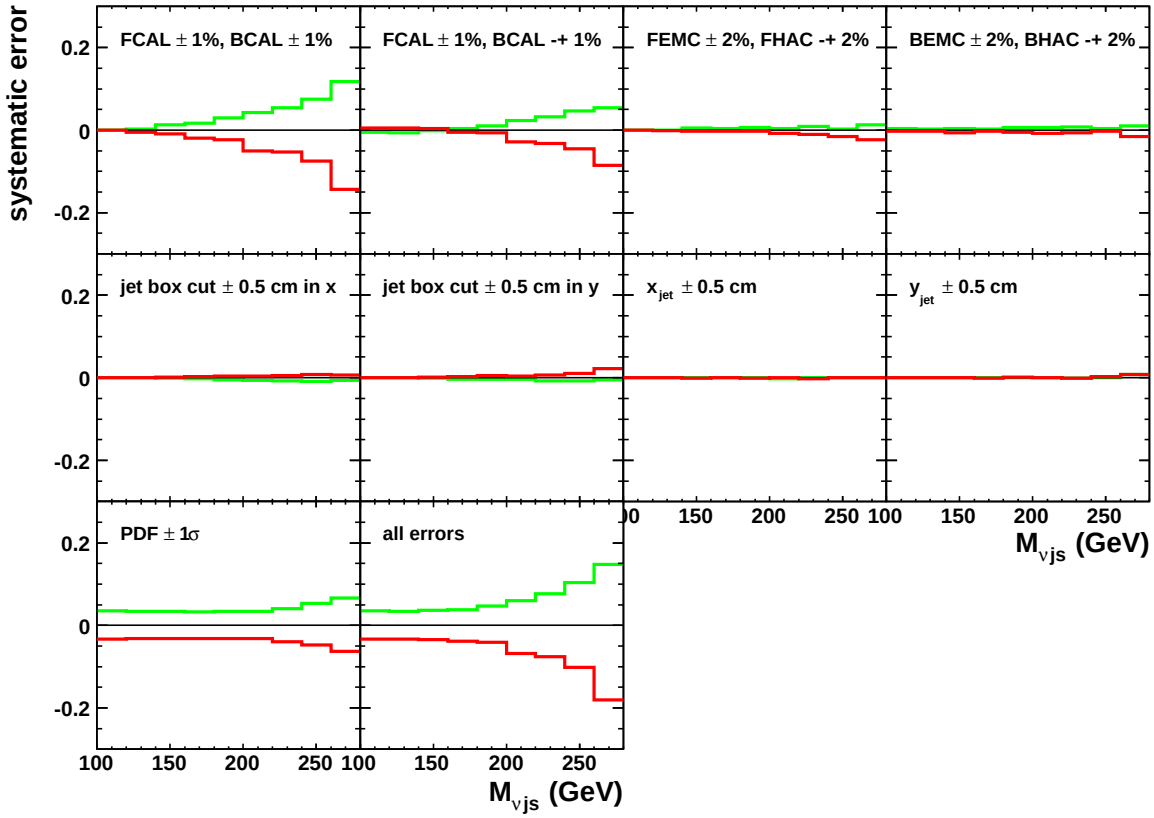

Figure 5.9: *Relative systematic error from different sources on the expected invariant mass spectrum for* **CC electron data**. *The last plot shows the overall uncertainty, calculated by summing all contributions in quadrature. The luminosity uncertainty of 2.6%, as well as the polarization error of 0.88% for LH data and 1.78% for RH data are not shown.*

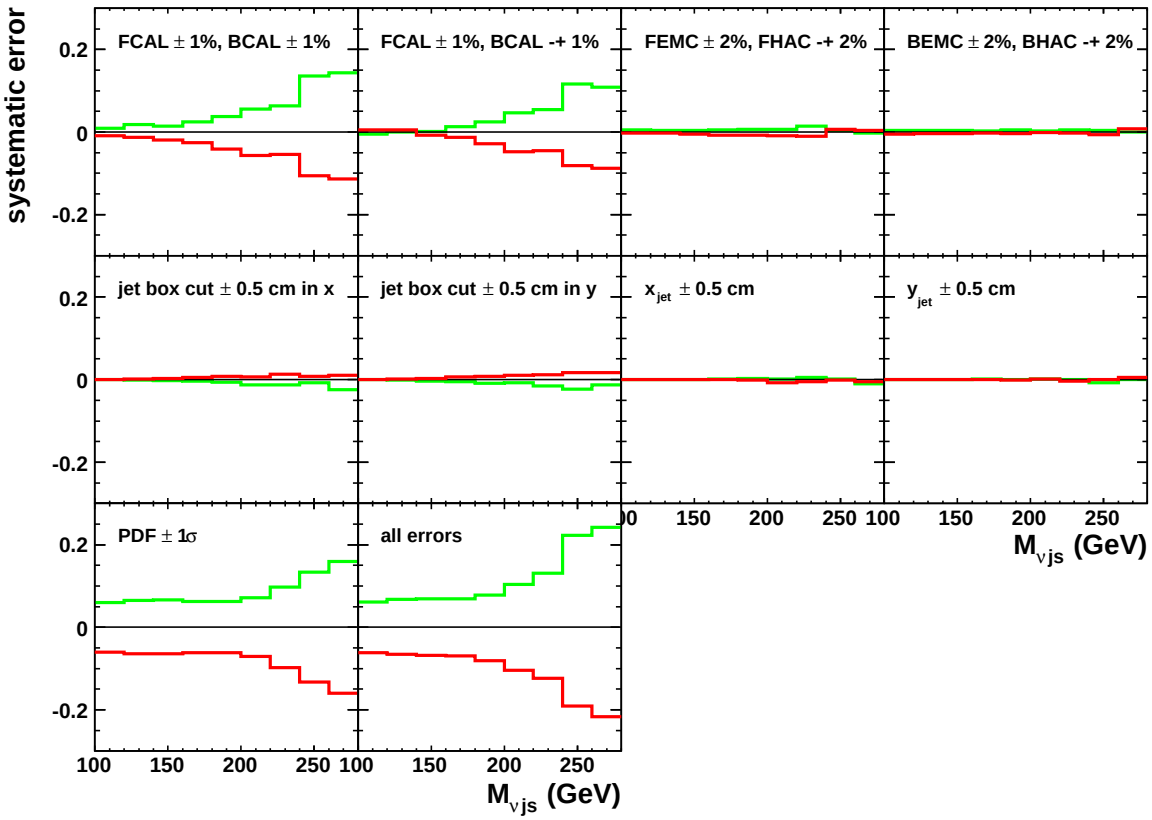

Figure 5.10: *Relative systematic error from different sources on the expected invariant mass spectrum for* **CC positron data**. *The last plot shows the overall uncertainty, calculated by summing all contributions in quadrature. The luminosity uncertainty of 2.6%, as well as the polarization error of 2.42% for LH data and 1.02% for RH data are not shown.*

Chapter 6

Limits on Leptoquark Production

No resonances or other deviations from the Standard Model are seen in the invariant mass distributions (Section 5.1). As mentioned in Section 2.4.2, M_{LQ} and λ are the only free parameters of leptoquarks in the Buchmüller-Rückl-Wyler model (assuming fixed branching fractions to eq and νq). Therefore, a hypothetical leptoquark must have a high mass M_{LQ} or a small Yukawa coupling λ (electron-quark-leptoquark coupling). Limits on λ are set as a function of M_{LQ}.

All limits were calculated including also the data recorded with the ZEUS detector in the years 1994-2000, the so-called HERA–I data taking period (Section 3.1), so that all HERA data is included in the following results. The HERA-I data was not reanalyzed, but the same input (data and MC distributions, systematic uncertainties) used for the published limits [72, 73, 69] was also used here. Figures 6.1 and 6.2 show the distributions of the invariant mass reconstructed from the lepton and all jets for HERA-I NC and CC data, respectively. The data are well described by the MC. The HERA–I period is divided into three subperiods with different lepton beam charge and center-of-mass energies, as given in Table 6.1. The average polarization was zero during the whole HERA–I period. The full limit analysis is therefore based on a sample of $\mathcal{L} = 488$ pb^{-1}.

data set	$\sqrt{s}$ (GeV)	lumi (pb^{-1})
94–97 e$^+$	300	48.5
98-99 e$^-$	318	16.7
99-00 e$^+$	318	66.3

Table 6.1: *Lepton beam charge, center-of-mass energy, and integrated luminosity of the three HERA–I data samples.*

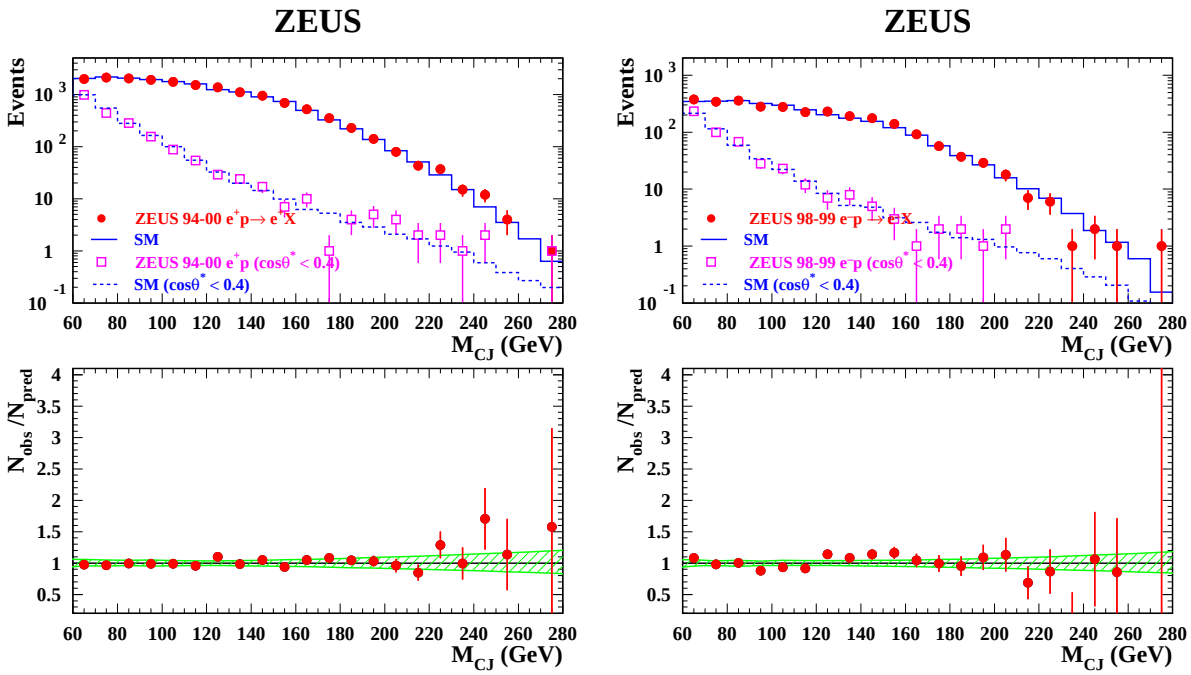

Figure 6.1: *Distributions of the invariant mass reconstructed from the electron and all jets for HERA-I NC data (left plot for positron data and right plot for electron data) [72, 69, 73]. Shown are the mass spectra without a cut on* $\cos\theta^*$ *(full dots) and with a cut on* $\cos\theta^* < 0.4$ *(open squares). The lower plots show the ratio of the observed spectrum to the luminosity normalized SM expectation without the cut on* $\cos\theta^*$*. The shaded area shows the overall uncertainty on the Standard Model expectation.*

6.1 Statistical Methods

6.1.1 Binning

Since leptoquark and NC/CC DIS events have a different invariant mass and $\cos\theta^*$ distribution (Section 2.4.3), the analysis is done in the $M - \cos\theta^*$ plane. Limits are set using events with invariant mass M_{ljs} from 150 to 320 GeV[1], where M_{ljs} is reconstructed from the lepton and all jets in the final state (Section 4.8). For both NC and CC DIS data, the M_{ljs}-$\cos\theta^*_{ljs}$ plane[2] is divided into 170 (17×10) bins, separately for each of the seven data sets (left-handed and right-handed electron and positron data, plus the three HERA–I

[1]Only events with $M_{ljs} > 150$ GeV are used because low LQ masses are already excluded by the Tevatron experiments.

[2]The angle θ^*_{ljs} is the lepton scattering angle reconstructed in the rest frame of the lepton and all jets in the final state.

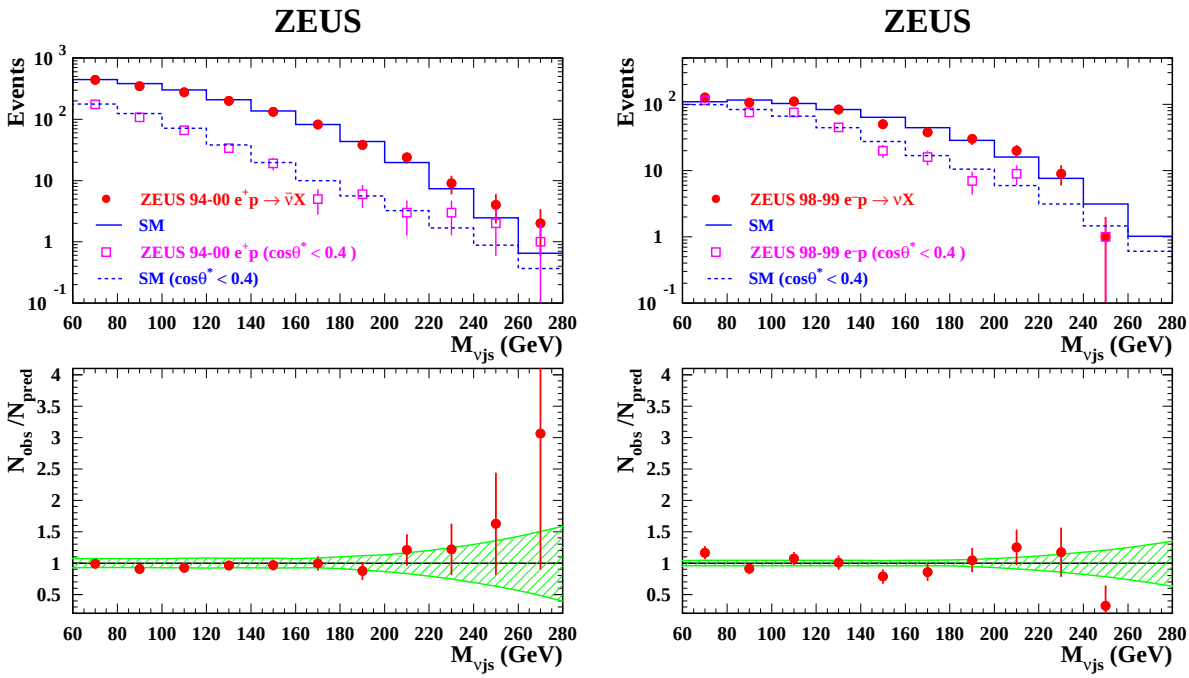

Figure 6.2: *Distributions of the invariant mass reconstructed from the electron and all jets for HERA-I CC data (left plot for positron data and right plot for electron data) [72, 73]. Shown are the mass spectra without a cut on* $\cos\theta^*$ *(full dots) and with a cut on* $\cos\theta^* < 0.4$ *(open squares). The lower plots show the ratio of the observed spectrum to the luminosity normalized SM expectation without the cut on* $\cos\theta^*$*. The shaded area shows the overall uncertainty on the Standard Model expectation.*

data sets). In total, 2380 bins are used for the limit setting, or 1190 for leptoquark types that can contribute only to NC DIS. The mass ($\cos\theta^*_{ljs}$) bins have a width of 10 GeV (0.2). The width of the mass bins corresponds to about 1σ of the resolution shown in Figure 4.24. Figure 6.3 shows the distribution of the selected NC DIS type and CC DIS type data events in the M_{ljs}-$\cos\theta^*_{ljs}$ plane. The same binning is used for the MC samples, to estimate the number of background events for each bin of each data set. As before, the MC is luminosity normalized.

6.1.2 Estimation of the Leptoquark Signal

To estimate the potential signal of a leptoquark with mass M_{LQ} and Yukawa coupling λ, the NC or CC DIS Monte Carlo is reweighted according to the LQ cross sections predicted in the BRW model. This has to be done separately for each LQ type, since

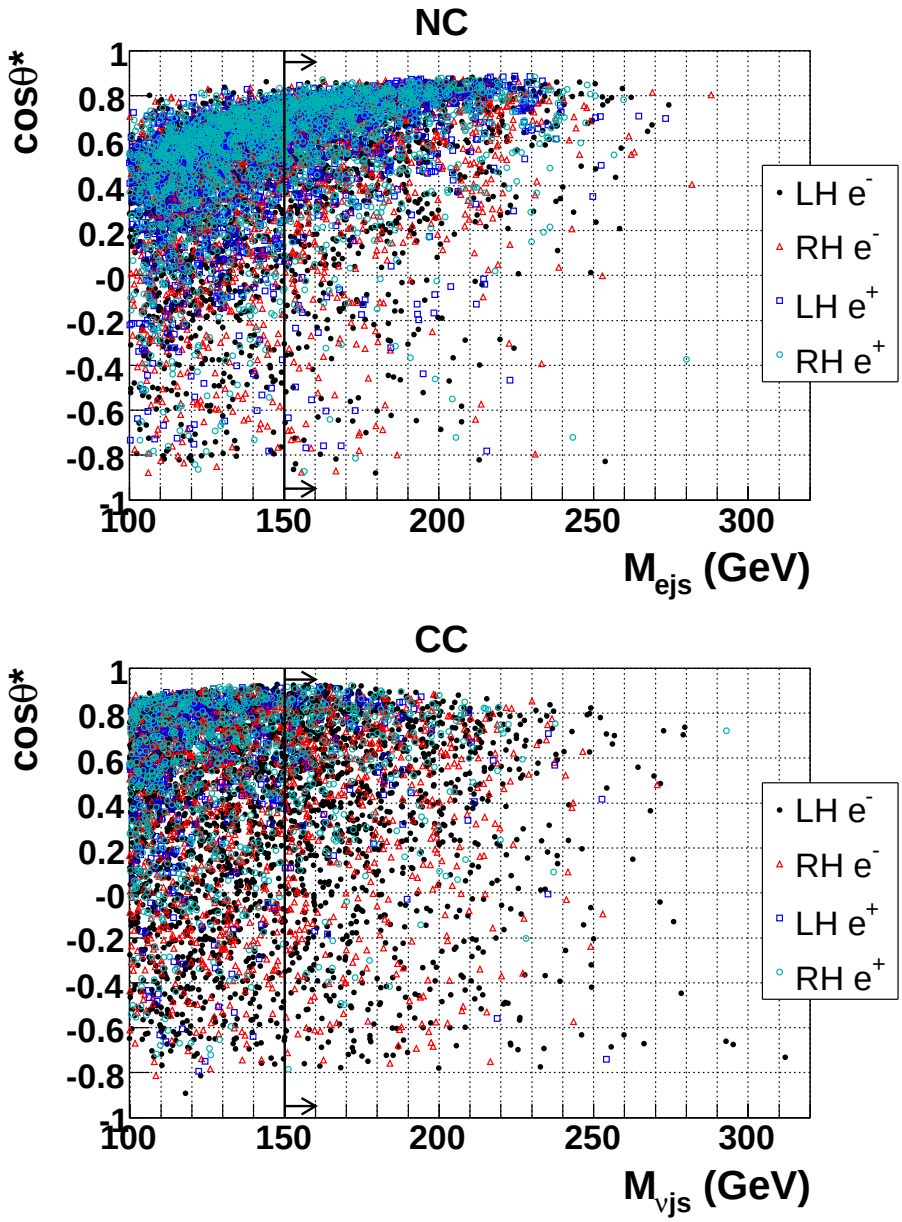

Figure 6.3: *Distribution of the selected NC (upper plot) and CC (lower plot) DIS type events in the* M_{ljs}-$\cos\theta^*_{ljs}$ *plane, for the different HERA–II data sets. All events with* $M_{ljs} > 150$ *GeV were used for the limit setting, the grid indicates the bins.*

the cross sections are different. A leptoquark signal MC is not used for the following two reasons: first, the interference of the leptoquark and the SM contributions cannot be taken into account if SM and signal MC are added to estimate the expected number of events; second, a lot of MC samples for different masses and couplings, for all 14 leptoquark types, would be needed in the limit setting procedure.

Each MC event is reweighted, in addition to the luminosity weighting, with the following weighting factor WF:

$$WF = \frac{\frac{d^2\sigma^{SM+LQ}}{dxdy}(x, y; P; M_{LQ}, \lambda)}{\frac{d^2\sigma^{SM}}{dxdy}(x, y; P)} = WF(x, y; P; M_{LQ}, \lambda), \tag{6.1}$$

where x and y are the true kinematic variables of the MC simulation, and P is the average polarization of the data sample given in Table 4.1[3]. As mentioned in Section 2.4.3, the LQ and the DIS cross sections in general have a different polarization dependence. Like in the MC simulation, the CTEQ5D PDFs [29] were used in the cross section calculation.

Since the coupling λ is constrained to be small for LQ masses below the HERA center-of-mass energy, the narrow-width approximation can be used to describe the s-channel resonance production:

$$\sigma^{NWA} = (J+1)\frac{\pi}{4s}\lambda^2 q(x_0, \mu^2), \tag{6.2}$$

where $q(x_0, \mu^2)$ is the quark density in the proton evaluated at $x_0 = m_{LQ}^2/s$ and $\mu^2 = m_{LQ}^2$ is the factorization scale. The cross section is smeared to take into account the limited detector resolution. The interference with the SM is also taken into account, while the u-channel contribution can be neglected.

Even though LQs with masses greater than the HERA center-of-mass energy cannot be produced as resonances, deviations in the invariant mass spectrum would be observed. Therefore, the limits can be extended beyond $\sqrt{s}$. All cross section terms are important and thus the full cross section is used:

$$\sigma(e^{\pm}p \to e^{\pm}(\nu)X) = \sigma_{SM} + \sigma_{s/SM}^{Int} + \sigma_{u/SM}^{Int} + \sigma_s + \sigma_u. \tag{6.3}$$

The use of the NWA below the HERA center-of-mass energy has the advantage that it is proportional to λ^2, while the full s-channel term has a more complicated dependence on λ for $M_{LQ} < \sqrt{s}$. The interference terms are approximately proportional to λ^2, and thus all cross section terms have a simple λ dependence. The same is true for $M_{LQ} > \sqrt{s}$, since the s-channel term is approximately proportional to λ^4 in this region, like the u-channel term, and the interference terms are approximately proportional to λ^2. When calculating the limit on λ for a fixed mass M_{LQ}, each cross section term thus needs to be calculated only once and then can be scaled for different values of λ.

Figure 6.4 shows the SM expectation for the left-handed electron sample as well as the reweighted SM expectation assuming a contribution from a S_0^R LQ state ($F = 2$) with a mass of 200 GeV and a coupling of $\lambda = 0.3$, in bins of x. These are the same LQ state

[3]For the HERA–I data samples, the average polarization is zero.

and the same values of M_{LQ} and λ as in Figure 2.6, which shows the theoretical cross section, and does not make use of the NWA. The peak in Figure 6.4 is broader since the cross section in the NWA is smeared to take into account the limited detector resolution.

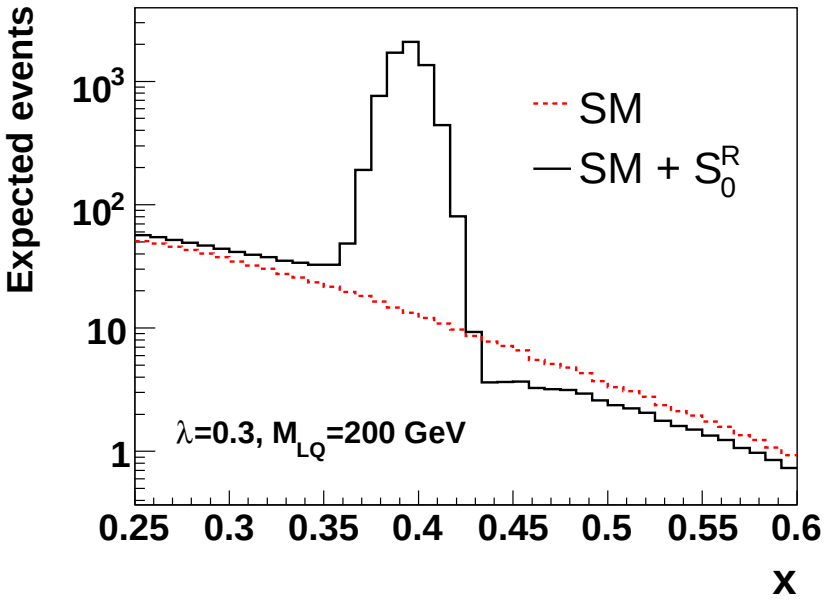

Figure 6.4: *SM expectation for the left-handed electron sample as well as the reweighted SM expectation assuming a contribution from a S_0^R LQ state ($F = 2$) with a mass of 200 GeV and a coupling of $\lambda = 0.3$, in bins of x.*

The sum of the MC weights ($w_{lumi} * WF$) of all events in the M_{ljs}-$\cos\theta^*_{ljs}$ bin i gives the expected number of events, $s_i + b_i$, in the presence of a leptoquark signal with mass M_{LQ} and coupling λ. Here, b_i is the Standard Model expectation, and s_i is the additional contribution due to the leptoquark and the interference terms, which depends on M_{LQ} and λ. Depending on size and sign of the interference terms, s_i can be both positive and negative. However, $s_i + b_i$ is always positive.

6.1.3 Systematic Uncertainties

For the limits using NC data, three different sources of systematic uncertainties are considered: the "energy" uncertainty (which includes all uncertaintys given in Section 5.2.1 added in quadrature, except for the PDF and the luminosity uncertainty), the PDF uncertainty and the luminosity uncertainty. For the PDF uncertainty, correlations between

different data sets are taken into account following the procedure in [73]. For limits using CC data, also the polarization uncertainty enters as an independent source, while it is negligible for NC data. For all sources of systematic uncertainties, Gaussian distributions are assumed. The uncertainties from the same source are assumed as correlated between different bins. For each bin, the uncertainty on the SM expectation is assumed to be equal to the uncertainty on the LQ signal, and they are assumed as correlated.

6.1.4 Bayesian Method

The likelihood in bin i is defined as the Poisson probability of observing d_i events when $s_i + b_i$ events are expected:

$$L_i = e^{-(s_i+b_i)} \frac{(s_i + b_i)^{d_i}}{d_i!} \tag{6.4}$$

Since s_i depends on M_{LQ} and λ, L_i also is a function of M_{LQ} and λ. The two-dimensional likelihood L is the product of the Poisson probabilities L_i of all considered M_{ljs}-$\cos\theta^*_{ljs}$ bins:

$$L(M_{LQ}, \lambda) = \prod_i L_i = \prod_i e^{-(s_i+b_i)} \frac{(s_i + b_i)^{d_i}}{d_i!} \tag{6.5}$$

With the Bayesian prior assumption of a uniform λ^2 distribution, the upper limit on the Yukawa coupling, λ_{limit}, as a function of M_{LQ} is obtained by solving the equation

$$\int_0^{\lambda^2_{\rm limit}} d\lambda^2 L(M_{LQ}, \lambda) = 0.95 \int_0^{\infty} d\lambda^2 L(M_{LQ}, \lambda). \tag{6.6}$$

This means that λ^2 is smaller than the obtained limit λ^2_{limit} with 95% probability.

Systematic effects are taken into account by convoluting the likelihood with a Gaussian distribution $G(\delta_j)$ for each source of systematic uncertainty j:

$$\begin{aligned} \mathcal{L} &= \prod_j \int_{-\infty}^{\infty} d\delta_j G(\delta_j) \cdot L(M_{LQ}, \lambda; \delta_j) \\ &= \prod_j \int_{-\infty}^{\infty} d\delta_j \frac{1}{\sqrt{2\pi}} e^{(-\delta_j^2/2)} \prod_i e^{-(s_i+b_i)'} \frac{(s_i + b_i)'^{d_i}}{d_i!}, \end{aligned} \tag{6.7}$$

where δ_j corresponds (approximately) to the variation of the $j^{\rm th}$ systematic uncertainty source in units of the relative systematic uncertainty, which is different in each bin i (Figures 5.7–5.10 show the systematic error in different bins of M_{ljs}, while for the limit setting it was determined in the M_{ljs}-$\cos\theta^*_{ljs}$ bins). The number of events in bin i after the systematic variation, $(s_i + b_i)'$, is given by

$$(s_i + b_i)' = (s_i + b_i) \prod_j (1 + c_{ij})^{\delta_j}, \tag{6.8}$$

where c_{ij} is the relative systematic uncertainty of source j on the observed number of events in bin i. This definition of $(s_i + b_i)'$ reduces to a linear dependence of $(s_i + b_i)'$ on each δ_j when δ_j is small while avoiding the possibility of $(s_i + b_i)'$ becoming negative, which would arise if $(s_i + b_i)'$ was defined as a linear function of the δ_j's.

The prior assumption of a uniform λ^2 distribution in Eq. 6.6 is chosen since the cross section in the narrow-width approximation is proportional to λ^2 (Eq. 2.15). The effect of the choice of the prior was found to be small. Figure 6.5 shows Bayesian limits on λ as a function of M_{LQ} for two different leptoquark states ($\tilde{S}^L_{1/2}$ and $\tilde{V}^L_{1/2}$), assuming a uniform λ distribution, a uniform λ^2 distribution, and a uniform λ^4 distribution. The change in the limits compared to the uniform λ^2 distribution is of the order of 10%.

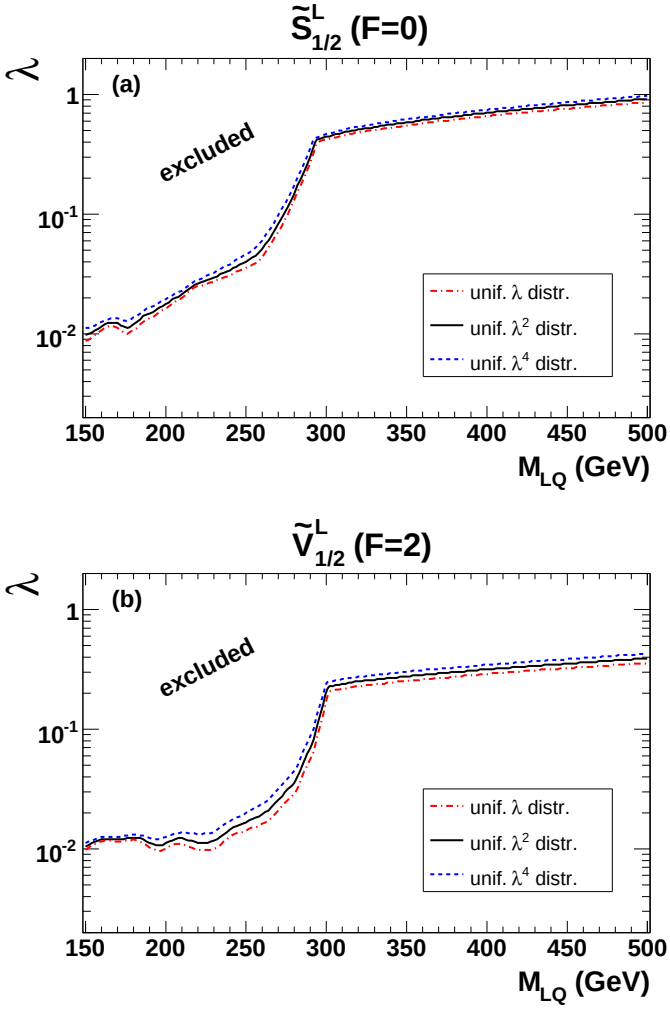

Figure 6.5: *Bayesian upper limits on the leptoquark Yukawa coupling λ as a function of the LQ mass, for different prior assumptions: a uniform λ distribution, a uniform λ^2 distribution, and a uniform λ^4 distribution. The limits for two different leptoquark types are shown: (a) $\tilde{S}^L_{1/2}$ (F=0), and (b) $\tilde{V}^L_{1/2}$ (F=2). All systematic uncertainties were included in the limit setting procedure.*

6.1.5 Frequentist Method

In addition to the Bayesian method, a modified frequentist approach based on fractional event counting [74] is used to set limits. To each bin i, a weight w_i, which is given by the asymmetry of the expected number of events in the presence or absence of a leptoquark signal, is assigned:

$$w_i = \frac{(s_i + b_i) - b_i}{(s_i + b_i) + b_i} = \frac{s_i}{s_i + 2b_i}. \tag{6.9}$$

The weight is small for bins with a poor signal-to-background ratio and thus these regions of phase space are suppressed in the limit setting procedure. A test statistic $X(d)$ is defined to merge all bins i in one discriminating variable:

$$X(d) = \sum_i w_i d_i \tag{6.10}$$

where d_i is the number of observed events in bin i. To estimate how well the data are described by the expected number of events in the presence (signal plus background hypothesis) or absence (background-only hypothesis) of a leptoquark signal, a large number of pseudo MC experiments are generated to reproduce the fluctuations of real data. For both hypotheses, 10000 pseudo experiments are generated which consist of random numbers obtained from Poisson distributions with mean values of $s_i + b_i$ (signal plus background hypothesis) or b_i (background-only hypothesis), for each bin i. In analogy to $X(d)$ (Eq. 6.10), a test statistic is defined for each pseudo MC experiment:

$$X(s+b) = \sum_i w_i N(s_i + b_i), \tag{6.11}$$

$$X(b) = \sum_i w_i N(b_i), \tag{6.12}$$

where $N(s_i + b_i)$ and $N(b_i)$ are the Poisson distributed random numbers from the pseudo experiments mentioned above. The confidence level CL_{s+b} (CL_b) for the signal+background (the background-only) hypothesis is defined as the fraction of pseudo MC experiments for which the quantity $X(s+b)$ ($X(b)$) is smaller than $X(d)$. If a value λ_{limit} corresponding to a confidence level CL_{s+b} (CL_b) of 5% is obtained, this means that for all values $\lambda > \lambda_{limit}$ the data distributions are predicted with less than 5% probability in the presence (absence) of a leptoquark signal, and thus λ is excluded with a confidence level $CL = 1 - CL_{s+b}$ ($CL = 1 - CL_b$) of 95%. In this analysis, a modified frequentist confidence level [74] for the exclusion of a leptoquark signal is used:

$$CL = 1 - \frac{CL_{s+b}}{CL_b} \tag{6.13}$$

This definition has the advantage that for a vanishing leptoquark coupling, which means $CL_{s+b} \to CL_b$, the confidence level CL is zero, and thus a leptoquark contribution cannot be excluded.

To include systematic uncertainties, the values of s_i+b_i (b_i) are altered for each pseudo MC experiment before $X(s+b)$ ($X(b)$) are calculated:

$$(s_i + b_i)' = (s_i + b_i)(1 + \sum_j c_{ij}\delta_j) \quad (6.14)$$

$$b_i' = b_i(1 + \sum_j c_{ij}\delta_j) \quad (6.15)$$

As in Eq. 6.7, c_{ij} is the relative systematic error in bin i from sorce j, and δ_j is a Gaussian random variable. In case that $(s_i+b_i)'$ is negative, a new random number δ_j is generated.

6.1.6 Comparison of Bayesian and Frequentist Limits

Figure 6.6 shows the Bayesian and frequentist upper limits on λ as a function of M_{LQ} for the leptoquark states $\tilde{S}^L_{1/2}$ and $\tilde{V}^L_{1/2}$, the systematic uncertainties were not included in the limit setting procedure. The Bayesian and the frequentist limits agree very precisely, within a few percent. Given the differenences in the two methods, it is not obvious that the limits agree. The differences between the Bayesian and the frequentist limits are much smaller than the differences in the Bayesian limits for different prior distributions, as can be seen from a comparison of Figure 6.6 and Figure 6.5[4]. This indicates that the prior assumption of a uniform λ^2 distribution is correct.

If the systematic uncertainties are included in the limit setting procedure, the frequentist limits are in general less stringent than the Bayesian limits, on average by 15% for LQ masses below $\sqrt{s}$ and by 35% for masses above $\sqrt{s}$. Figure 6.7 shows the limits for the same two leptoquark types as in Figure 6.6. A comparison with Figure 6.5 shows that these differences could not be explained by the prior assumption only. A more likely explanation is that the choice of the bin weights (Eq. 6.9) is not optimal in the presence of systematic uncertainties since bins with large systematic uncertainties should be downgraded in the analysis [74]. Since this was not done, only Bayesian limits will be used for the final results with a flat prior in λ^2.

[4]Figure 6.5 shows limits with systematic uncertainties included in the limit setting procedure, but without systematic uncertainties the differences in the limits with different prior assumptions are very similar.

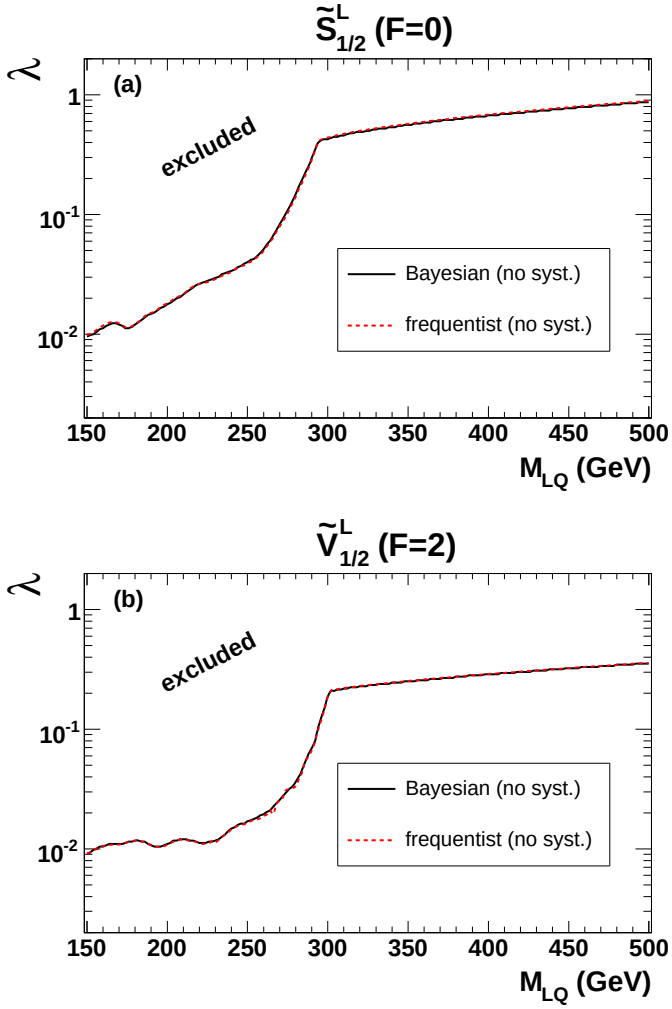

Figure 6.6: *Comparison of Bayesian (flat prior in λ^2) and frequentist upper limits on the leptoquark Yukawa coupling λ as a function of the LQ mass, for two different LQ types: (a) $\tilde{S}^L_{1/2}$ (fermion number F=0), and (b) $\tilde{V}^L_{1/2}$ (fermion number F=2). Systematic uncertainties were not included in the limit setting procedure for this figure.*

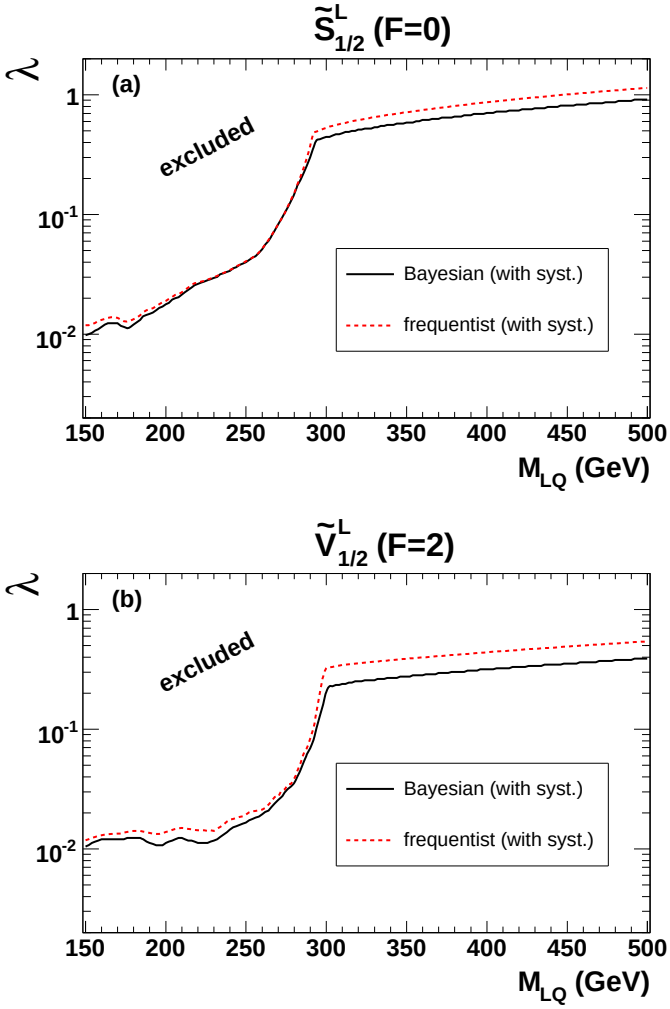

Figure 6.7: *Comparison of Bayesian (flat prior in λ^2) and frequentist upper limits on the leptoquark Yukawa coupling λ as a function of the LQ mass, for two different LQ types: (a) $\tilde{S}^L_{1/2}$ (F=0), and (b) $\tilde{V}^L_{1/2}$ (F=2). All systematic uncertainties were included in the limit setting procedure.*

6.2 Results

Figure 6.8 shows the Bayesian upper limits on the Yukawa coupling λ as a function of the leptoquark mass for all 14 LQ states. They range from 0.0036–0.018 for $M_{LQ} = 150$ GeV, and from 0.24–1.41 for $M_{LQ} = 500$ GeV. Assuming a fixed coupling λ, lower limits on the LQ mass can be read off from the plots. Table 6.2 shows the lower mass limits assuming $\lambda = 0.1$ and $\lambda = 0.3$, where the latter corresponds to the electromagnetic coupling $\lambda = \sqrt{4\pi\alpha}$. The limits range from 273–297 GeV for $\lambda = 0.1$, and from 289–630 GeV for $\lambda = 0.3$.

For low LQ masses ($M_{LQ} \lesssim 250$ GeV) the high background limits λ and thus the limits in Figure 6.8 increase only very little with the mass. In the intermediate mass region ($250 \lesssim M_{LQ} \lesssim 300$ GeV) there is almost no background and thus the raise in the limit on λ reflects the steep falling of the PDF (Equation 2.15). For high LQ masses ($M_{LQ} \gg \sqrt{s}$), the cross section only depends on the ratio of λ/M_{LQ} (Section 2.4.5) and thus the limits increase linear with the mass.

LQ type (F=0)	V_0^L	V_0^R	$\tilde{V}_0^R$	V_1^L	$S_{1/2}^L$	$S_{1/2}^R$	$\tilde{S}_{1/2}^L$
mass limit (GeV) ($\lambda = 0.1$)	279	276	294	297	292	293	273
mass limit (GeV) ($\lambda = 0.3$)	409	291	357	630	298	298	289
LQ type (F=2)	S_0^L	S_0^R	$\tilde{S}_0^R$	S_1^L	$V_{1/2}^L$	$V_{1/2}^R$	$\tilde{V}_{1/2}^L$
mass limit (GeV) ($\lambda = 0.1$)	294	293	274	295	278	293	293
mass limit (GeV) ($\lambda = 0.3$)	389	315	291	517	292	304	377

Table 6.2: *Bayesian lower mass limits for all 14 leptoquark types at* $\lambda = 0.1$ *and* $\lambda = 0.3$.

As mentioned in Section 2.4.6, the limit on the LQ state $\tilde{S}_{1/2}^L$ (S_0^L) can be interpreted as limit on $\lambda\sqrt{\beta}$ for an up-type squark $\tilde{u}_L$ (a down-type squark $\tilde{d}_R$), where λ is the coupling of $\tilde{u}_L$ to eq ($\tilde{d}_R$ to eq and νq) and β is the unknown branching fraction of the squarks to lepton (e or ν) and quark. The branching fractions of the squarks to eq and νq are assumed to be $\beta_{eq} = \beta,\ \beta_{\nu q} = 0$ for $\tilde{u}_L$, and $\beta_{eq} = 0.5\,\beta,\ \beta_{\nu q} = 0.5\,\beta$ for $\tilde{d}_R$.

For the four leptoquark states that can contribute to CC DIS, the combined search using both NC DIS and CC DIS data samples produces more stringent limits than the ones obtained from NC DIS data or CC DIS data alone. Figure 6.9 shows the limits using only the NC samples, only the CC samples, and the NC and CC samples combined, for all four LQ states. The sensitivity of the NC DIS and CC DIS samples are similar. The leptoquark states V_1^L and S_1^L (Figures 6.9b and 6.9d) each can be produced in two

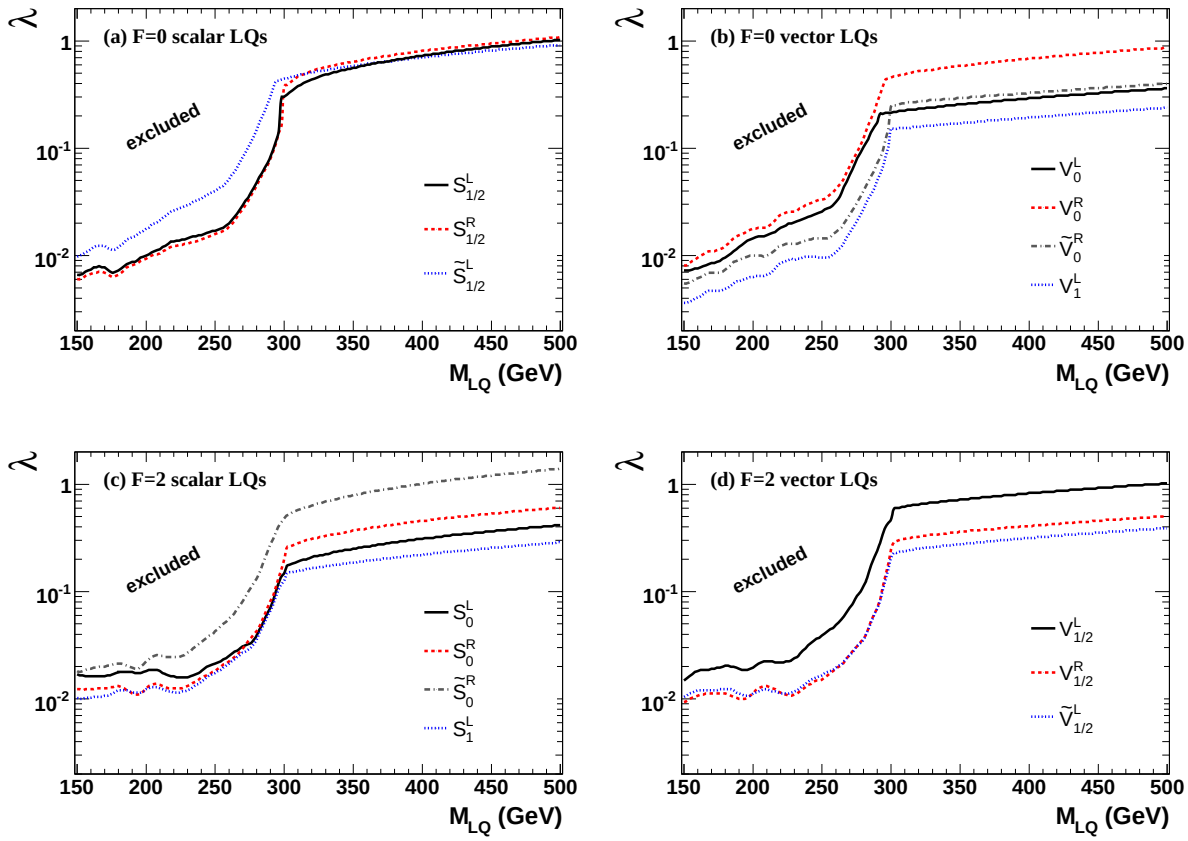

Figure 6.8: *Bayesian upper limits on the leptoquark Yukawa coupling λ as a function of the LQ mass, for scalar (a) and vector (b) leptoquarks with fermion number F=0, and for scalar (c) and vector (d) leptoquarks with fermion number F=2.*

different isospin states at HERA (Table 2.1) of which only one can decay to νq. Thus, the sensitivity of the NC DIS samples is higher, as can clearly be seen for $M_{LQ} < \sqrt{s}$.

Figure 6.10 shows the limits for two leptoquark states only sensitive to NC DIS, $\tilde{V}_0^R$ (F=0) and S_0^R (F=2), separately for electron and positron data, as well as the combined limit. For $M_{LQ} < \sqrt{s}$, leptoquarks with $F = 0$ are more sensitive to positron data and leptoquarks with $F = 2$ are more sensitive to electron data. This is due to the fact that leptoquarks with $F = 0$ ($F = 2$) are produced as resonances in e^+q and $e^-\bar{q}$ (e^-q and $e^+\bar{q}$) scattering, as mentioned in Section 2.4.3. Since the $\bar{q}$ PDF is smaller at high x than the q PDF, the production in $e^-\bar{q}$ ($e^+\bar{q}$) scattering is suppressed. For $M_{LQ} > \sqrt{s}$, the u-channel contribution becomes important and thus the behavior can be different, especially for vector leptoquarks, which have a different y dependence of the s-channel and u-channel terms, as well as the s-channel and u-channel interference terms, than scalar LQs.

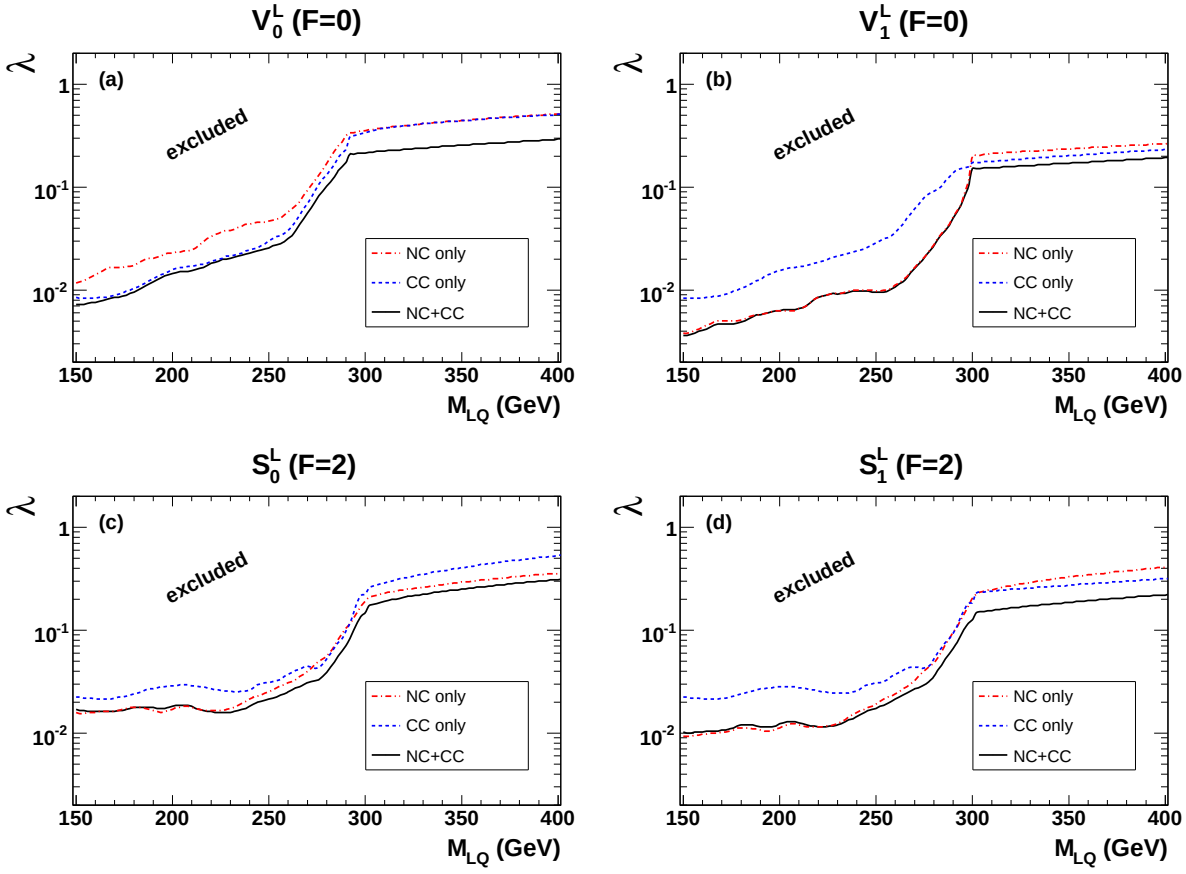

Figure 6.9: *Comparison of the upper limits extracted using NC data only, CC data only, and NC and CC data combined, for the four leptoquark types that can contribute to CC DIS: (a) V_0^L, (b) V_1^L, (c) S_0^L, and (d) S_1^L.*

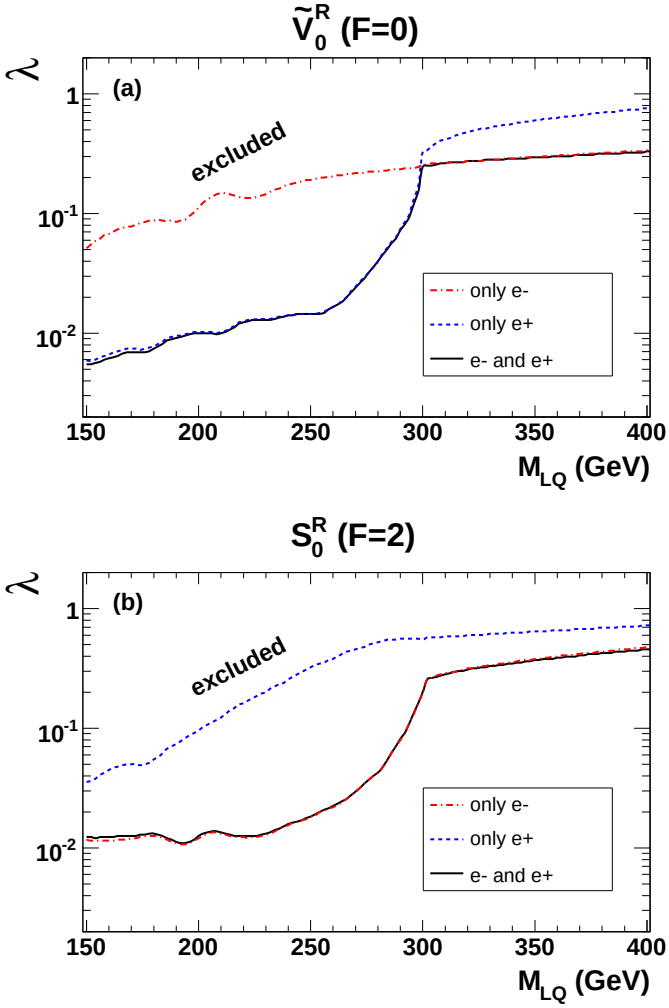

Figure 6.10: *Comparison of the upper limits extracted using electron data only, positron data only, and electron and positron data combined, for two different LQ types: (a) $\tilde{V}_0^R$ (F=0), and (b) S_0^R (F=2).*

6.3 Comparison with Other Experiments

The limits obtained in this analysis were compared with limits from the LEP experiments OPAL and L3, and the Tevatron experiment D0. In Figure 6.11, the comparison for two scalar leptoquark states ($\tilde{S}^L_{1/2}$ and S^L_0) is shown. For $M_{LQ} < \sqrt{s}$, the limits from this analysis are significantly better than the LEP limits, and for $M_{LQ} > \sqrt{s}$, they are comparable (for most LQ types better). The LEP limits shown here are obtained from a search for indirect effects in the process $e^+e^- \to q\bar{q}$ ([75], Section 2.4.4), which is the process giving the most stringent LEP limits. Limits combining data from all four LEP experiments, which are more stringent than the limits shown here, can be found in [76] (only for a coupling of $\lambda = 0.3$). Also shown in Figure 6.11 are the D0 limits from leptoquark pair production ([63], Section 2.4.4), which are independent of the Yukawa coupling λ. For scalar LQs that couple only to eq, like the $\tilde{S}^L_{1/2}$ (Figure 6.11a), masses up to 299 GeV are excluded, which corresponds to almost the whole region below the HERA center-of-mass energy ($\sqrt{s} = 318$ GeV). For scalar leptoquarks with a branching fraction of 0.5 to both eq and νq, like the S^L_0 (Figure 6.11b), masses up to 284 GeV are excluded. As mentioned in Section 2.4.4, the production cross section for vector LQs depends on the unknown coupling of the LQs to gluons. The Tevatron limits for vector LQs are in general higher than the ones for scalar LQs.

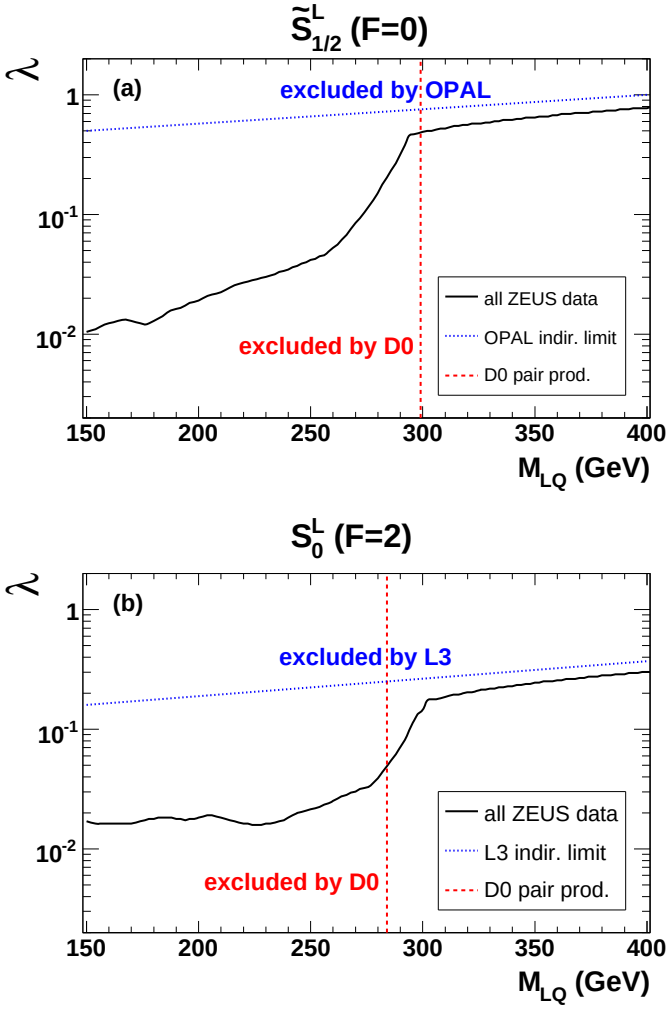

Figure 6.11: *Limits on the $\tilde{S}^L_{1/2}$ leptoquark (a) and the S^L_0 leptoquark (b) in the mass-coupling plane from OPAL/L3, D0, and ZEUS. The regions above the curves for OPAL, L3, and ZEUS, and to the left of the line for D0, are excluded.*

6.4 Heavy Leptoquark Limits

As mentioned in Section 2.4.5, heavy leptoquark exchange ($M_{LQ} \gg \sqrt{s}$) at HERA can be described by a four-fermion contact interaction with an effective coupling proportional to λ^2/M_{LQ}^2, and would lead to deviations from the SM cross sections. It follows that the limit on the coupling λ is a linear function of the leptoquark mass. The limits in Section 6.2 already show an approximately linear behavior for $M_{LQ} > \sqrt{s}$, but to make sure that there are no deviations from a linear behavior, the upper limit on λ was calculated at $M_{LQ} = 2$ TeV. Table 6.3 shows the values of (2 TeV)/λ_{lim}, which corresponds to the lower limit on M_{LQ}/λ, for all 14 LQ types. The limits range from 0.32 TeV for the $\tilde{S}_0^R$ LQ type to 2.14 TeV for the V_1^L LQ type. For the four LQ types that can contribute to CC DIS, the limits using the NC and CC samples combined as well as the limits using only the NC samples and using only the CC samples are shown.

LQ type	limit on M_{LQ}/λ (TeV)		
	NC+CC	NC only	CC only
$S_{1/2}^L$		0.42	
$S_{1/2}^R$		0.42	
$\tilde{S}_{1/2}^L$		0.51	
V_0^L	1.42	0.76	0.85
V_0^R		0.57	
$\tilde{V}_0^R$		1.31	
V_1^L	2.14	1.58	1.70
S_0^L	1.11	0.98	0.61
S_0^R		0.76	
$\tilde{S}_0^R$		0.32	
S_1^L	1.66	0.83	1.20
$V_{1/2}^L$		0.50	
$V_{1/2}^R$		1.02	
$\tilde{V}_{1/2}^L$		1.31	

Table 6.3: *Lower limit on the ratio of the leptoquark mass M_{LQ} to the Yukawa coupling λ, for all 14 leptoquark types. The upper part of the table shows the LQs with $F = 0$, the lower part the LQs with $F = 2$. For the four LQ types that can contribute to CC DIS, the limits using the NC and CC samples combined as well as the limits using only the NC samples and using only the CC samples are shown.*

Chapter 7

Conclusion

In this thesis, a search for first generation leptoquarks in the Buchmüller-Rückl-Wyler model was presented. Leptoquarks are hypothetical scalar or vector bosons carrying both lepton and baryon number, as well as color charge and fractional electric charge. The existence of leptoquarks would lead to resonances or other deviations from the Standard Model in the spectrum of the invariant mass of lepton and jets in the final state of polarized NC and CC DIS.

Data recorded with the ZEUS detector from 2003–2007, corresponding to an integrated luminosity of 356 pb^{-1}, were analyzed. No deviations from the Standard Model were found. This data was combined with the HERA-I data which was not reanalyzed but included as published previously [72]. The full HERA data sample, corresponding to $\mathcal{L} = 488\,\text{pb}^{-1}$, was used to set upper limits on the Yukawa coupling λ of the 14 Buchmüller-Rückl-Wyler leptoquark states as a function of the leptoquark mass. The limits were set using a Bayesian and a frequentist method for masses up to 500 GeV. Both results were found to agree within a few % for a bayesian prior flat in λ^2 if no systematic uncertainties were included. The inclusion of systematic uncertainties caused differences between the two methods which might be due to the treatment of systematic uncertainties in the frequentist limit setting procedure, which was not fully optimized.

The Bayesian lower limits on the leptoquark mass including all systematic uncertainties range from 289–630 GeV (273–297 GeV) assuming the coupling $\lambda = 0.3$ ($\lambda = 0.1$). Furthermore, limits were set on the ratio between the leptoquark mass and the Yukawa coupling, M_{LQ}/λ, in the limit of large leptoquark masses, $M_{LQ} \gg \sqrt{s}$. They range from 0.32–2.14 TeV.

The limits were compared with the results from LEP and found to be significantly better for $M_{LQ} < \sqrt{s}$ and similar or better for $M_{LQ} > \sqrt{s}$. The D0 limits on scalar

leptoquarks are only slightly lower than the HERA center-of-mass energy, especially for the 10 leptoquark types decaying only to $e + q$ final states.

At the end of this year the Large Hadron Collider (LHC) will start operation. It has potential to discover leptoquarks with masses of more than 1 TeV [77]. If leptoquarks will be discovered at the LHC, the Large Hadron Electron Collider (LHeC), which might succeed the LHC, will be able to determine additional quantum numbers of these leptoquark states [78].

Acknowledgements

First of all I would like to thank my supervisor Prof. Peter Schleper for his help and support and for giving me the opportunity to work on physics beyond the Standard Model in his group. A big thanks to Prof. Robert Klanner for his help concerning physics and organizational matters. Many thanks to JProf. Johannes Haller for the second opinion on this thesis.

A big thanks to my advisor Jolanta Sztuk-Dambietz for guiding me through this analysis and for always having time for my questions. It was a pleasure to work together with you!

I am very grateful to Monica Turcato, Peter Schleper and Robert Klanner for reading draft versions of this thesis, making a lot of useful suggestions and answering the questions that came up while I was writing.

Many thanks to all the people from the Hamburg University ZEUS/CMS group and from the ZEUS collaboration for the good working atmosphere. Special thanks to Friederike Januschek and Matthias Schröder with whom I shared an office during (part of) my phd time, to Jörg Behr and Christian Blohm for all the lunches we survived together in the canteen, and to Christian for many discussions concerning the CC analysis and frequentist limits.

I like to work in the high-Q^2 group, a big thanks thanks to everybody and especially to the coordinators and the "NC and CC guys" for answering many questions.

I enjoyed to work in the ZEUS calorimeter group, many thanks to everybody. A big thanks to Ingrid Gregor for her help and support with the halo muon studies. It's a pity that there was no time to finish it and make it part of this thesis!

Last but not least I would like to thank my parents, my sister, my brother-in-law and my friends for their support and for cheering me up when things didn't go as I wanted :-)

Appendix A

Control Distributions for Neutral Current

In this chapter, the NC control distributions for positron data and right-handed electron data are shown. The control distributions for left-handed electron data can be found in Section 4.6.3.

A.1 Right-handed Electron Data

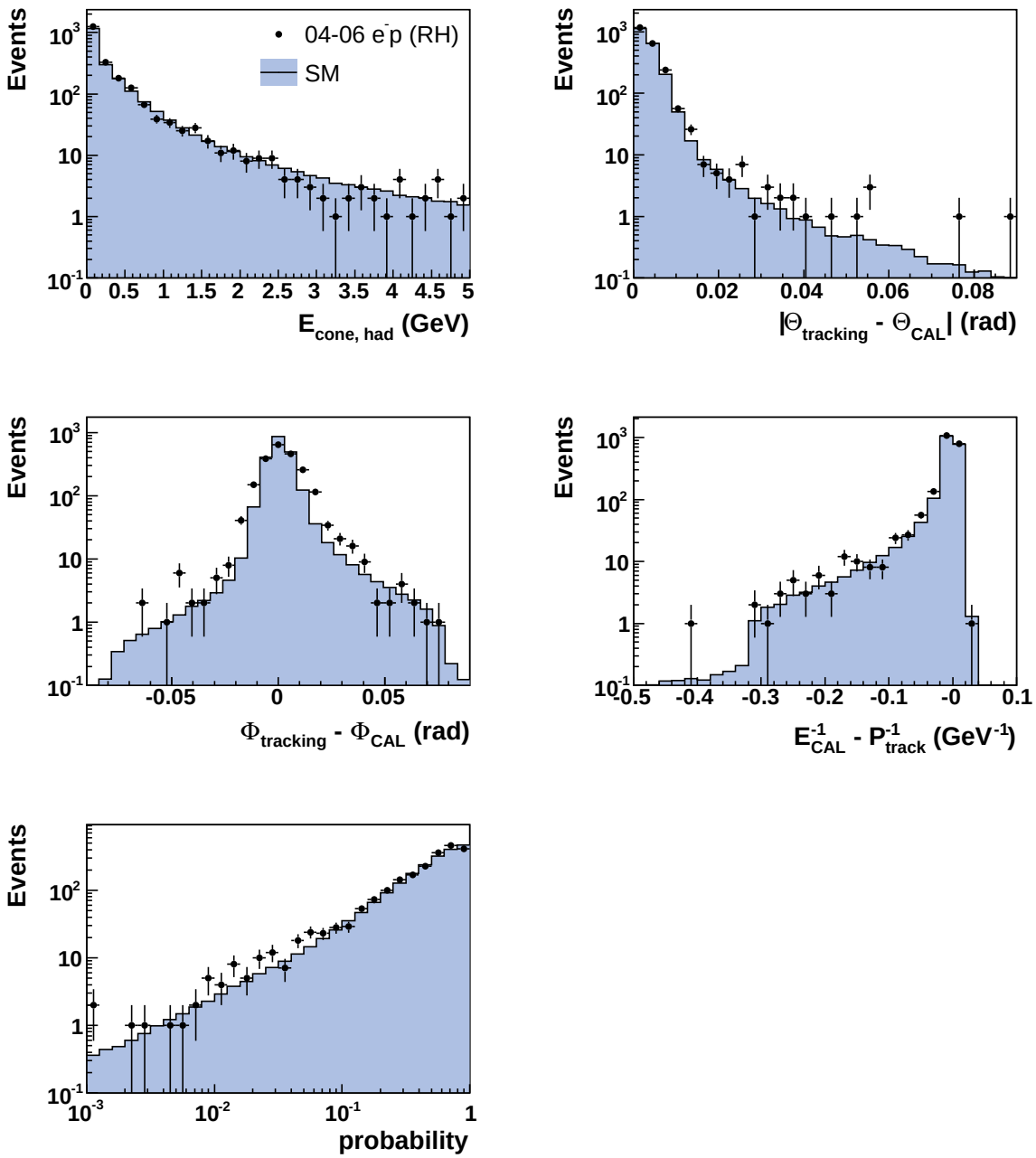

Figure A.1: *Variables used by the EM finder for the evaluation of the electron probability, and the electron probability itself, shown for right-handed electron data after all selection cuts. The dots are the data and the histograms show the luminosity normalized Standard Model expectation.*

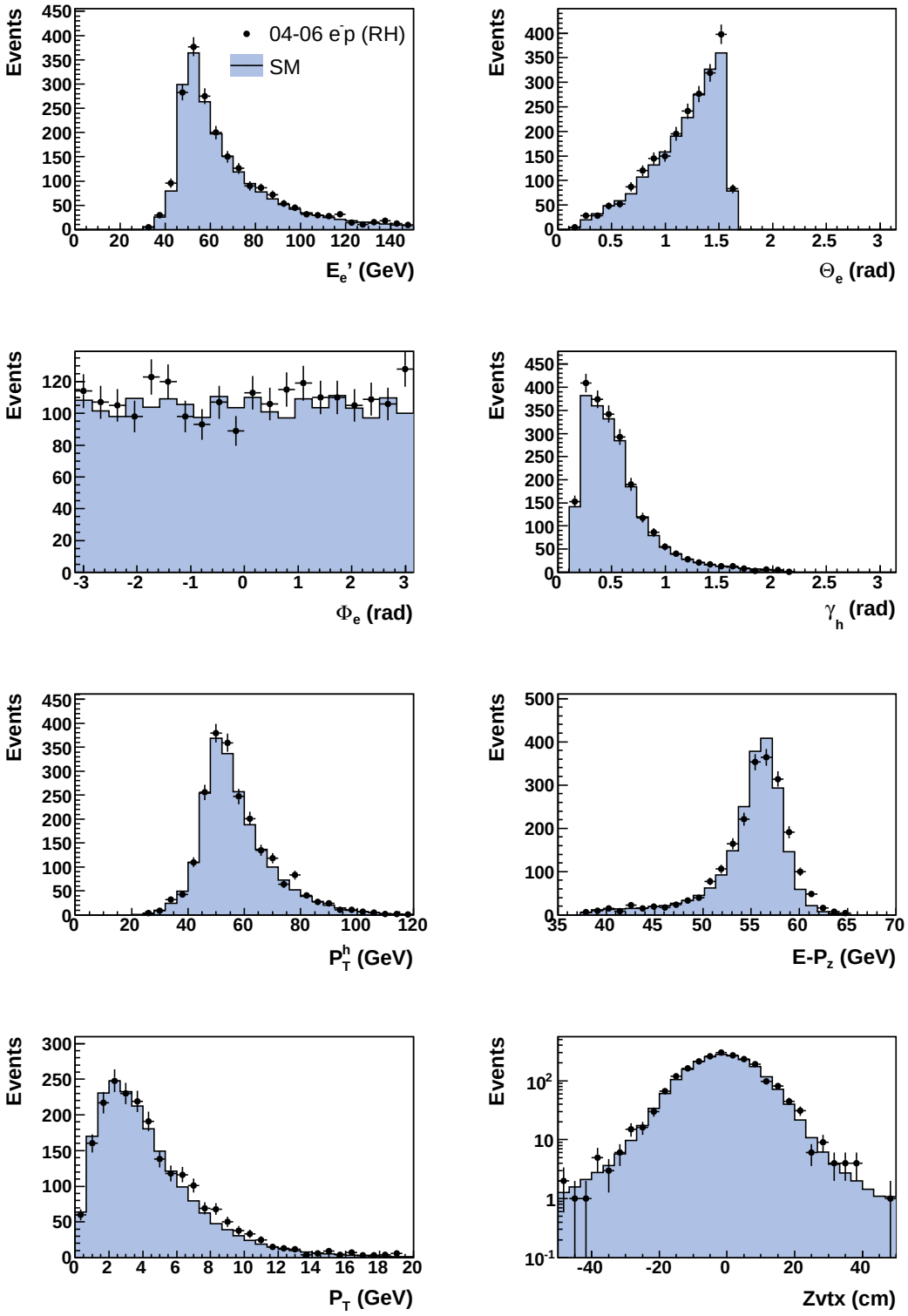

Figure A.2: *Electron, hadronic, and global variables for right-handed electron data after all selection cuts. The dots are the data and the histograms show the luminosity normalized Standard Model expectation.*

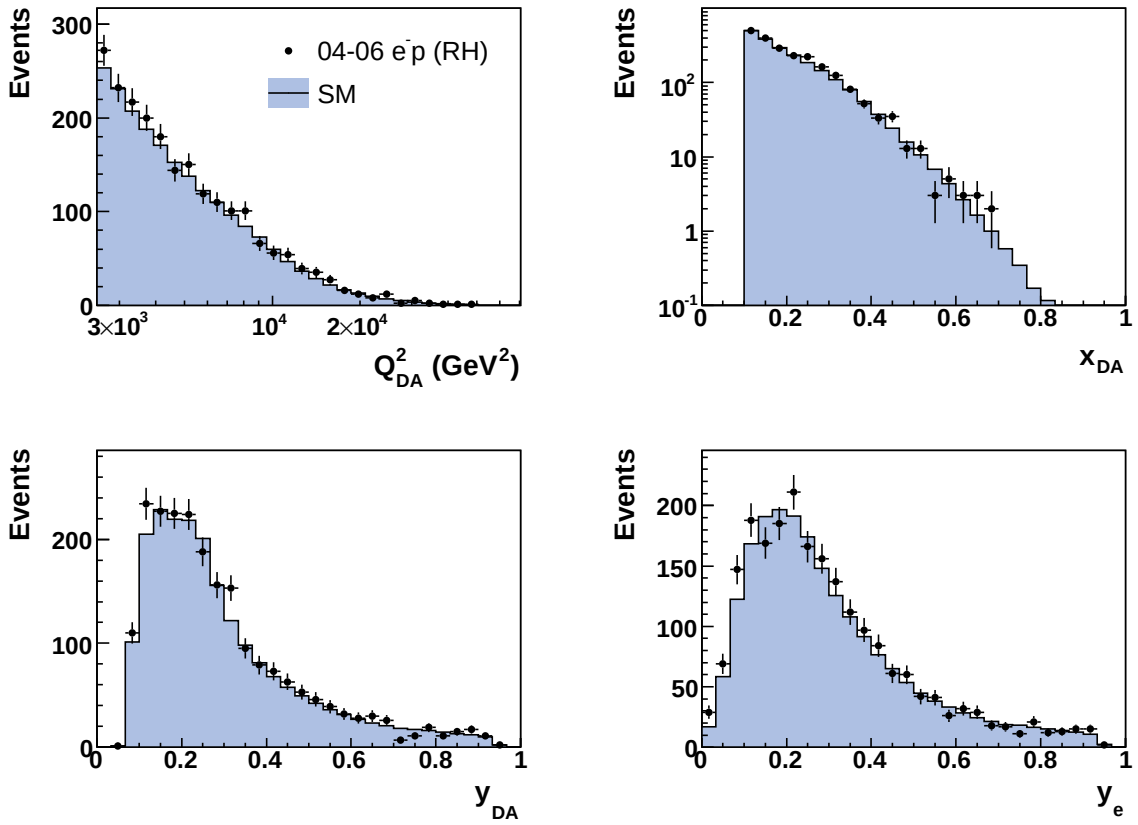

Figure A.3: *Kinematic variables for right-handed electron data after all selection cuts. The dots are the data and the histograms show the luminosity normalized Standard Model expectation.*

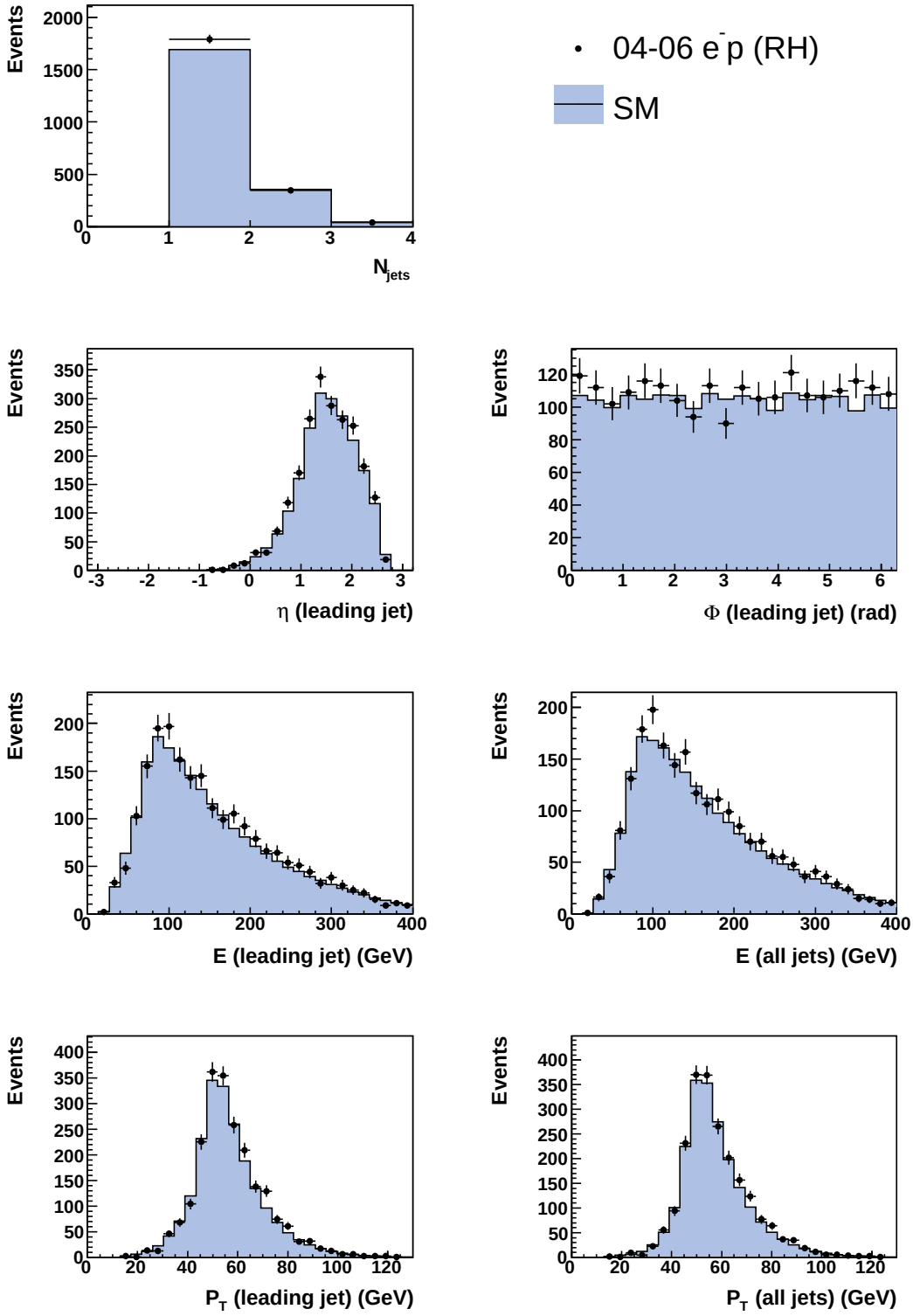

Figure A.4: *Jet variables for right-handed electron data after all selection cuts. The dots are the data and the histograms show the luminosity normalized Standard Model expectation.*

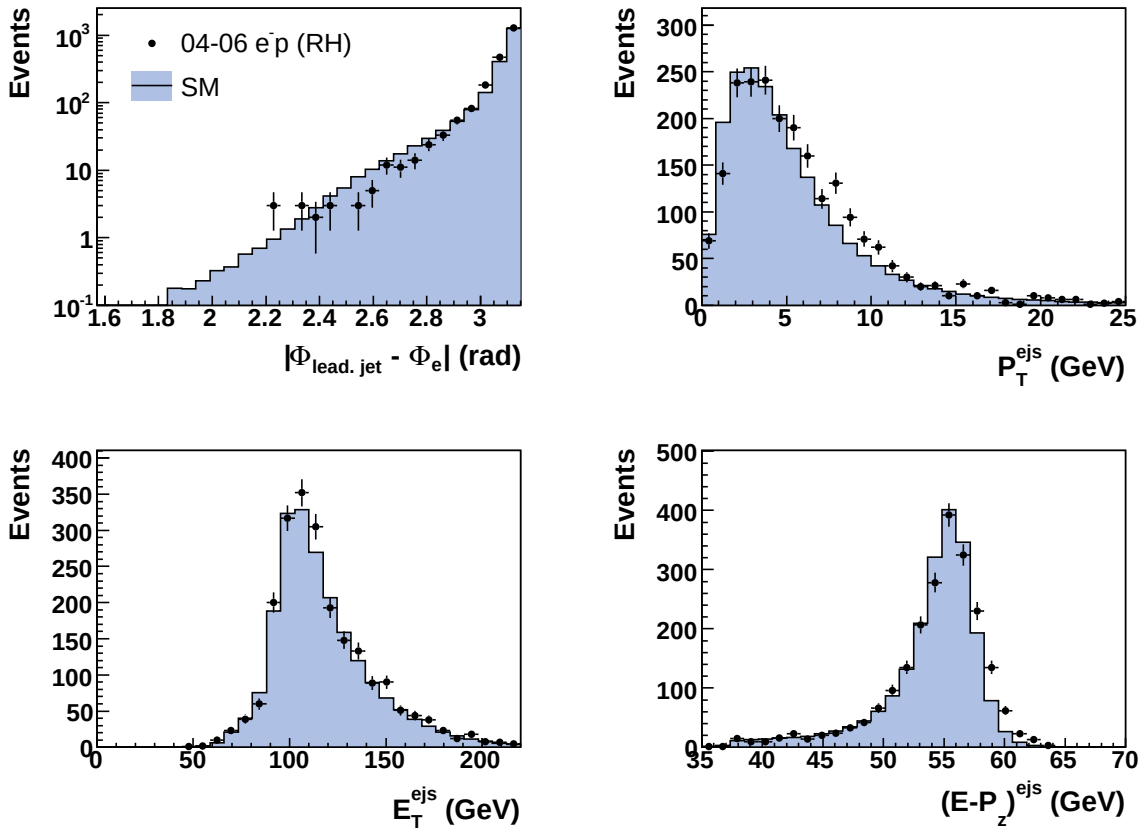

Figure A.5: *Variables from electron and jet information for right-handed electron data after all selection cuts. The dots are the data and the histograms show the luminosity normalized Standard Model expectation.*

A.2 Left-handed Positron Data

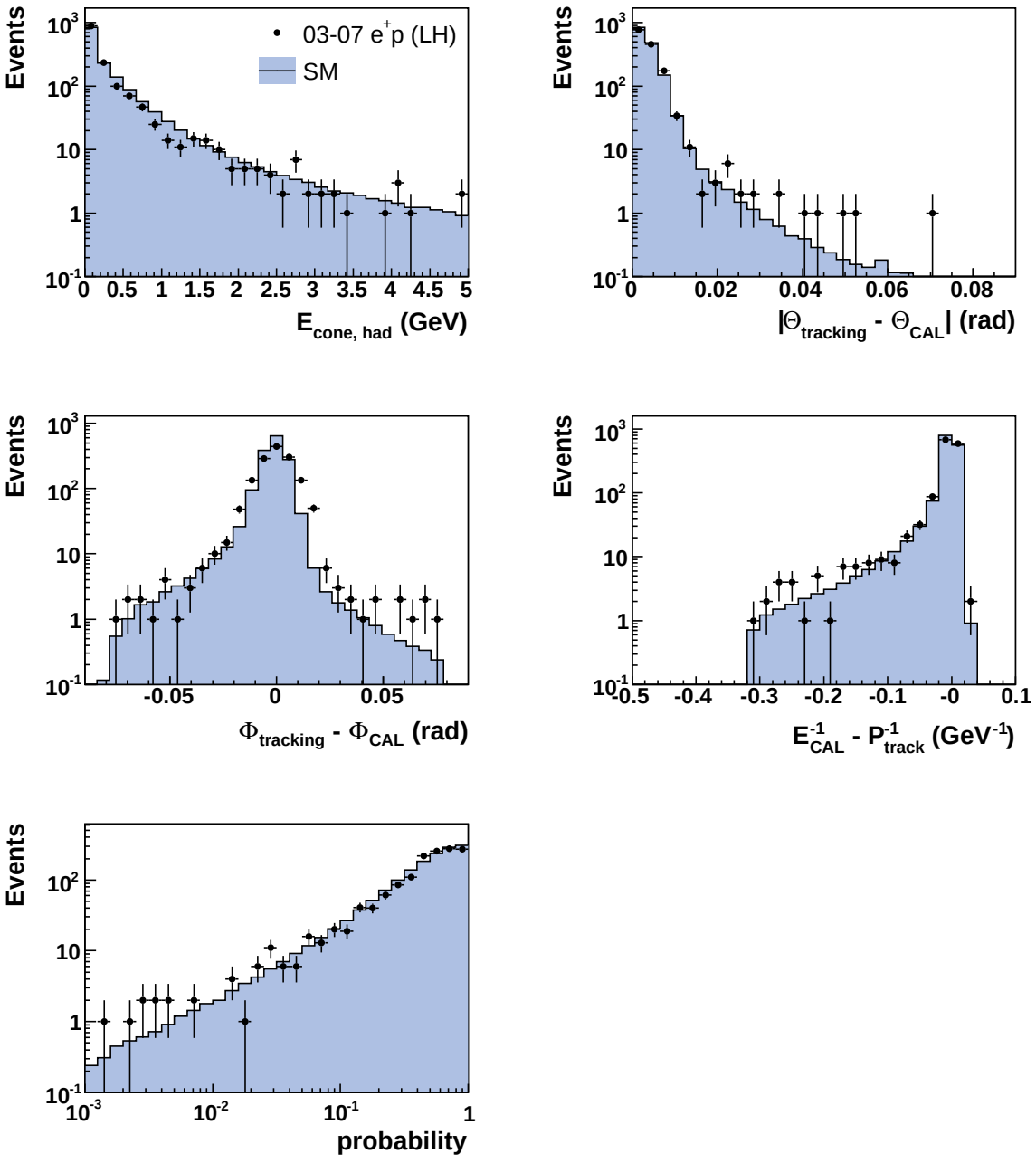

Figure A.6: *Variables used by the EM finder for the evaluation of the electron probability, and the electron probability itself, shown for left-handed positron data after all selection cuts. The dots are the data and the histograms show the luminosity normalized Standard Model expectation.*

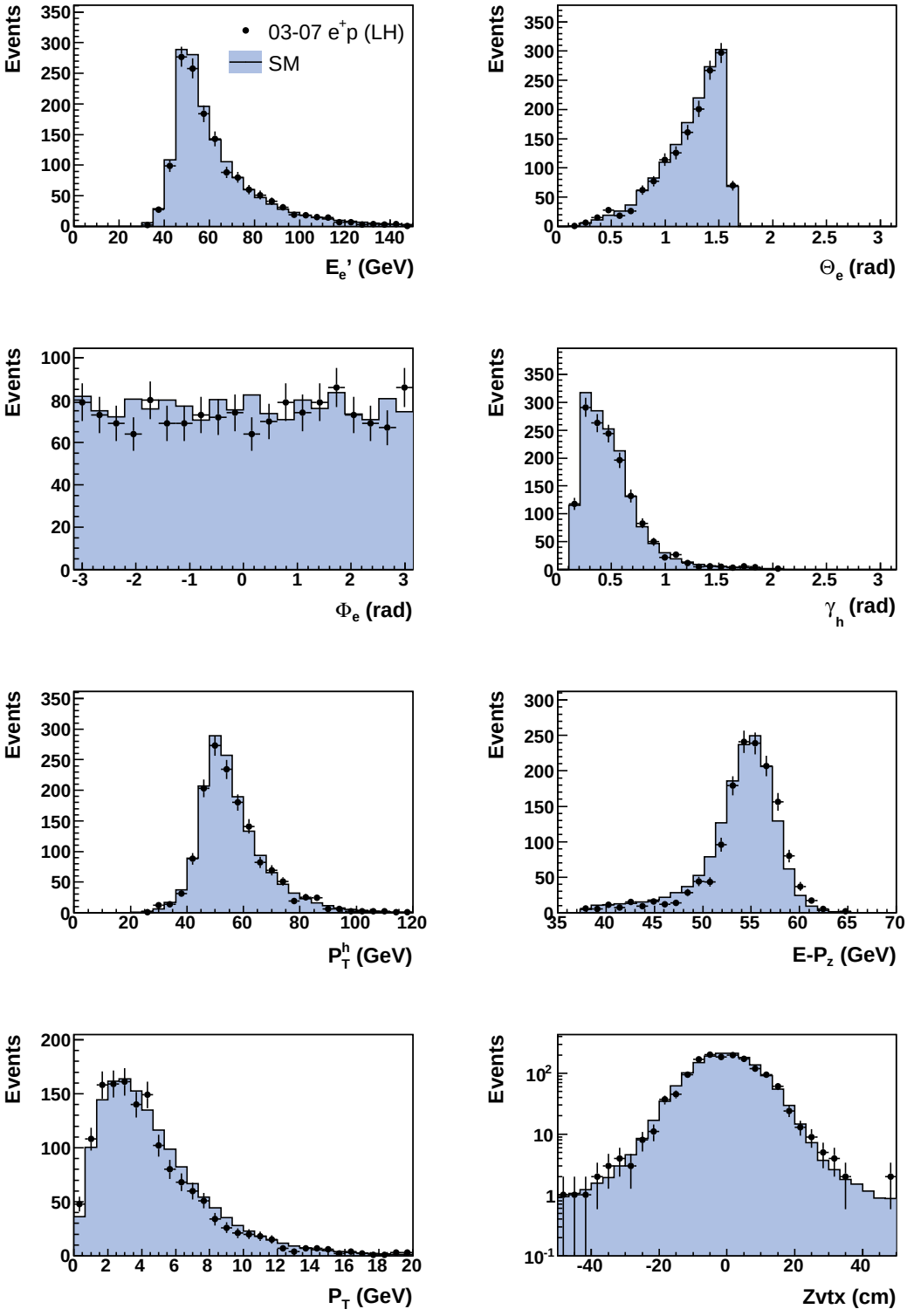

Figure A.7: *Electron, hadronic, and global variables for left-handed positron data after all selection cuts. The dots are the data and the histograms show the luminosity normalized Standard Model expectation.*

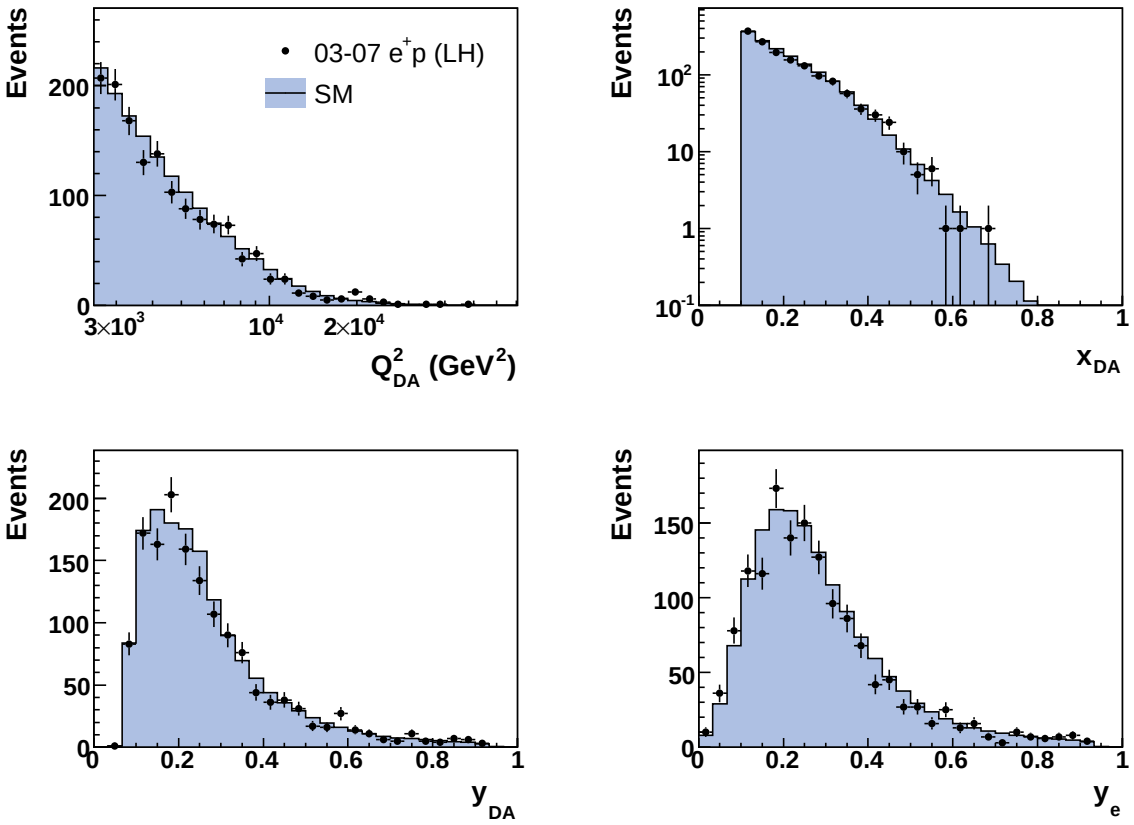

Figure A.8: *Kinematic variables for left-handed positron data after all selection cuts. The dots are the data and the histograms show the luminosity normalized Standard Model expectation.*

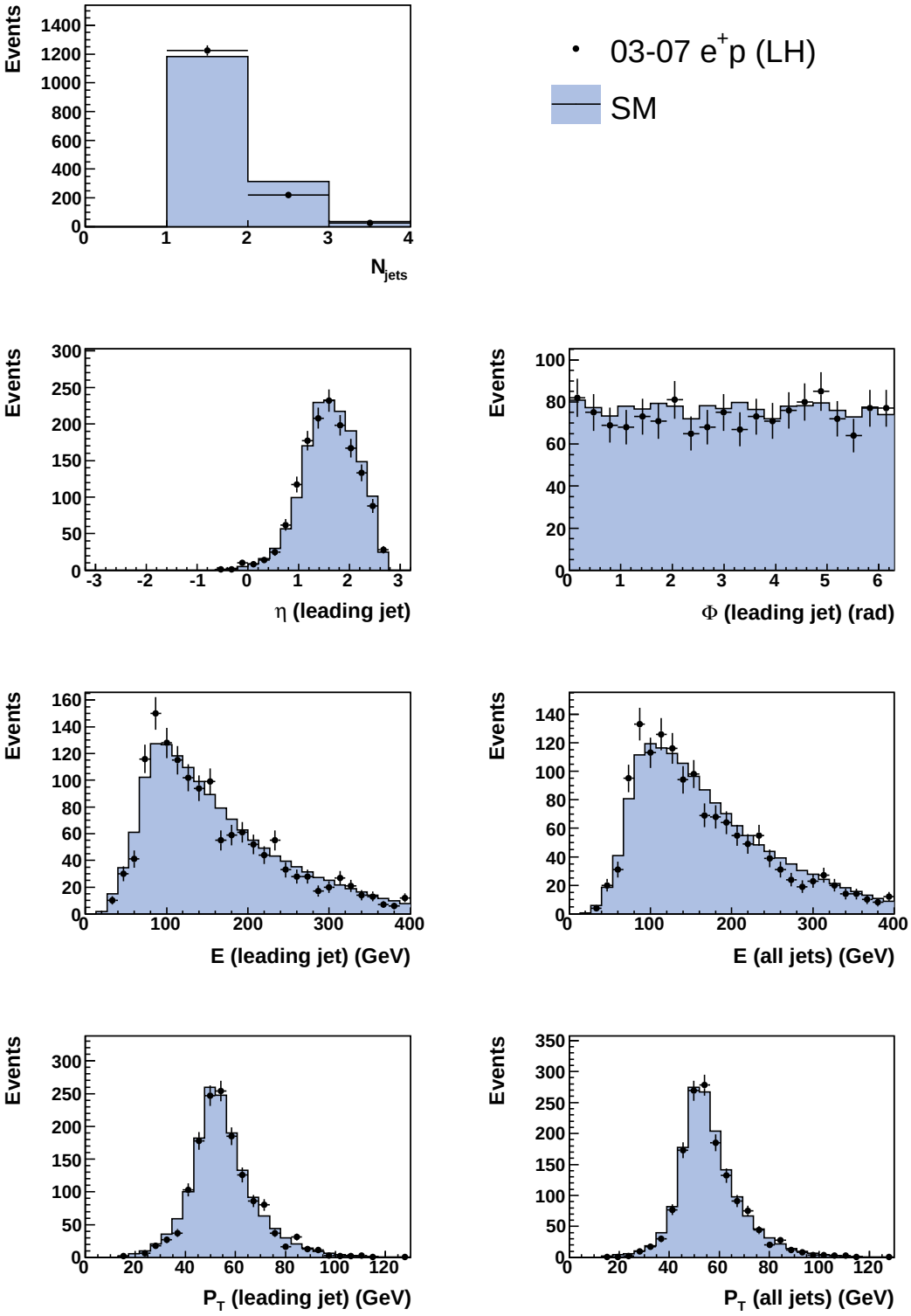

Figure A.9: *Jet variables for left-handed positron data after all selection cuts. The dots are the data and the histograms show the luminosity normalized Standard Model expectation.*

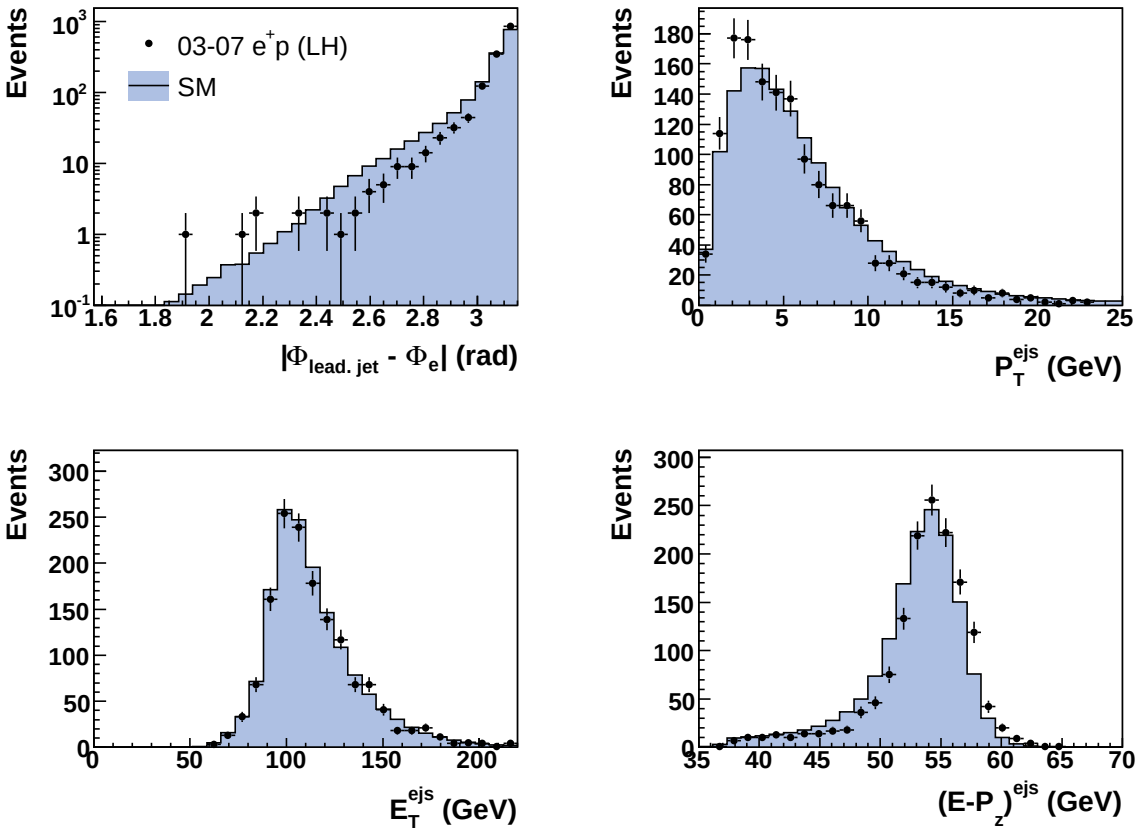

Figure A.10: *Variables from electron and jet information for left-handed positron data after all selection cuts. The dots are the data and the histograms show the luminosity normalized Standard Model expectation.*

A.3 Right-handed Positron Data

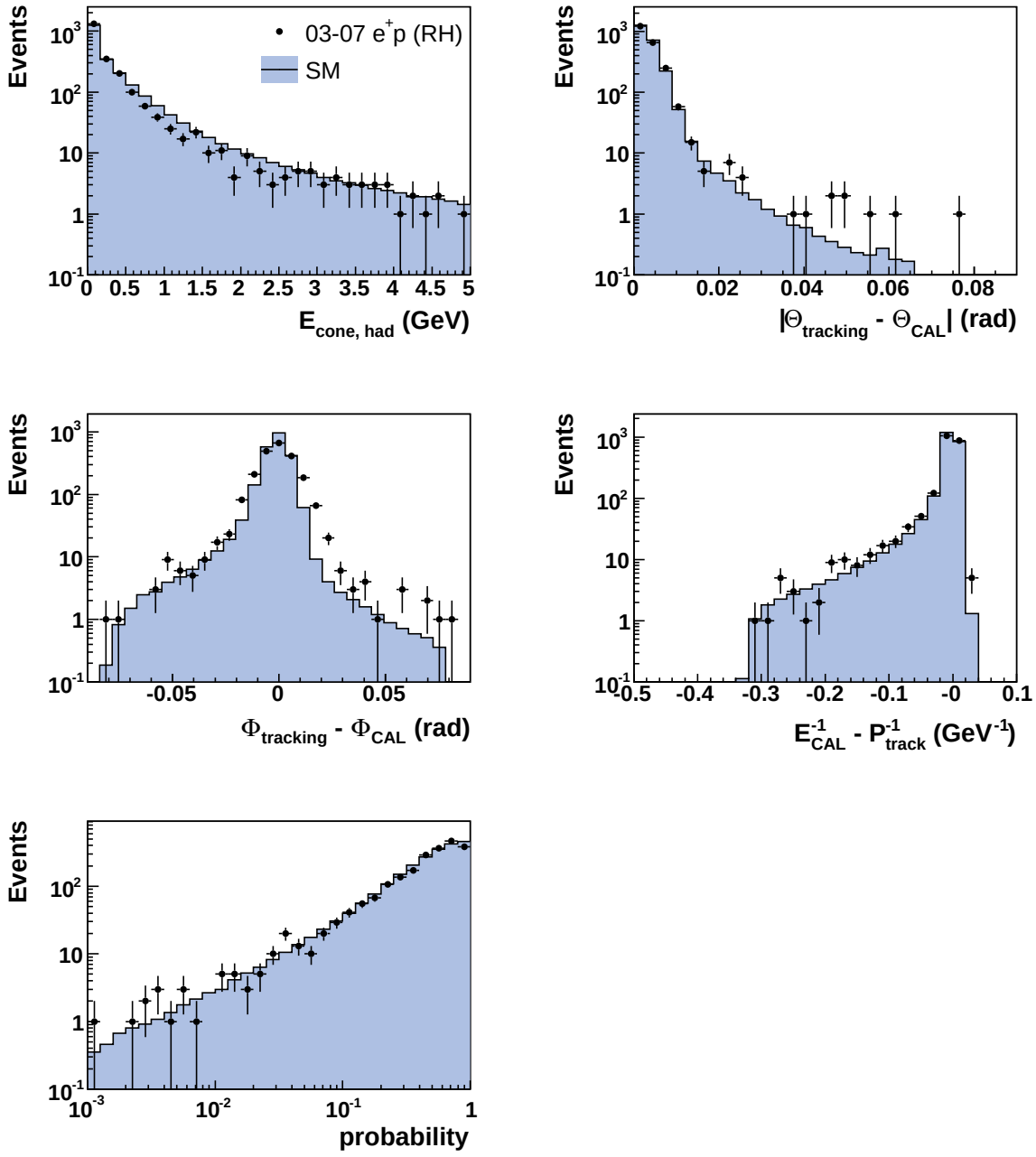

Figure A.11: *Variables used by the EM finder for the evaluation of the electron probability, and the electron probability itself, shown for right-handed positron data after all selection cuts. The dots are the data and the histograms show the luminosity normalized Standard Model expectation.*

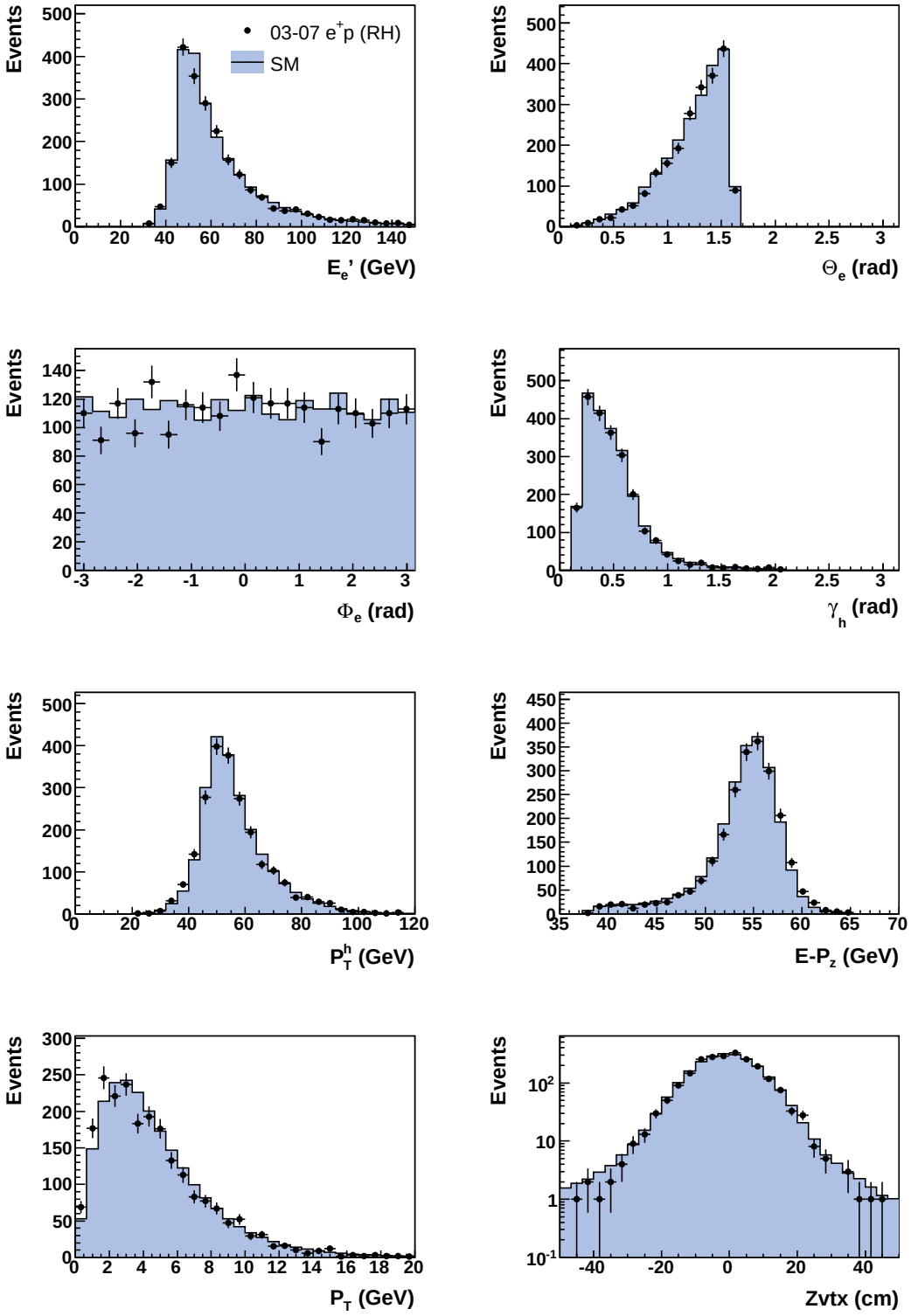

Figure A.12: *Electron, hadronic, and global variables for right-handed positron data after all selection cuts. The dots are the data and the histograms show the luminosity normalized Standard Model expectation.*

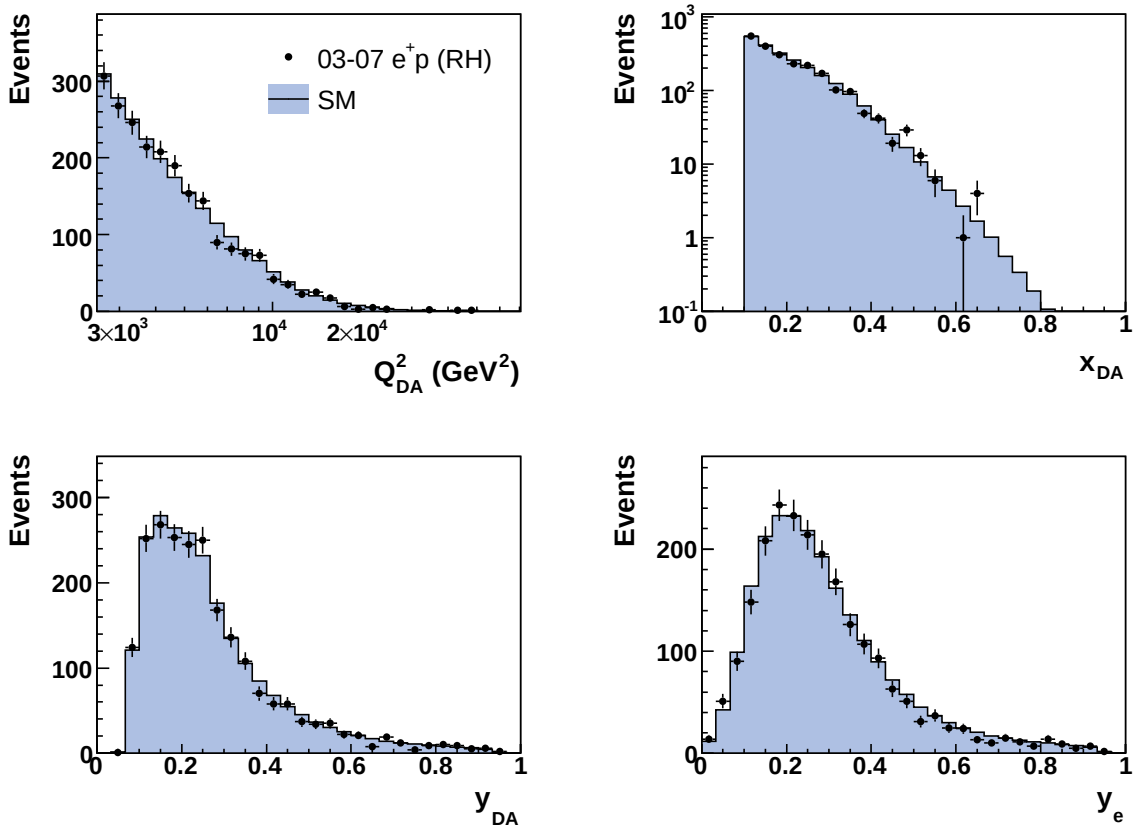

Figure A.13: *Kinematic variables for right-handed positron data after all selection cuts. The dots are the data and the histograms show the luminosity normalized Standard Model expectation.*

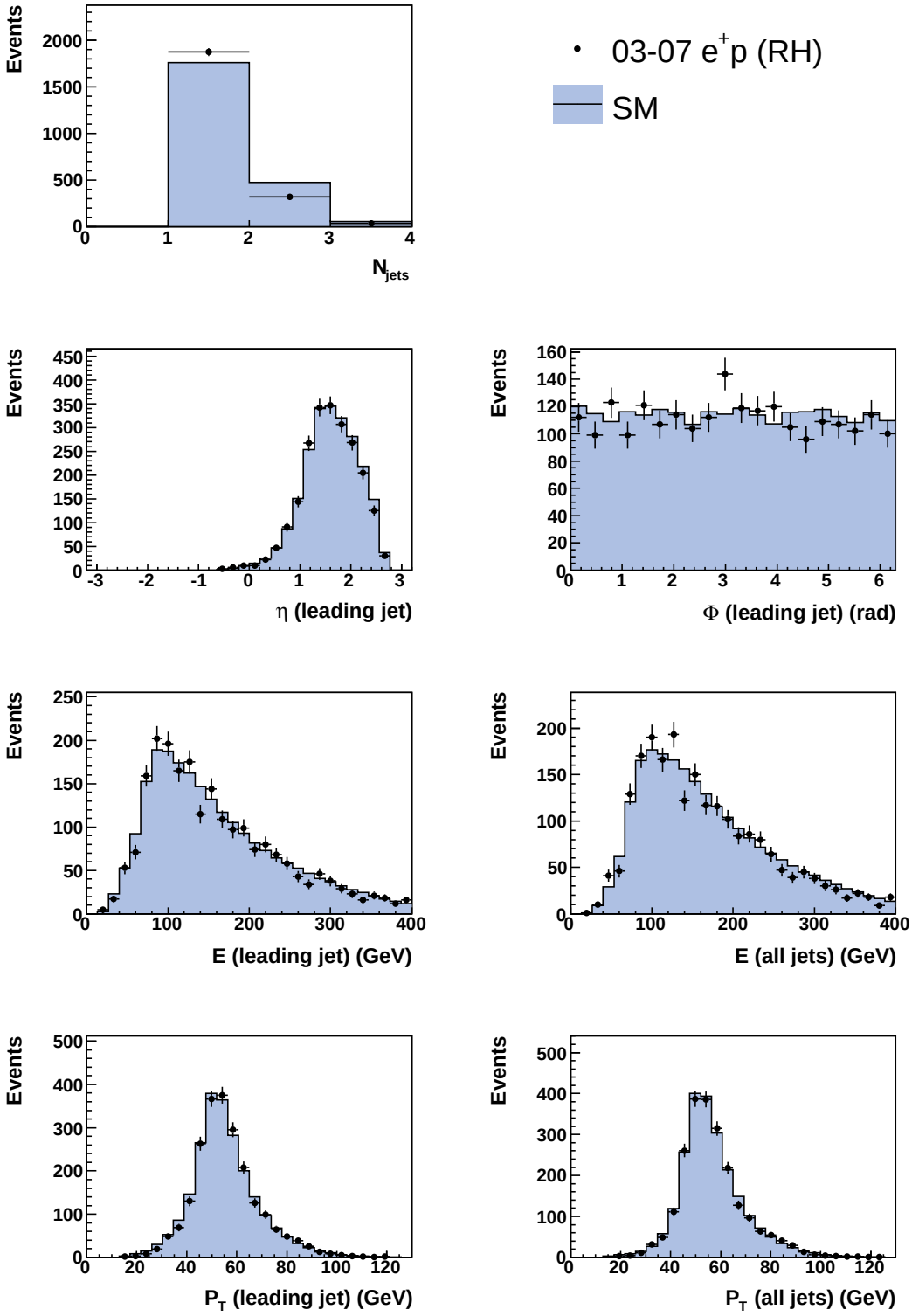

Figure A.14: *Jet variables for right-handed positron data after all selection cuts. The dots are the data and the histograms show the luminosity normalized Standard Model expectation.*

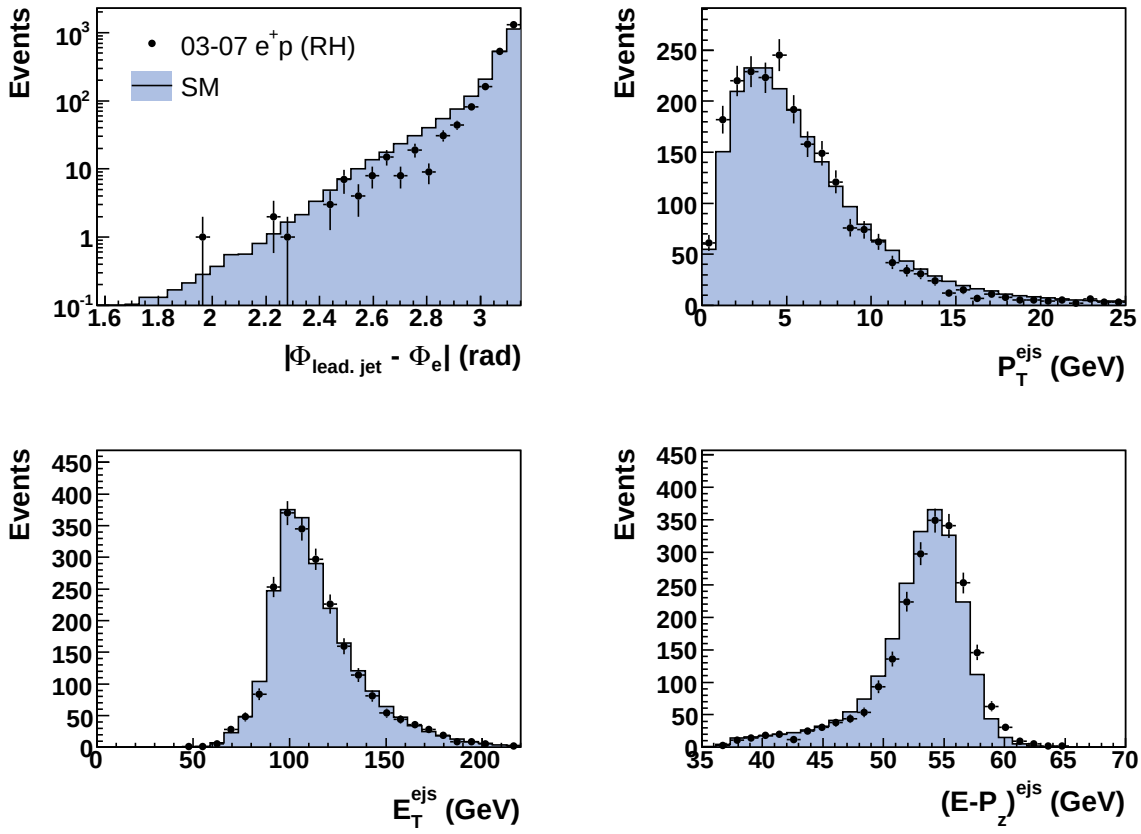

Figure A.15: *Variables from electron and jet information for right-handed positron data after all selection cuts. The dots are the data and the histograms show the luminosity normalized Standard Model expectation.*

Appendix B

Control Distributions for Charged Current

In this chapter, the CC control distributions for positron data and right-handed electron data are shown. The control distributions for left-handed electron data can be found in Sections 4.7.3 and 4.7.5.

B.1 Right-handed Electron Data

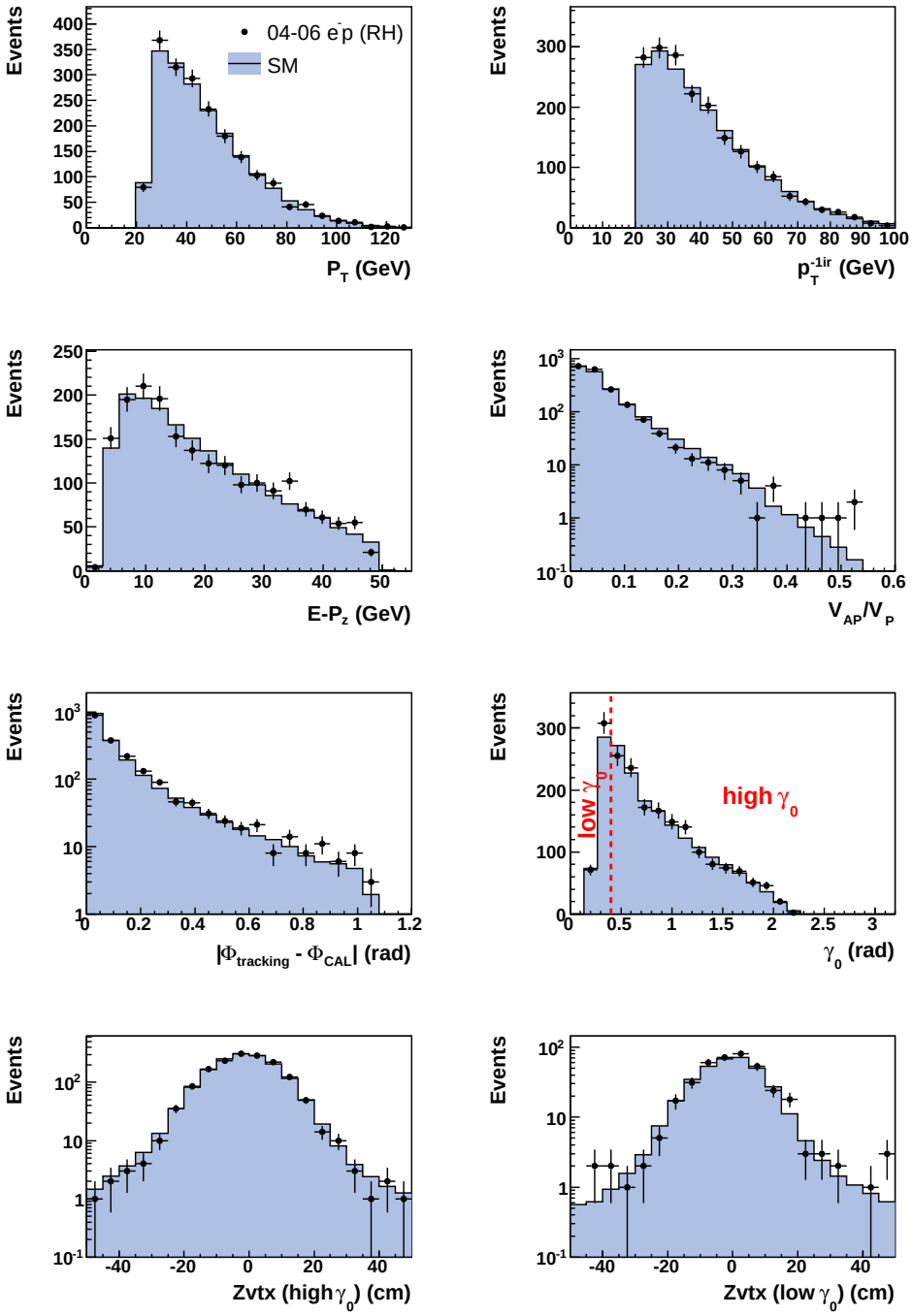

Figure B.1: *Global variables for right-handed electron data after all selection cuts. The dots are the data and the histograms show the luminosity normalized Standard Model expectation.*

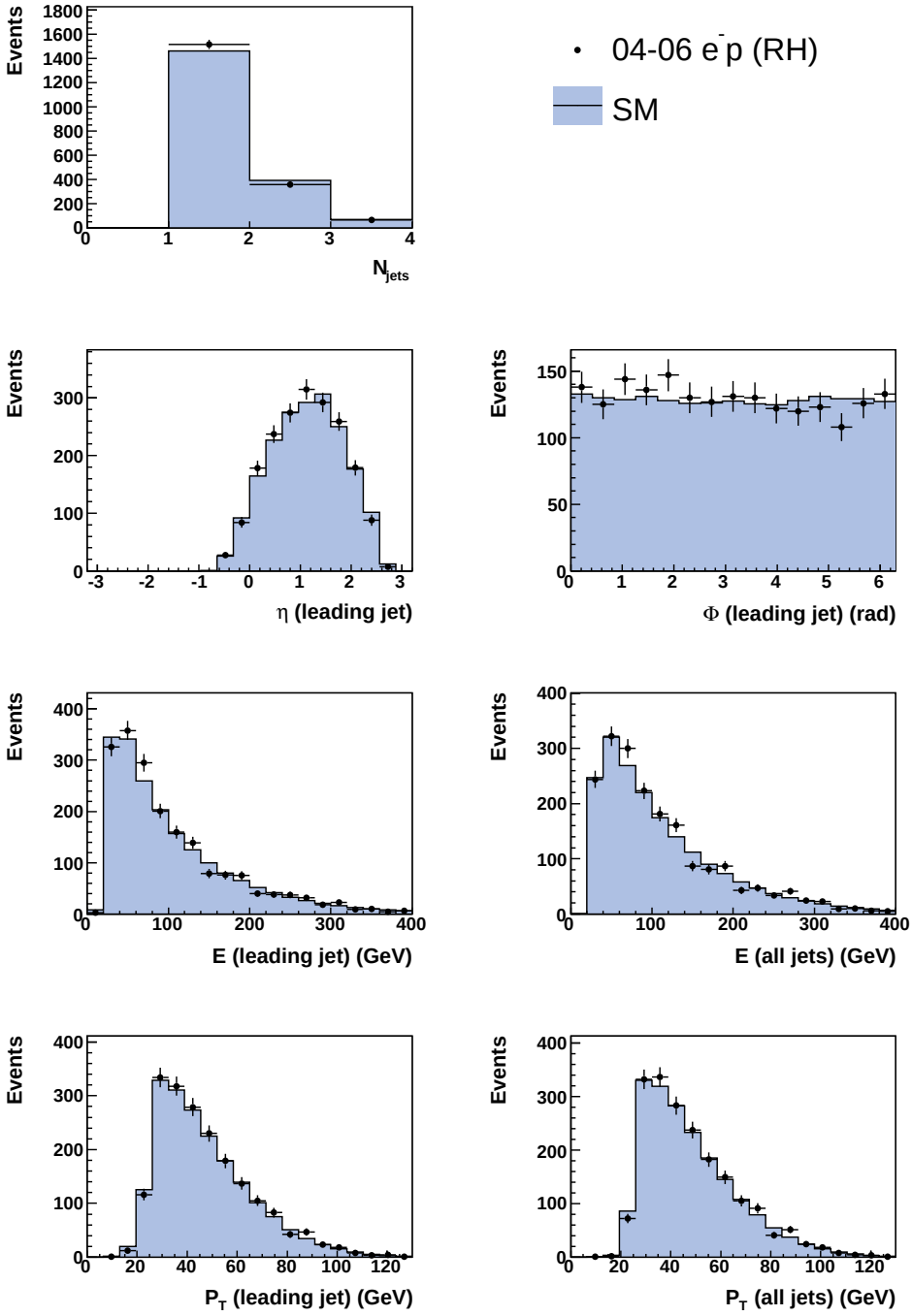

Figure B.2: *Jet variables for right-handed electron data after all selection cuts. The dots are the data and the histograms show the luminosity normalized Standard Model expectation.*

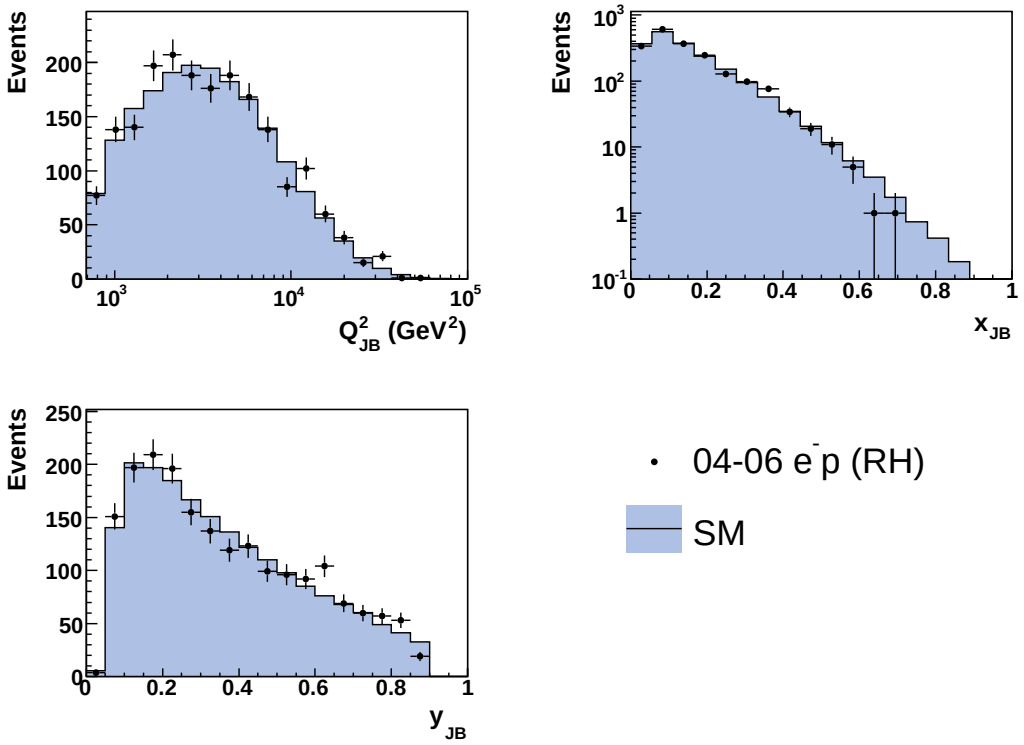

Figure B.3: *Kinematic variables for right-handed electron data after all selection cuts. The dots are the data and the histograms show the luminosity normalized Standard Model expectation.*

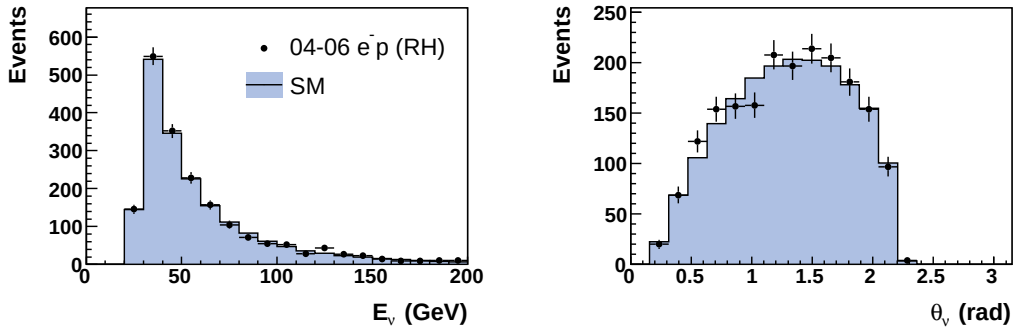

Figure B.4: *Neutrino variables for right-handed electron data after all selection cuts. The dots are the data and the histograms show the luminosity normalized Standard Model expectation.*

B.2 Left-handed Positron Data

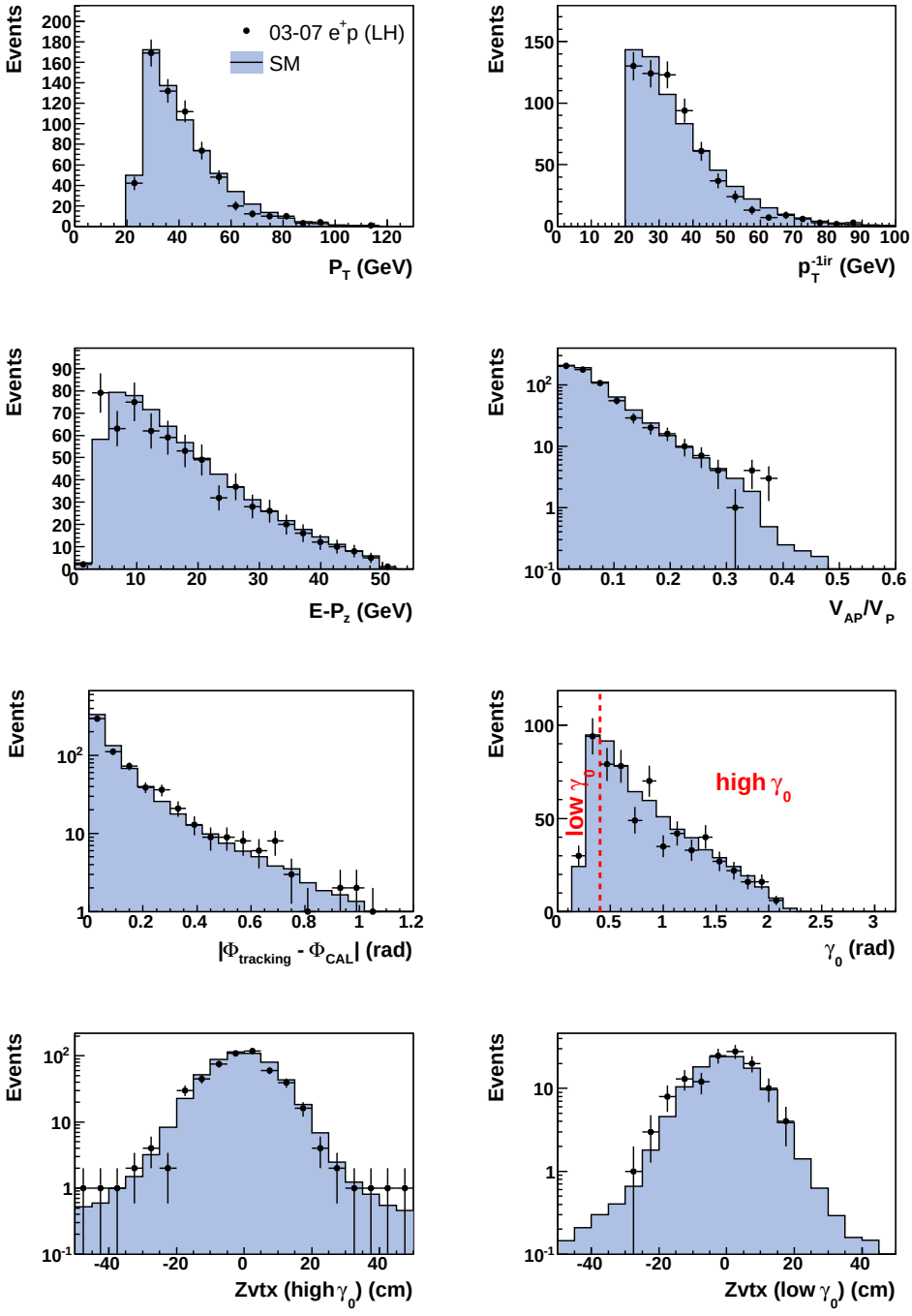

Figure B.5: *Global variables for left-handed positron data after all selection cuts. The dots are the data and the histograms show the luminosity normalized Standard Model expectation.*

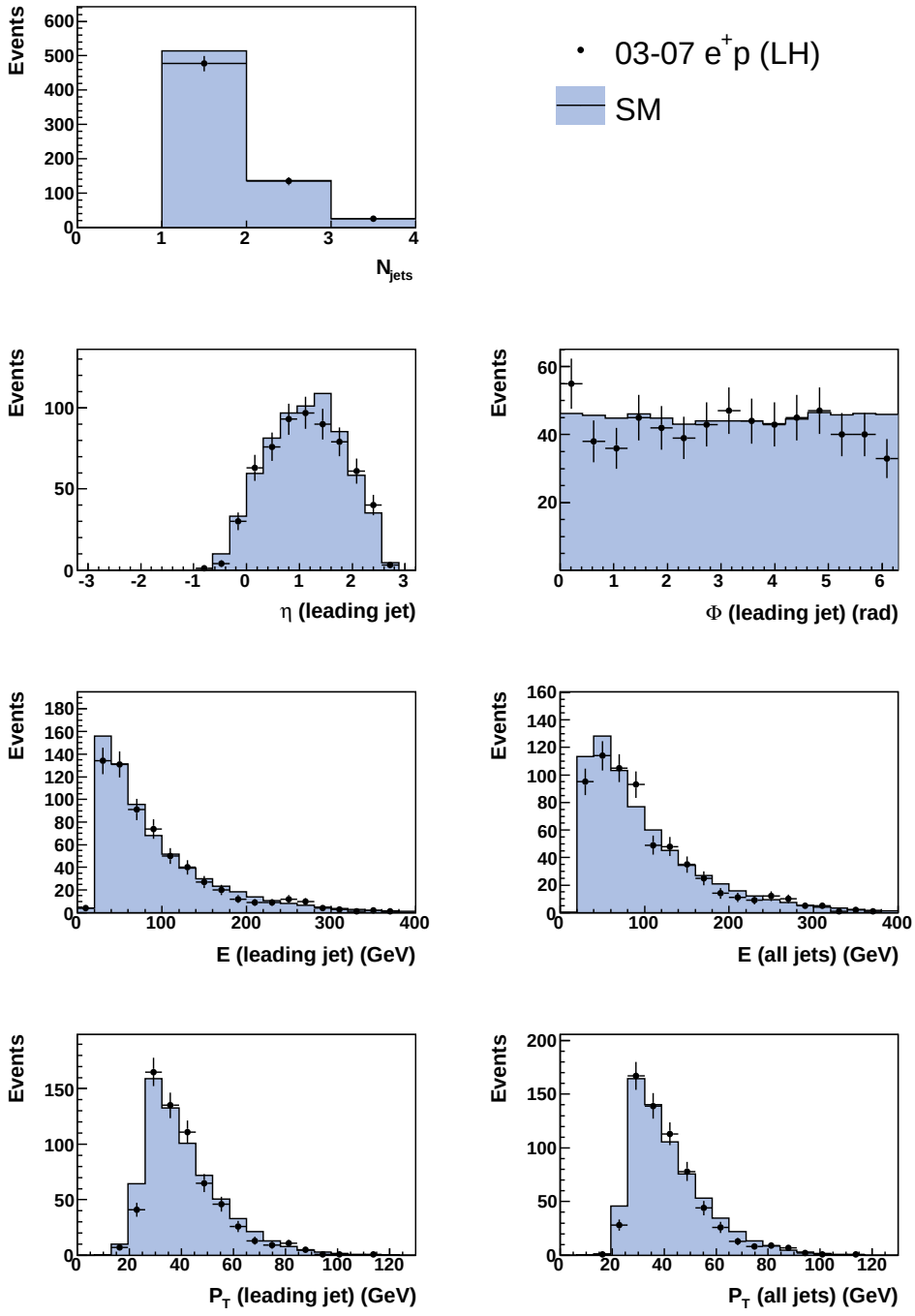

Figure B.6: *Jet variables for left-handed positron data after all selection cuts. The dots are the data and the histograms show the luminosity normalized Standard Model expectation.*

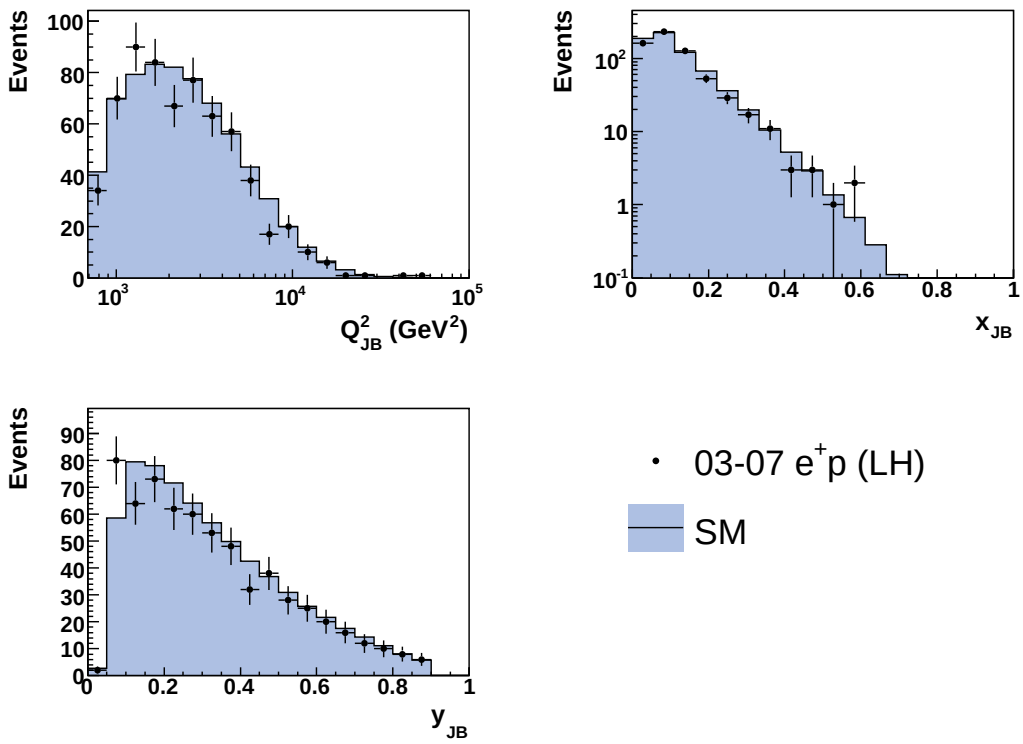

Figure B.7: *Kinematic variables for left-handed positron data after all selection cuts. The dots are the data and the histograms show the luminosity normalized Standard Model expectation.*

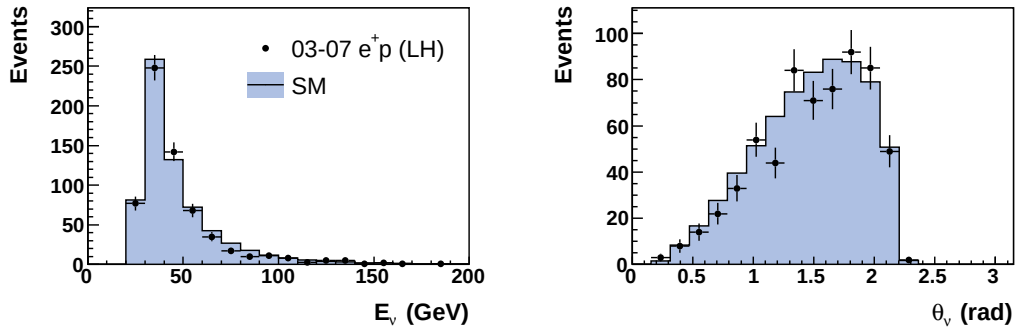

Figure B.8: *Neutrino variables for left-handed positron data after all selection cuts. The dots are the data and the histograms show the luminosity normalized Standard Model expectation.*

B.3 Right-handed Positron Data

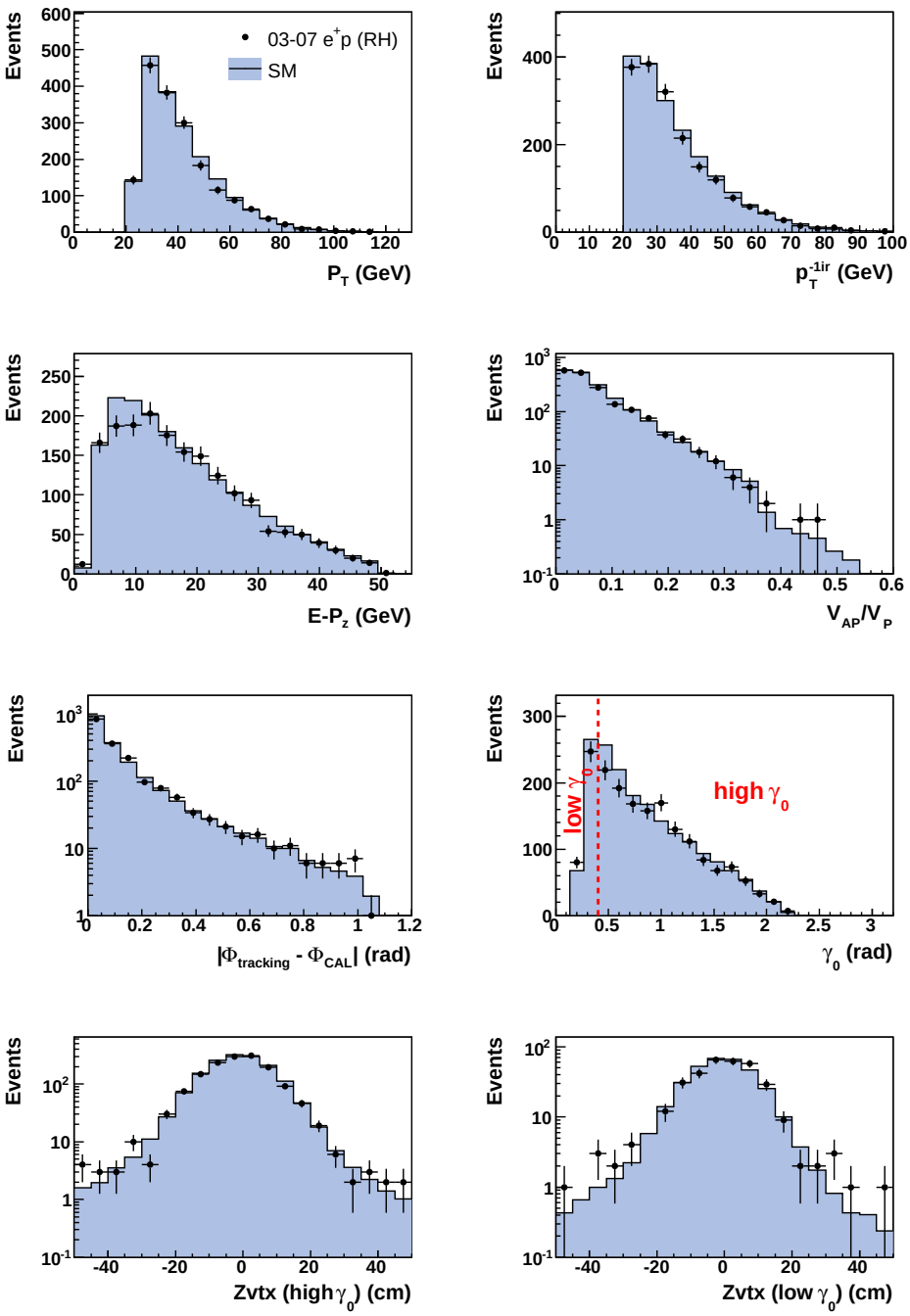

Figure B.9: *Global variables for right-handed positron data after all selection cuts. The dots are the data and the histograms show the luminosity normalized Standard Model expectation.*

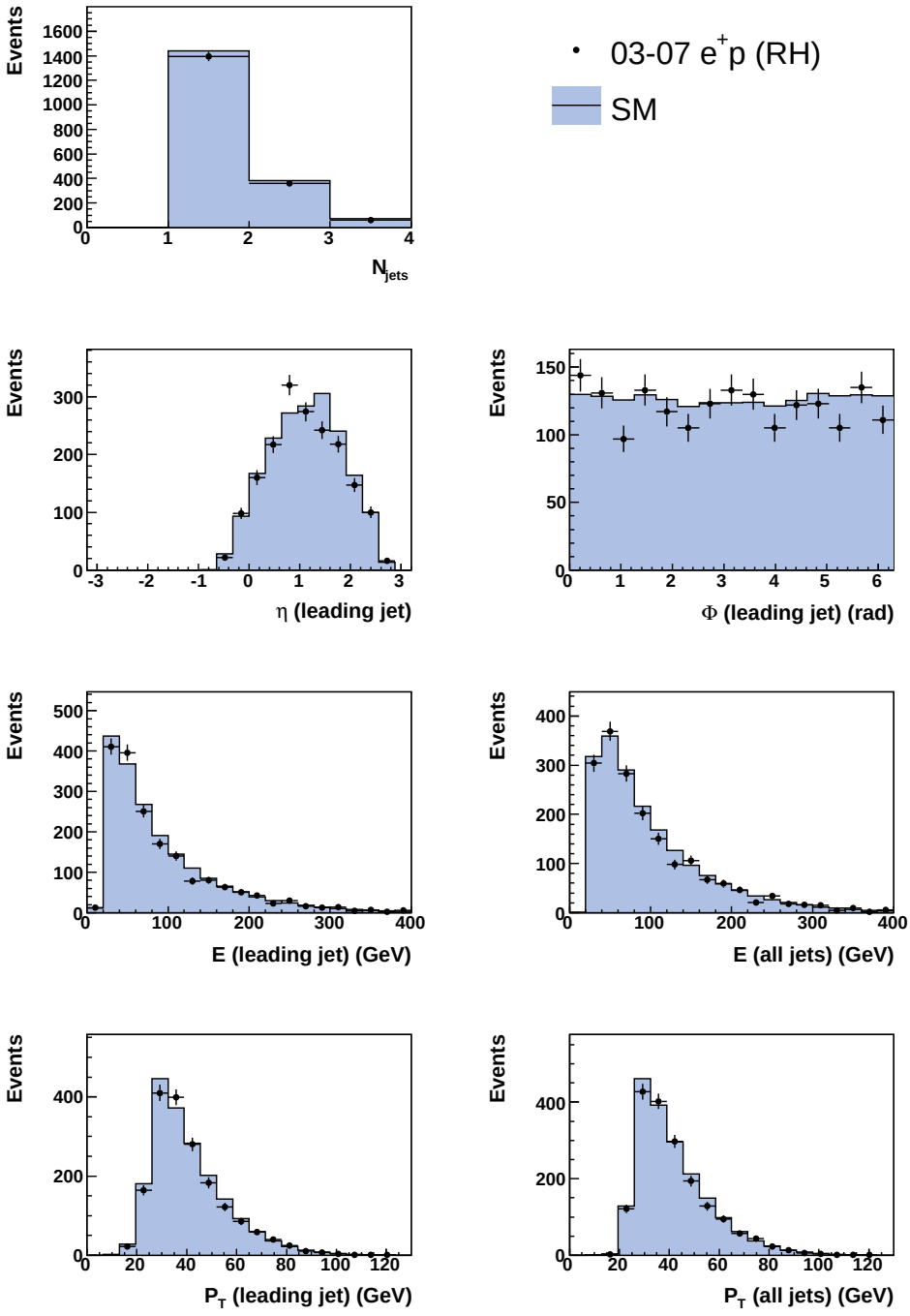

Figure B.10: *Jet variables for right-handed positron data after all selection cuts. The dots are the data and the histograms show the luminosity normalized Standard Model expectation.*

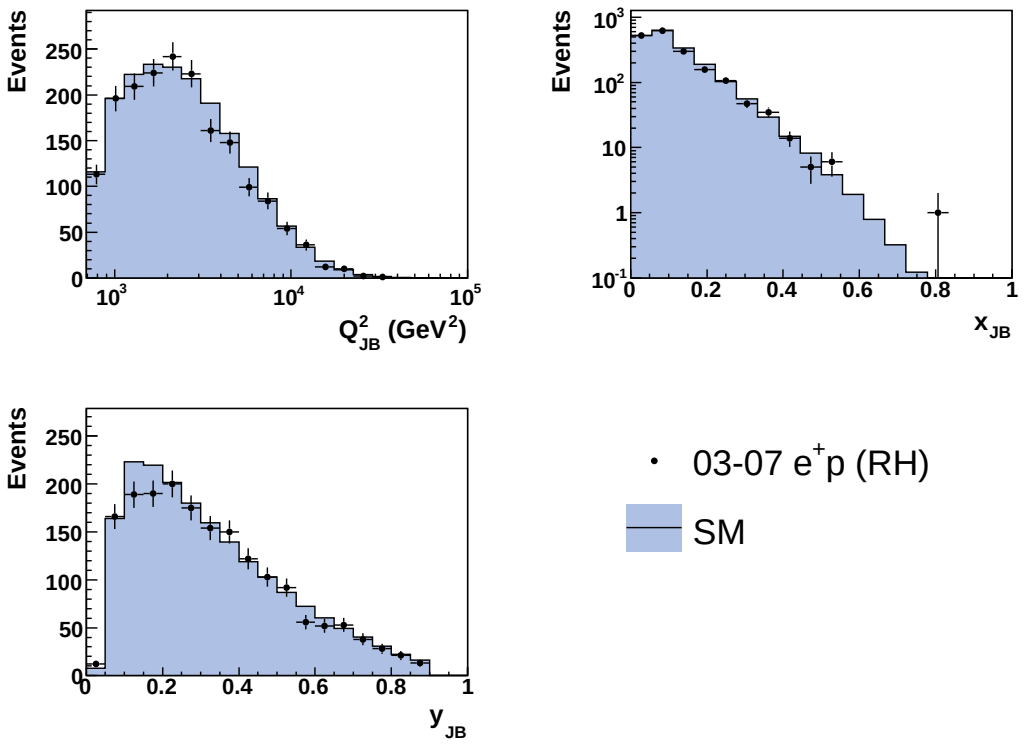

Figure B.11: *Kinematic variables for right-handed positron data after all selection cuts. The dots are the data and the histograms show the luminosity normalized Standard Model expectation.*

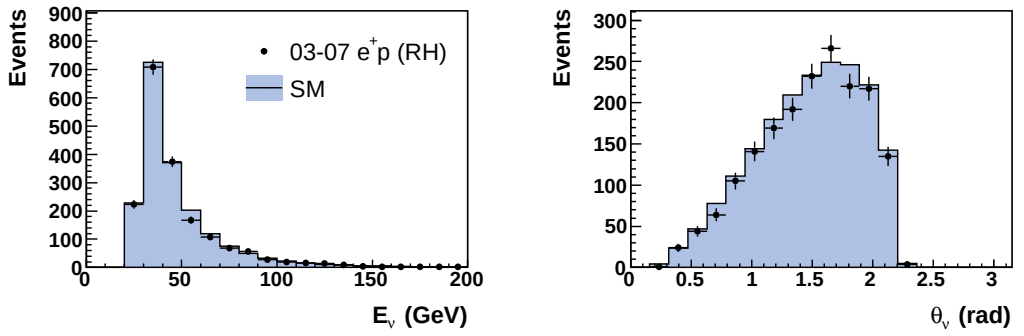

Figure B.12: *Neutrino variables for right-handed positron data after all selection cuts. The dots are the data and the histograms show the luminosity normalized Standard Model expectation.*

Appendix C

Timing Cut for CC Data Events

The CAL time for each calorimeter cell is defined relative to the expected time of an energy deposit in an *ep* interaction occuring at the nominal interaction point. Data events in the CC analysis are required to fulfill the following conditions:

$$
\begin{aligned}
|t_{\mathrm{F}}| < 6\,\mathrm{ns} \vee E_{\mathrm{F}} \leq 0.6\,\mathrm{GeV} \vee n_{\mathrm{F}} < 2 \vee t_{\mathrm{F}} = -100\,\mathrm{ns},\\
(t_{\mathrm{F}} > -5\,\mathrm{ns} \wedge t_{\mathrm{F}} < 4\,\mathrm{ns}) \vee E_{\mathrm{F}} \leq 3\,\mathrm{GeV} \vee n_{\mathrm{F}} < 2 \vee t_{\mathrm{F}} = -100\,\mathrm{ns},\\
|t_{\mathrm{B}}| < 6\,\mathrm{ns} \vee E_{\mathrm{B}} \leq 2\,\mathrm{GeV} \vee n_{\mathrm{B}} < 2 \vee t_{\mathrm{B}} = -100\,\mathrm{ns},\\
(t_{\mathrm{B}} > -4\,\mathrm{ns} \wedge t_{\mathrm{B}} < 5\,\mathrm{ns}) \vee E_{\mathrm{B}} \leq 4\,\mathrm{GeV} \vee n_{\mathrm{B}} < 2 \vee t_{\mathrm{B}} = -100\,\mathrm{ns},\\
|t_{\mathrm{R}}| < 6\,\mathrm{ns} \vee E_{\mathrm{R}} \leq 2\,\mathrm{GeV} \vee n_{\mathrm{R}} < 2 \vee t_{\mathrm{R}} = -100\,\mathrm{ns},\\
|t_{\mathrm{R}}| < 5\,\mathrm{ns} \vee E_{\mathrm{R}} \leq 4\,\mathrm{GeV} \vee n_{\mathrm{R}} < 2 \vee t_{\mathrm{R}} = -100\,\mathrm{ns},\\
(t_{\mathrm{g}} > -5\,\mathrm{ns} \wedge t_{\mathrm{g}} < 4\,\mathrm{ns}) \vee E_{\mathrm{g}} \leq 0.6\,\mathrm{GeV} \vee n_{\mathrm{g}} < 2 \vee t_{\mathrm{g}} = -100\,\mathrm{ns},\\
(t_{\mathrm{u}} > -5\,\mathrm{ns} \wedge t_{\mathrm{u}} < 5\,\mathrm{ns}) \vee E_{\mathrm{u}} \leq 3\,\mathrm{GeV} \vee n_{\mathrm{u}} < 2 \vee t_{\mathrm{u}} = -100\,\mathrm{ns},\\
(t_{\mathrm{d}} > -7\,\mathrm{ns} \wedge t_{\mathrm{d}} < 5\,\mathrm{ns}) \vee E_{\mathrm{d}} \leq 4\,\mathrm{GeV} \vee n_{\mathrm{d}} < 2 \vee t_{\mathrm{d}} = -100\,\mathrm{ns},\\
\big((t_{\mathrm{F}} - t_{\mathrm{R}}) > -8\,\mathrm{ns} \wedge (t_{\mathrm{F}} - t_{\mathrm{R}}) < 4\,\mathrm{ns}\big) \vee E_{\mathrm{F}} \leq 2\,\mathrm{GeV} \vee E_{\mathrm{R}} \leq 2\,\mathrm{GeV}\\
\vee n_{\mathrm{F}} < 2 \vee n_{\mathrm{R}} < 2 \vee t_{\mathrm{F}} = -100\,\mathrm{ns} \vee t_{\mathrm{R}} = -100\,\mathrm{ns},\\
\big((t_{\mathrm{u}} - t_{\mathrm{d}}) > -7\,\mathrm{ns} \wedge (t_{\mathrm{u}} - t_{\mathrm{d}}) < 6\,\mathrm{ns}\big) \vee E_{\mathrm{u}} \leq 3\,\mathrm{GeV} \vee E_{\mathrm{d}} \leq 3\,\mathrm{GeV}\\
\vee n_{\mathrm{u}} < 2 \vee n_{\mathrm{d}} < 2 \vee t_{\mathrm{u}} = -100\,\mathrm{ns} \vee t_{\mathrm{d}} = -100\,\mathrm{ns}.
\end{aligned}
$$

Here, t_F, t_B and t_R are the average times of the energy deposits in the FCAL, BCAL or RCAL cells; t_g, t_u and t_d are the average times of the energy deposits in the whole calorimeter and in the upper and lower half of the calorimeter, respectively. n_i $(i = F, B, R, g, u, d)$ is the number of photomultipliers that measured an energy deposit above the noise threshold (each cell is read out by two photomultiplier, Section 3.2.3), E_i is the energy sum of

the photomultipliers. A time of -100 ns means that none of the photomultipliers of the considered calorimeter part measured an energy deposit above the noise threshold.

Bibliography

[1] S. L. Glashow, "Partial Symmetries of Weak Interactions," *Nucl. Phys.* **22** (1961) 579–588.

A. Salam, "Fundamental Theory of Matter: a Survey of Results and Methods,". International symposium on contemporary physics 7-28 Jun 1968, Trieste, Italy.

S. Weinberg, "A Model of Leptons," *Phys. Rev. Lett.* **19** (1967) 1264–1266.

M. Gell-Mann, "A Schematic Model of Baryons and Mesons," *Phys. Lett.* **8** (1964) 214–215.

H. Fritzsch, M. Gell-Mann, and H. Leutwyler, "Advantages of the Color Octet Gluon Picture," *Phys. Lett.* **B47** (1973) 365–368.

[2] **Particle Data Group** Collaboration, C. Amsler *et al.*, "Review of particle physics," *Phys. Lett.* **B667** (2008) 1. and references therein.

[3] W. Buchmüller, R. Rückl, and D. Wyler, "Leptoquarks in lepton quark collisions," *Phys. Lett.* **B191** (1987) 442–448. [Erratum-ibid. **B448** (1999) 320].

[4] R. P. Feynman, "Very High-Energy Collisions of Hadrons," *Phys. Rev. Lett.* **23** (1969) 1415–1417.

J. D. Bjorken and E. A. Paschos, "Inelastic Electron Proton and gamma Proton Scattering, and the Structure of the Nucleon," *Phys. Rev.* **185** (1969) 1975–1982.

[5] R. Devenish and A. Cooper-Sarker, *Deep Inelastic Scattering*. Oxford University Press, 2003.

[6] **ZEUS** Collaboration, S. Chekanov *et al.*, "Measurement of high-Q**2 e- p neutral current cross sections at HERA and the extraction of xF3," *Eur. Phys. J.* **C28** (2003) 175, `hep-ex/0208040`.

ZEUS Collaboration, S. Chekanov *et al.*, "High-Q**2 neutral current cross sections in e+ p deep inelastic scattering at s**(1/2) = 318-GeV," *Phys. Rev.* **D70** (2004) 052001, hep-ex/0401003.

ZEUS Collaboration, S. Chekanov *et al.*, "Measurement of high-Q**2 charged current cross sections in e+ p deep inelastic scattering at HERA," *Eur. Phys. J.* **C32** (2003) 1–16, hep-ex/0307043.

H1 Collaboration, C. Adloff *et al.*, "Measurement of neutral and charged current cross-sections in positron proton collisions at large momentum transfer," *Eur. Phys. J.* **C13** (2000) 609–639, hep-ex/9908059.

H1 Collaboration, C. Adloff *et al.*, "Measurement of neutral and charged current cross-sections in electron - proton collisions at high Q^2," *Eur. Phys. J.* **C19** (2001) 269–288, hep-ex/0012052.

S. Kretzer, H. L. Lai, F. I. Olness, and W. K. Tung, "CTEQ6 parton distributions with heavy quark mass effects," *Phys. Rev.* **D69** (2004) 114005, hep-ph/0307022.

[7] **ZEUS** Collaboration, S. Chekanov *et al.*, "Measurement of high-Q**2 charged current cross sections in e- p deep inelastic scattering at HERA," *Phys. Lett.* **B539** (2002) 197–217, hep-ex/0205091. [Erratum-ibid. **B552** (2003) 308].

[8] "Compiled H1+ZEUS NC and CC plots for conferences," ZEUS-prel-09-001.

[9] **ZEUS** Collaboration, S. Chekanov *et al.*, "Measurement of high-Q^2 neutral current deep inelastic $e^- p$ scattering cross sections with a longitudinally polarised electron beam at HERA," *Eur. Phys. J.* **C62** (2009) 625–658, 0901.2385.

[10] **ZEUS** Collaboration, S. Chekanov *et al.*, "Measurement of charged current deep inelastic scattering cross sections with a longitudinally polarised electron beam at HERA," *Eur. Phys. J.* **C61** (2009) 223–235, 0812.4620.

[11] H. Georgi and S. L. Glashow, "Unity of All Elementary Particle Forces," *Phys. Rev. Lett.* **32** (1974) 438–441.

[12] J. C. Pati and A. Salam, "Lepton Number as the Fourth Color," *Phys. Rev.* **D10** (1974) 275–289.

[13] S. Dimopoulos, S. Raby, and F. Wilczek, "Supersymmetry and the Scale of Unification," *Phys. Rev.* **D24** (1981) 1681–1683.

[14] I. Dorsner and P. Fileviez Perez, "Unification without supersymmetry: Neutrino mass, proton decay and light leptoquarks," *Nucl. Phys.* **B723** (2005) 53–76, hep-ph/0504276.

I. Dorsner, P. Fileviez Perez, and R. Gonzalez Felipe, "Phenomenological and cosmological aspects of a minimal GUT scenario," *Nucl. Phys.* **B747** (2006) 312–327, hep-ph/0512068.

[15] O. U. Shanker, "Flavor Violation, Scalar Particles and Leptoquarks," *Nucl. Phys.* **B206** (1982) 253.

[16] W. Buchmüller and D. Wyler, "Constraints on SU(5) Type Leptoquarks," *Phys. Lett.* **B177** (1986) 377.

[17] A. Djouadi, T. Köhler, M. Spira, and J. Tutas, "(e b), (e t) Type Leptoquark at *ep* Colliders," *Z. Phys.* **C46** (1990) 679–686.

[18] M. Krämer, T. Plehn, M. Spira, and P. M. Zerwas, "Pair production of scalar leptoquarks at the Tevatron," *Phys. Rev. Lett.* **79** (1997) 341–344, hep-ph/9704322.

J. Blümlein, E. Boos, and A. Kryukov, "Leptoquark pair production in hadronic interactions," *Z. Phys.* **C76** (1997) 137–153, hep-ph/9610408.

[19] J. L. Hewett and T. G. Rizzo, "Much ado about leptoquarks: A Comprehensive analysis," *Phys. Rev.* **D56** (1997) 5709–5724, hep-ph/9703337.

[20] D. E. Acosta and S. K. Blessing, "Leptoquark searches at HERA and the Tevatron," *Ann. Rev. Nucl. Part. Sci.* **49** (1999) 389–434.

[21] J. Kalinowski, R. Rückl, H. Spiesberger, and P. M. Zerwas, "Leptoquark/squark interpretation of HERA events: Virtual effects in e+ e- annihilation to hadrons," *Z. Phys.* **C74** (1997) 595–603, hep-ph/9703288.

[22] V. D. Barger, K.-m. Cheung, K. Hagiwara, and D. Zeppenfeld, "Global Study of Electron Quark Contact Interactions," *Phys. Rev.* **D57** (1998) 391–404, hep-ph/9707412.

D. Zeppenfeld and K.-m. Cheung, "New Interactions in Neutral Current Processes," hep-ph/9810277.

[23] H. P. Nilles, "Supersymmetry, Supergravity and Particle Physics," *Phys. Rept.* **110** (1984) 1–162.

H. E. Haber and G. L. Kane, "The Search for Supersymmetry: Probing Physics Beyond the Standard Model," *Phys. Rept.* **117** (1985) 75–263.

I. J. R. Aitchison, "Supersymmetry and the MSSM: An elementary introduction," `hep-ph/0505105`.

[24] R. Barbier *et al.*, "R-parity violating supersymmetry," *Phys. Rept.* **420** (2005) 1–202, `hep-ph/0406039`.

[25] J. Butterworth and H. K. Dreiner, "R-parity violation at HERA," *Nucl. Phys.* **B397** (1993) 3–34, `hep-ph/9211204`.

[26] A. Kwiatkowski, H. Spiesberger, and H. J. Möhring, "HERACLES: An Event Generator for *ep* Interactions at HERA Energies Including Radiative Processes: VERSION 1.0," *Comp. Phys. Commun.* **69** (1992) 155–172.

[27] H. Spiesberger, HERACLES *and* DJANGOH*: Event Generation of ep Interactions at HERA Including Radiative Processes*, 2005. Available on `wwwthep.physik.uni-mainz.de/~hspiesb/djangoh/djangoh.html`.

[28] K. Charchula, G. A. Schuler, and H. Spiesberger, "Combined QED and QCD Radiative Effects in Deep Inelastic Lepton - Proton Scattering: The Monte Carlo Generator DJANGO6," *Comput. Phys. Commun.* **81** (1994) 381–402.

[29] **CTEQ** Collaboration, H. L. Lai *et al.*, "Global QCD Analysis of Parton Structure of the Nucleon: CTEQ5 Parton Distributions," *Eur. Phys. J.* **C12** (2000) 375–392.

[30] L. Lönnblad, "ARIADNE version 4: A Program for simulation of QCD cascades implementing the color dipole model," *Comput. Phys. Commun.* **71** (1992) 15–31.

[31] T. Sjöstrand, "The Lund Monte Carlo for Jet Fragmentation and e+ e- Physics: Jetset Version 6.2," *Comput. Phys. Commun.* **39** (1986) 347–407.

T. Sjöstrand and M. Bengtsson, "The Lund Monte Carlo for Jet Fragmentation and e+ e- Physics. Jetset Version 6.3: An Update," *Comput. Phys. Commun.* **43** (1987) 367.

T. Sjöstrand, "High-energy physics event generation with PYTHIA 5.7 and JETSET 7.4," *Comput. Phys. Commun.* **82** (1994) 74–90.

[32] A. Arbuzov, D. Y. Bardin, J. Blümlein, L. Kalinovskaya, and T. Riemann, "HECTOR 1.00 - A program for the calculation of QED, QCD and electroweak corrections to ep and lN deep inelastic neutral and charged current scattering," *Comput. Phys. Commun.* **94** (1996) 128–184, `hep-ph/9511434`.

[33] T. Sjöstrand *et al.*, "High-energy physics event generation with PYTHIA 6.1," *Comput. Phys. Commun.* **135** (2001) 238–259, `hep-ph/0010017`.

[34] C. Friberg, E. Norrbin, and T. Sjöstrand, "QCD aspects of leptoquark production at HERA," *Phys. Lett.* **B403** (1997) 329–334, `hep-ph/9704214`.

[35] **HERMES** Collaboration, K. Ackerstaff *et al.*, "The HERMES spectrometer," *Nucl. Instrum. Meth.* **A417** (1998) 230–265, `hep-ex/9806008`.

[36] **HERA-B** Collaboration, "Technical Design Report." Status Report (unpublished), DESY–PRC, 1995.

[37] A. A. Sokolov and I. M. Ternov, "On Polarization and spin effects in the theory of synchrotron radiation," *Sov. Phys. Dokl.* **8** (1964) 1203–1205.

[38] D. P. Barber *et al.*, "The First achievement of longitudinal spin polarization in a high-energy electron storage ring," *Phys. Lett.* **B343** (1995) 436–443.

[39] D. P. Barber *et al.*, "The HERA polarimeter and the first observation of electron spin polarization at HERA," *Nucl. Instrum. Meth.* **A329** (1993) 79–111.

[40] M. Beckmann *et al.*, "The longitudinal polarimeter at HERA," *Nucl. Instrum. Meth.* **A479** (2002) 334–348, `physics/0009047`.

[41] **ZEUS** Collaboration, U. Holm *et al.*, "The ZEUS Detector." Status Report (unpublished), DESY, 1993. Available on `www-zeus.desy.de/bluebook/bluebook.html`.

[42] N. Harnew *et al.*, "Vertex Triggering Using Time Difference Measurements in the ZEUS Central Tracking Detector," *Nucl. Instrum. Meth.* **A279** (1989) 290–296.

B. Foster *et al.*, "The Performance of the Zeus central tracking detector z-by-timing electronics in a transputer based data acquisition system," *Nucl. Phys. Proc. Suppl.* **32** (1993) 181–188.

B. Foster *et al.*, "The Design and Construction of the ZEUS Central Tracking Detector," *Nucl. Instrum. Meth.* **A338** (1994) 254–283.

[43] R. Hall-Wilton *et al.*, "The CTD Tracking Resolution,". ZEUS internal note 99-024.

[44] **ZEUS** Collaboration, A. Polini *et al.*, "The design and performance of the ZEUS Micro Vertex detector," *Nucl. Instrum. Meth.* **A581** (2007) 656–686, 0708.3011.

[45] M. Derrick *et al.*, "Design and construction of the ZEUS barrel calorimeter," *Nucl. Instrum. Meth.* **A309** (1991) 77–100.

A. Andresen *et al.*, "Construction and beam test of the ZEUS forward and rear calorimeter," *Nucl. Instrum. Meth.* **A309** (1991) 101–142.

A. Caldwell *et al.*, "Design and implementation of a high precision readout system for the ZEUS calorimeter," *Nucl. Instrum. Meth.* **A321** (1992) 356–364.

A. Bernstein *et al.*, "Beam tests of the ZEUS barrel calorimeter," *Nucl. Instrum. Meth.* **A336** (1993) 23–52.

[46] H. Bethe and W. Heitler, "On the Stopping of fast particles and on the creation of positive electrons," *Proc. Roy. Soc. Lond.* **A146** (1934) 83–112.

[47] J. Andruszkow *et al.*, "Luminosity measurement in the ZEUS experiment," *Acta Phys. Polon.* **B32** (2001) 2025–2058.

J. Chwastowski, J. Figiel, A. Kotarba, K. Olkiewicz, and L. Suszycki, "Aerogel Cherenkov detectors for the luminosity measurement at HERA," *Nucl. Instrum. Meth.* **A504** (2003) 222–227.

[48] M. Helbich *et al.*, "The spectrometer system for measuring ZEUS luminosity at HERA," *Nucl. Instrum. Meth.* **A565** (2006) 572–588, physics/0512153.

[49] W. H. Smith, K. Tokushuku, and L. W. Wiggers, "The ZEUS trigger system,". Contributed to 10th International Conference on Computing in High Energy Physics (CHEP 92), Annecy, France, 21-25 Sept 1992.

P. D. Allfrey *et al.*, "The design and performance of the ZEUS global tracking trigger," *Nucl. Instrum. Meth.* **A580** (2007) 1257–1282.

[50] S. Silverstein *et al.*, "The ZEUS Calorimeter First Level Trigger," *Nucl. Instrum. Meth.* **A360** (1995) 322–324.

[51] H. Uijterwaal, *The Global Second Level Trigger for ZEUS*. PhD thesis, DESY, 1992.

[52] W. O. Vogel *et al.*, "The Eventbuilder of the ZEUS Detector,". Contributed to 8th Conference on Computing in High-energy Physics: Computing for High Luminosity and High Intensity Facilities, Santa Fe, New Mexico, 9-13 Apr 1990.

[53] *ADAMO: User guide*. CERN, 1993.

[54] **ZEUS TLT Group** Collaboration, D. C. Bailey *et al.*, "The ZEUS Third Level Trigger Hardware Architecture,". Presented at International Conference on Open Bus Systems 92, Zurich, Switzerland, 13-15 Oct 1992.

[55] R. Brun *et al.*, "GEANT 3.13,". GEANT 3.13, CERN DD/EE/84-1.

[56] **ZEUS** Collaboration, J. Breitweg *et al.*, "Measurement of high Q^2 neutral current e^+p deep inelastic scattering cross-sections at HERA," *Eur. Phys. J.* **C11** (1999) 427–445, `hep-ex/9905032`.

[57] B. Straub, *The em Electron Finder*. Available on `www-zeus.desy.de/~straub/ZEUS_ONLY/doc/em.ps`.

[58] G. M. Briskin, "Diffractive dissociation in e p deep inelastic scattering,". DESY-THESIS-1998-036.

L. L. Wai, "Search for an O (100-GeV) mass right-handed electron- neutrino at the HERA electron - proton collider using the ZEUS detector,". UMI-96-06968.

[59] S. Catani, Y. L. Dokshitzer, M. H. Seymour, and B. R. Webber, "Longitudinally Invariant K(t) Clustering Algorithms for Hadron-Hadron Collisions," *Nucl. Phys.* **B406** (1993) 187–224.

S. D. Ellis and D. E. Soper, "Successive combination jet algorithm for hadron collisions," *Phys. Rev.* **D48** (1993) 3160–3166, `hep-ph/9305266`.

[60] S. Bentvelsen, J. Engelen, and P. Kooijman, "Reconstruction of (x, Q^2) and Extraction of Structure Functions in Neutral Current Scattering at HERA,". in *Physics at HERA*, vol. 1 (1991) 23; NIKHEF-H-92-02.

[61] F. Jacquet and A. Blondel *Proc. of the Study for an ep Facility for Europe* **DESY 79-048** (1979) 391.

[62] S. U. Noor, *Measurement of neutral current electron-proton cross sections with longitudinally polarised electrons using the ZEUS detector*. PhD thesis.

[63] **The D0** Collaboration, . V. Abazov, "Search for pair production of first-generation leptoquarks in p pbar collisions at sqrt(s)=1.96 TeV," 0907.1048.

[64] **CDF** Collaboration, D. E. Acosta *et al.*, "Search for first-generation scalar leptoquarks in $p\bar{p}$ collisions at $\sqrt{s} = 1.96$ TeV," *Phys. Rev.* **D72** (2005) 051107, hep-ex/0506074.

[65] C. L. Fry, *Measurement of spin-dependent charged current deep inelastic scattering cross sections using the ZEUS detector at HERA*. PhD thesis.

[66] **ZEUS** Collaboration, S. Chekanov *et al.*, "Measurement of high-Q**2 deep inelastic scattering cross sections with a longitudinally polarised positron beam at HERA," *Phys. Lett.* **B637** (2006) 210–222, hep-ex/0602026.

[67] "Measurement of high-Q^2 charged current deep inelastic scattering cross sections with a longitudinally polarised positron beam at HERA,". ZEUS-prel-07-023, submitted to EPS 07.

[68] Y.Tajima, *Development of halo muon finder for CC analysis at HERA*. Diploma thesis.

[69] X.-a. Liu, *A Search for Resonance Decays to e-jet in ep Collisions at HERA*. PhD thesis. UMI-31-10161.

[70] Y. Ri, *Measurement of e^-p Neutral-Current Deep Inelastic Scattering Cross Sections with Longitudinally Polarized Electron Beams at $\sqrt{s} = 318$ GeV*. PhD thesis. Tokyo Metropolitan University.

[71] M. Botje, "A QCD Analysis of HERA and Fixed Target Structure Function Data," *Eur. Phys. J.* **C14** (2000) 285–297, hep-ph/9912439.

[72] **ZEUS** Collaboration, S. Chekanov *et al.*, "A Search for Resonance Decays to Lepton+Jet at HERA and Limits on Leptoquarks," *Phys. Rev.* **D68** (2003) 052004.

[73] J. Sztuk, *Search for Physics Beyond the Standard Model in ep Deep Inelastic Scattering at HERA*. PhD thesis.

[74] P. Bock, "Computation of Confidence Levels for Exclusion or Discovery of a Signal with the Method of Fractional Event Counting," *JHEP* **01** (2007) 080, hep-ex/0405072.

[75] **OPAL** Collaboration, G. Abbiendi *et al.*, "Tests of the standard model and constraints on new physics from measurements of fermion pair production at 183-GeV at LEP," *Eur. Phys. J.* **C6** (1999) 1–18, hep-ex/9808023.

L3 Collaboration, M. Acciarri *et al.*, "Search for manifestations of new physics in fermion pair production at LEP," *Phys. Lett.* **B489** (2000) 81–92, hep-ex/0005028.

[76] **ALEPH** Collaboration, J. Alcaraz *et al.*, "A Combination of preliminary electroweak measurements and constraints on the standard model," hep-ex/0612034.

[77] A. Belyaev, C. Leroy, R. Mehdiyev, and A. Pukhov, "Leptoquark single and pair production at LHC with CalcHEP/CompHEP in the complete model," *JHEP* **09** (2005) 005, hep-ph/0502067.

[78] J. B. Dainton, M. Klein, P. Newman, E. Perez, and F. Willeke, "Deep inelastic electron nucleon scattering at the LHC," *JINST* **1** (2006) P10001, hep-ex/0603016.